ULTRASHORT-PULSE LASER TECHNIQUES FOR UNRAVELING CHEMICAL AND PHYSICAL PROCESSES IN NEXT-GENERATION COMBUSTION SYSTEMS

A Dissertation

by

YEJUN WANG

Submitted to the Office of Graduate and Professional Studies of
Texas A&M University
in partial fulfillment of the requirements for the degree of

DOCTOR OF PHILOSOPHY

Chair of Committee,	Waruna Kulatilaka
Committee Members,	Adonios Karpetis
	Ying Li
	Eric Petersen
Head of Department,	Andreas Polycarpou

August 2018

Major Subject: Mechanical Engineering

ABSTRACT

Ultrashort-pulse, femtosecond (fs)-duration laser techniques are powerful tools for investigating physical and chemical processes in reacting and non-reacting flow systems, providing data with high spatial and temporal resolution. Femtosecond laser pulses are advantages over traditionally used nanosecond laser pulses because of the low average power but high peak power as well as high repetition rate provided by amplified fs lasers. The objective of this thesis research is to use fs laser pulses to investigate mixing processes and also image important intermediate chemical species in combustion systems.

The primary work on mixing process studies has been demonstrated using krypton (Kr) as an inert gas tracer. A detailed spectroscopic study was performed to investigate key fluorescence channels followed by the 5p’←←4p, two-photon excitation of Kr using 204.1-nm fs pulses. The experimentally observed spectral line locations agree well with the data in the NIST Atomic Spectra Database in the 750–840-nm emission region, although significant discrepancies in some line strengths were observed. Two-dimensional (2D), two-photon laser-induced fluorescence (TPLIF) images recorded in an unsteady jet demonstrate the potential of using the fs excitation scheme of Kr for mixing and flow diagnostic studies.

In the next part of this thesis research, fs-TPLIF was investigated for detecting carbon monoxide (CO) in flames. Interferences from photolytically produced C_2 Swan-band emissions show a pronounced effect on CO fluorescence signals in fuel-rich, sooting hydrocarbon flames when using CO fs-TPLIF. Therefore, specific spectral filter is

required to reduce C_2 interferences for quantitative concentration measurements in such flames. Interferences from nascent C_2 originating from hot soot particles could be avoided by using a narrower detection gate width. At elevated pressures, CO fluorescence signal resulting from the fs excitation scheme, decays slower than that resulting from the ns excitation scheme. Comparison of the measured CO fluorescence signal with the calculated CO number density shows a good agreement for both premixed CH_4/air and C_2H_4/air flames. Subsequently, fs-TPLIF imaging measurements of CO are also demonstrated in piloted liquid-methanol spray flames.

In the final part of this research, fs pulses have been used for planar laser-induced fluorescence (PLIF) measurements of the hydroxyl (OH) radicals in flames. The excitation of the (1,0) vibrational band of the $A^2\Sigma^+ \leftarrow X^2\Pi$ electronic manifold using single-photon transition scheme has been utilized. The measured OH-LIF signals agree well with the equilibrium calculations in a range of flame conditions. Single-laser-shot, 2D OH-PLIF images recorded at 1-kHz repetition rate in a premixed C_2H_4/air jet flame and a turbulent CH_4/H_2 diffusion flame show the potential of fs-laser pulses for OH imaging measurements in reacting flow systems.

DEDICATION

To my parents for all their love and support and putting me through the best education possible. I am indebted to their sacrifices and I would not have simply been where I am today without them.

ACKNOWLEDGEMENTS

Over the past four years, I have received tremendous guidance and advice from Dr. Waruna Kulatilaka, who has been a mentor, supervisor, and a friend to me, to whom I owe my sincere gratitude. As the first doctoral student in the research group, I had a tremendous opportunity to work with him for developing and expanding our new research capabilities. He brought me into an interesting and also challenging research area. Despite my minimal background in laser-based diagnostics, he has taken his patience and expertise to explain things, sometimes over and over. Without his patience, technical guidance and encouragement, I would not have simply made such an achievement, and this doctoral dissertation would not have been possible. Meanwhile, as a friend, he has given me a lot of help and sincere suggestions for my future career. I also would like to thank Dr. Eric Petersen, Dr. Adonios Karpetis, and Dr. Ying Li for serving on my advisory committee, and providing me numerous academic and research guidance.

I would like to express my thanks to my colleagues, Morgan O'Neil, Cade Capps, Ayush Jain, and Tyler Paschal for their incredible help in experiments and making my time at Texas A&M University a truly great experience.

Finally, my utmost gratitude goes to my mother, father and older sister for their continued support and encouragement during these years.

CONTRIBUTORS AND FUNDING SOURCES

Contributors

This work was supervised by a dissertation committee consisting of Dr. Waruna Kulatilaka, Dr. Ying Li and Dr. Eric Petersen of the Department of Mechanical Engineering, and Dr. Adonios Karpetis of the Department of Aerospace Engineering.

All work for the dissertation was completed by the student, in collaboration with Ayush Jain, Tyler Pascal, and Cade Capps of the Department of Mechanical Engineering.

Funding Sources

This research was funded by grants from the National Science Foundation (NSF), Combustion, Fire and Plasma Systems Program, Office of Naval Research (ONR), and Texas A&M Engineering Experimental Station Turbomachinery Laboratory (TEES-TL).

Yejun Wang was also supported by the Ralph E. James Fellowship and the Emil Buehler Aerodynamic Analog Fellowship during this period.

The contents are solely the responsibility of the authors and do not necessarily represent the official views of NSF, ONR, or TEES-TL.

NOMENCLATURE

N_i	Population densities at state *i*
b_{12}/ b_{21}	Rate constants for absorption and stimulated emission
A_{21}	Spontaneous emission rate constant
Q_{21}	Collisional quenching rate constant
P	Predissociation rate constant
W_{2i}	Photoionization rate constant
B	Einstein coefficient for stimulated emission or absorption
I	Incident laser irradiance
c	Speed of light
h	Planck’s constant
ν	Frequency of the emitted fluorescence
Ω	Collection solid angle
A	Focal area of the laser excitation beam
l	Axial extent along the beam
I_f	Fluorescence signal
α_{13}	Two-photon absorption cross section
ξ	Mixture fraction
χ	Scalar dissipation rate
X_i	Mole fraction of species *i*
W_i	Molecular weight of species *i*

D	Local mixture-averaged mass diffusivity
k_B	Boltzmann’s constant
T	Absolute temperature
μ	Reduced mass of the CO-quencher collision pair
g	Spectral overlap
ϕ	Fluorescence yield
R	Ratio
$\Delta\varepsilon_{12}$	Energy difference between the two absorbing states
ns	nanosecond
ps	picosecond
fs	femtosecond

TABLE OF CONTENTS

Page

LIST OF FIGURES

LIST OF TABLES

Page

1. INTRODUCTION

1.1 Motivation

Combustion of fossil fuels is the foundation of global energy supply and it is expected to remain that way for the foreseeable future. However, combustion of hydrocarbon fuels releases a variety of harmful air pollutants including CO, CO_2, NO_x, SO_2 and particulates, which have great effects on the environmental pollution and human health. In addition, incomplete combustion reduces the energy conversion efficiency of various practical combustion systems. Regulations on these combustion-generated pollutants become more stringent and require drastic reduction of emissions all over the world [1]. Furthermore, a detailed understanding of combustion processes remains challenging due to the variations in temperature and pressure, and complex flow-chemistry interactions in practical combustion environments. Computer simulation of combustion processes needs to consider complex fluid mechanics, heat transfer and turbulent flow chemistry. Interactions between turbulent flow fields and complex chemical reactions for predicting flame extinction, unburnt hydrocarbon emission, and soot formation are the subject of numerous studies [2]. Meanwhile, well-designed experiments are required to validate numerical combustion models. Compared with conventional probing methods for investigation and characterization of combustion processes, laser-based diagnostic techniques offer a number of advantages. These non-intrusive methods do not disturb the flow fields and permit *in-situ* detection in some confined regions. Furthermore, they are capable of providing temporally and spatially resolved measurements via pulsed lasers, often times at high repetition rates. Therefore, laser-based techniques have been extensively developed and employed in combustion applications. Several commonly used techniques include Rayleigh scattering, Raman scattering, coherent anti-Stokes Raman scattering (CARS), tunable diode laser absorption spectroscopy (TDLAS), laser-induced fluorescence (LIF), and four-wave mixing (FWM) [3].

1.2 Imaging Diagnostics to Characterize Mixing Flow Fields

A better understanding of fuel-oxidizer mixing processes in combustion chambers is a critical step towards the development of highly efficient, low-emission engines for different applications. The fuel-oxidizer mixing primarily controls engine performance and efficiency, combustion emissions, and in extreme cases engine failure. The physical and chemical processes involved in mixing processes are very complex and present significant challenges for the modelers. Therefore, imaging diagnostics are required to visualize mixing processes and provide data for validating and improving numerical simulations. The most often used parameters to describe mixing processes in combustion systems are mixture fraction and scalar dissipation rate. For experimental determination of mixture fraction, non-reactive tracers can be seeded to one of the flow streams, which can be considered as conserved scalars and only subject to passive mixing. Through combined measurements of concentration of the tracer and temperature in turbulent combustion systems, the mixture fraction could be determined and thus the scalar dissipation rate can be calculated.

1.3 Two-Dimensional (2D) Imaging of Important Chemical Species

Incomplete combustion of hydrocarbon fuels results in harmful emission products such as carbon monoxide (CO), oxides of nitrogen (NO_x) and soot. The computational models of formation mechanisms of these products are based on elementary chemical reactions and reaction rates in combustion systems, which involve a large number of intermediate species and reactions. In these elementary reactions, reactive atoms such as hydrogen (H), oxygen (O), carbon (C), nitrogen (N), as well as molecular species such as CO and hydroxyl (OH), and nitric oxide (NO) play an important role in heat release and pollutant formation pathways. For example, atomic hydrogen is highly diffusive and hence play a critical role in flame ignition, propagation and extinction. Atomic oxygen involves in chain-branching reactions and pollutant formation pathways of hydrocarbon fuels [4, 5]. Atomic nitrogen is a key species in the formation of NO_x through Zeldovich mechanism, prompt mechanism, N_2O (nitrous oxide)-intermediate mechanism or NNH at different combustion conditions [6]. CO is a highly toxic combustion product, and its level increases during incomplete combustion. Meanwhile, it also affects the heat release in combustion through C-H-O reaction mechanism $CO + OH \rightarrow CO_2 + H,$ and hence many research studies have been conducted on measurements of its reaction rate [7, 8]. To improve the models and better understand the combustion processes, it is of great importance to develop techniques which can facilitate two-dimensional (2D) imaging of reactive species with sufficient temporal and spatial resolutions in combustion environments.

1.4 Potential of Ultrashort-Pulse-Based Imaging Techniques

Among all possible laser-based diagnostic approaches, LIF is the most promising technique for investigating minor atomic and radical species in combustion environments, because of its high sensitivity and ease of extension to 2D imaging [2]. Previously, most investigations on minor species measurements have used nanosecond (ns) laser systems [9-11]. It is found that the application of the LIF technique has been obstructed in some situations by the unintended generation of the same species being detected by photodissociation of certain flame radicals when using ns laser systems. Examples are atomic hydrogen produced by hydroxyl, water vapor and methyl photodissociation [12], and atomic oxygen and CO produced by CO_2 photodissociation [13]. Recently, as a result of successful demonstrations of the use of ultrashort, femtosecond-duration (fs) laser pulses, photolytic-interference-free, efficient two-photon excitation of H [14, 15] and O [16] atoms have been revealed. The potential of similar two-photon LIF (TPLIF) schemes for applications involving CO and Kr imaging measurements have also been explored. The natural fluorescence lifetime of the CO $B^1\Sigma^+$ state is approximately 22 ns; however, quenching effects at modest pressures significantly reduce the effective lifetime to a few nanoseconds (ns) [14]. Previous CO measurements have been carried out mainly using ns-duration pulsed lasers, and therefore could not satisfy the temporally-resolved quantitative CO measurement requirements in practical combustion environments [14-16]. In recent studies, Brackmann et al. [17] applied picosecond (ps)-duration excitation pulses to determine CO in premixed laminar flames and then compared the results with ns excitation scheme. They concluded that ps-duration excitation pulses showed more efficient signal strength in the CO-TPLIF technique as well as reduction of C_2 interferences using a narrower detection gate. More recently, fs laser pulses have been used for CO measurements in flames and negligible photolytic interferences were observed [18].

1.5 Dissertation Outline

Previous investigations have shown that the broadband, fs laser pulses can provide interference-free measurements of important intermediate species in combustion and plasma systems. Hence the fs-duration laser pulses are increasing been used for investigating mixing processes and important chemical species measurements such as CO and OH in non-reacting and reacting flow fields. Meanwhile the high peak intensity of fs laser pulses associated with broadband widths enables efficient nonlinear excitation. Furthermore, the high repetition rates of the fs pulses can also enable to better understand the dynamics of turbulent flow systems. Hence, the fs laser pulses combining with the LIF technique are used for investigating important minor species and mixing processes in various flow fields. A comprehensive literature review of related LIF theory, developments, applications and challenges are present in Section 2. Section 3 describes the Kr fs-TPLIF experimental apparatus and presents important findings. The CO fs-TPLIF experimental apparatus and burner facilities, and the results of spectroscopic studies, applications in gaseous sooting flames as well as liquid-fuel spray flames are present in detail in Section 4. OH fs-PLIF imaging measurements are also demonstrated in Section 5. Section 6 contains a summary and a conclusion of the current work, and an outline of future research direction.

2. LITERATURE REVIEW

2.1 LIF Theory

LIF technique is based on the resonant absorption of laser photons followed by the detection of spontaneous fluorescence emission. Compared with other laser-based techniques, LIF shows high detection sensitivity of specific chemical species, and could be easily extended to 2D imaging measurements via planar laser-induced fluorescence (PLIF) [13]. The simple two-level energy diagram of the LIF technique is illustrated in Figure 1.

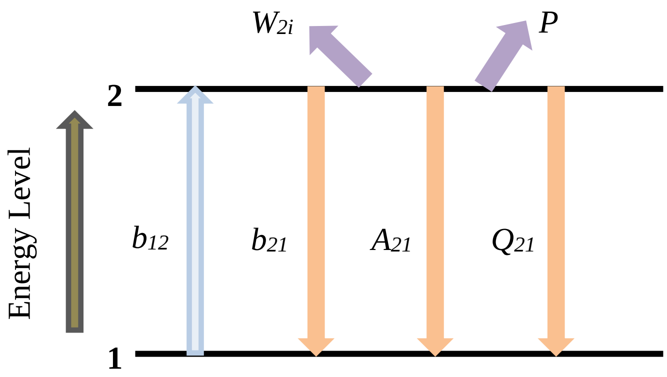

Figure 1. A simple two-level energy diagram for LIF reprinted from [3].

The population density of the states 1 and 2 can be expressed as [3];

$$\frac{dN_1}{dt} = -N_1 b_{12} + N_2 (b_{21} + A_{21} + Q_{21}) \qquad \textbf{(1)}$$

$$\frac{dN_2}{dt} = N_1 b_{12} - N_2 (b_{21} + A_{21} + Q_{21} + P + W_{2i}) \qquad \textbf{(2)}$$

where N_1 and N_2 represent the population densities at state 1 and 2 respectively, b_{12} and b_{21} are the rate constants for absorption and stimulated emission respectively. A_{21} is the spontaneous emission rate constant given by the Einstein coefficient, Q_{21} is the collisional quenching rate constant, P is the predissociation rate constant; and W_{2i} is the photoionization rate constant.

The rate coefficient for b_{12} and b_{21} can be expressed by

$$b = \frac{BI}{c} \tag{3}$$

where B is the Einstein coefficient for stimulated emission or absorption, I is the incident laser irradiance, and c is the speed of light.

If the predissociation and photoionization processes are assumed to be negligible, then

$$\frac{dN_1}{dt} + \frac{dN_2}{dt} = 0 \tag{4}$$

and thus,

$$N_1 + N_2 = constant = N_1^0 \tag{5}$$

where the N_1^0 indicates the population density at state 1 prior to laser excitation.

At a steady state,

$$\frac{dN_1}{dt} = \frac{dN_2}{dt} = 0 \tag{6}$$

By combining Equations (1)–(6), we can obtain

$$N_2(t) = \frac{b_{12}N_1^0}{r}(1 - e^{-rt}) \tag{7}$$

where $r=b_{12}+b_{21}+Q_{21}+A_{21}$.

Then the fluorescence signal I_f can be expressed as

$$I_f = h\nu \frac{\Omega}{4\pi} lAN_1^0 \frac{B_{12}}{B_{12} + B_{21}} \frac{A_{21}}{1 + \frac{I_{sat}}{I}} \tag{8}$$

where h is the Planck's constant, ν is the frequency of the emitted fluorescence, Ω is the collection solid angle, A is the focal area of the laser excitation beam, l is the axial extent along the beam from which the fluorescence is observed, I_{sat} is the saturation laser irradiance.

At lower laser irradiances wher $I \ll I_{sat}$, equation (8) can be simplified as

$$I_f = \frac{h\nu}{c}\frac{\Omega}{4\pi}lAN_1^0B_{12}I\frac{A_{21}}{A_{21}+Q_{21}} \qquad \mathbf{(9)}$$

It is expected that the LIF signal is proportional to the laser irradiance at lower laser irradiance values. One of the most important effects for quantitative species measurements is the quenching effect (Q_{21}) in the linear regime, because it significantly depends on collisional molecules and their concentrations, and also variations of temperature and pressure.

When the laser irradiance $I \gg I_{sat}$, equation (8) can be rearranged to

$$I_f = h\nu\frac{\Omega}{4\pi}lAN_1^0\frac{B_{12}}{B_{21}+B_{12}}A_{21} \qquad \mathbf{(10)}$$

In the saturation regime, the LIF signal is independent on both the laser irradiance and collisional quenching rate, hence the saturation LIF is one way to avoid corrections for quenching effects in LIF applications. However, it is a somewhat difficult to achieve complete saturation because of the specific wavelength region or the saturation energy level [3].

In practical LIF applications, there is no exact two energy level system and the fluorescence emission wavelength would be red-shift to avoid the interference from excitation laser itself. Moreover, the lower electronic transitions accessible from the ground states in most atoms and in some radicals of combustion interest such as H and O require high laser energies, which correspond to vacuum-ultraviolet (VUV) excitation wavelengths if the single-photon LIF technique is used. In these wavelengths, the medium becomes optically thick to the VUV radiation. Therefore, multi-photon excitation schemes must be employed in practical diagnostic applications to red shift the excitation wavelengths to the ultraviolet (UV) region [2]. Therefore, two-photon laser-induced fluorescence (TPLIF) has been widely used for detecting atoms and radicals in reacting flow systems [8, 19-21].

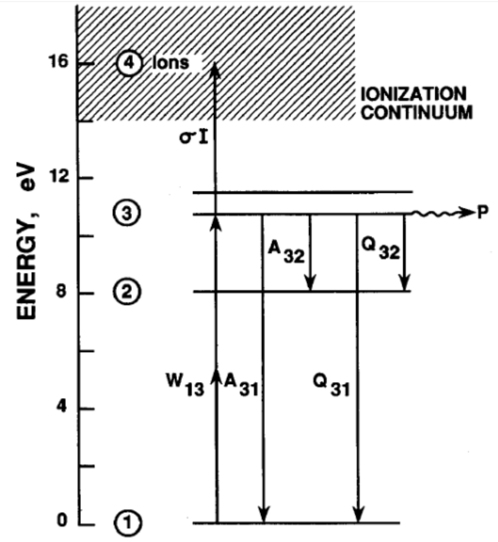

Figure 2. A schematic energy level diagram for TPLIF reprinted from [22].

As shown in Figure 2, the rate of change of the population at the excited state for a two-photon excitation can be expressed by [22],

$$\frac{dN_3}{dt} = N_1 W_{13} - N_3(Q + A + P) - N_3 \sigma I \tag{11}$$

where N_1 and N_3 represent the population densities at ground state and excited state respectively. W_{13} represents the two-photon absorption rate coefficient, σ represents the rate coefficient, I represents the laser fluence. Q is the collisional quenching which depends on collisional partners, temperature and pressure. A and P represent the rates of spontaneous emission from the excited state and predissociation, respectively.

The rate coefficient for two-photon absorption W_{13} can be written as [23]

$$W_{13} = \frac{\alpha_{13} I^2}{\hbar\omega} \quad \textbf{(12)}$$

where α_{13} is the two-photon absorption cross section from ground state 1 to excited state 3. It is a function of temperature, laser excitation frequency, two-photon absorption line shape, and laser linewidth. I is the laser fluence, ω is the laser frequency, and $\hbar$ is the Planck constant.

At equilibrium conditions, $dN_3/dt = 0$, hence,

$$N_3 = \frac{N_1 W_{13}}{(Q + A + P + \sigma I)} \quad \textbf{(13)}$$

Thus, the observed fluorescence signal can be expressed by,

$$I_f \propto \frac{N_1 \alpha_{13} I^2}{(Q + A + P + \sigma I)\hbar\omega} \quad \textbf{(14)}$$

At low laser intensities, the fluorescence signal of two-photon excitation is proportional to the square of the laser fluence. Other competing processes, such as photochemical production, collisional quenching, and photoionization reactions can result in interpreting the LIF signal more complicated.

2.2 TPLIF Imaging of Inert Gas Tracers for Mixing Studies

Understanding of fuel-oxidizer mixing processes is crucial to better characterize complicated flow-flame interactions taking place in turbulent non-premixed and partially premixed flames, such as those present in gas turbines and internal combustion engines. Two critical parameters are used in general to characterize mixing processes between the fuel and the oxidizer streams. They are mixture fraction (ξ) and scalar dissipation rate (χ), as defined by,

$$\xi = X_{fuel} \times \frac{W_{fuel}}{W_{mix(\xi)}} \tag{15}$$

$$\chi = 2D(\nabla\xi \cdot \nabla\xi) \tag{16}$$

where X_{fuel} is the mole fraction of gases originating from the fuel stream, W_{fuel} is the molecular weight of the fuel stream, $W_{mix(\xi)}$ is the local mixture molecular weight, and D is the local mixture-averaged mass diffusivity.

From above equations, the scalar dissipation rate can be determined via measuring the gradient of mixture fraction. Because of the temporal and spatial variations of temperature, pressure and chemical species in turbulent flows and non-premixed flames, multi-dimensional measurements of mixture fraction in reactive and non-reactive flow systems are required to determine the scalar dissipation rate. Non-intrusive laser-based techniques have been long developed in combustion and plasma systems because of their capabilities for chemical species measurements with high spatial and temporal resolutions. Previously, various approaches have been employed to investigate mixture fraction and scalar dissipation rate. For example, Barlow and Karpetis [24] used Raman scattering, Rayleigh scattering and CO LIF to investigate one-dimensional measurements of temperature, mixture fraction and scalar dissipation rate in partially premixed flames. Frank et al. [8] employed a three-scalar technique to measure mixture fraction via using polarized Rayleigh scattering, fuel concentration and CO LIF. An alternative way for determining mixture fraction is to seed a non-reactive tracer into one of the flow streams.

The tracer could be considered as a conserved scalar and only subject to passive mixing. The mixture fraction is then calculated by measuring the tracer concentration and temperature simultaneously. Several tracers have been developed in recent decades. Sutton and Driscoll [25] seeded NO gas into a CO-air flame. Because the seeded NO does not react in this flame configuration, they considered the mass fraction of NO as a conserved scalar. By combining NO-PLIF and planar Rayleigh scattering temperature measurements simultaneously, they quantitatively determined NO mixture fraction in a turbulent jet flame. However, NO was only used for dry CO-air flames where the chemistry is well-controlled. When it applies for hydrocarbon fuels, NO would involve in reacting with intermediate species, thus NO could not be considered as a conserved scalar. Furthermore, NO is widely used as a tracer species for different applications [26-30]. Fletcher and McDaniel used iodine as a tracer to investigate compressible flow fields in a steady, non-reacting supersonic combustor [31]. Cheng et al. [32] seeded sodium into a supersonic nitrogen jet to visualize the flow fields. Some hydrocarbon materials such as toluene [33] and acetone [34] have also been used as tracers for thermometry in different flow fields. However these tracers have some restrictions due to their toxicity, reactivity and condensation issues [35].

More recently, Krypton gas has been used for mixture fraction imaging. The two-photon excitation transition of Kr is accessible easily compared to other inert gases [36]. Furthermore, injection of Kr in dilute concentrations has negligible effects on thermo-physical and thermo-chemical properties of reacting flows [36]. Hence, as a tracer species, Kr has a great potential in numerous engineering applications [37-40]. Hsu et al.[41] first demonstrated Kr-TPLIF to determine mixture fraction imaging in turbulent jet flames. The results showed that measurements of mixture fraction with the Kr-TPLIF were in a good agreement with previous data of the Sandia flame D and DLR-B flames. They also pointed out that interference processes such as stimulated emission and signal absorption (ie., fluorescence trapping) can affect measurements at higher seed concentrations. Narayanaswamy et al.[35] further employed Kr-PLIF for scalar imaging in supersonic flows and the results showed Kr was a suitable marker in supersonic and hypersonic flows. For above applications of Kr-TPLIF, two-photon excitation transition at 214.7 nm has been used. In this scheme, atomic krypton is excited from $4p^6(^1S_0)$ ground state to $5p[3/2]_2$ excited state, followed by detection of fluorescence emission at 760 nm from $5p[3/2]_2$ to $5s[3/2]_2$ radiative decay. The detection channel yielded higher fluorescence signal levels [40] and the radiative lifetime of the $5p[3/2]_2$ excited state was found to be 25.4±0.8 ns [42]. Moreover, the 204.1-nm excitation scheme of krypton has been used for calibration measurements of absolute H-atom and N-atom number densities in a similar TPLIF scheme. The $5p'[3/2]_2 \leftarrow\leftarrow 4p^6[^1S_0]$ excitation scheme is preferred because of its wavelength proximity to corresponding H-atom excitation transition [43, 44]. However, the latter excitation scheme has not been used for mixing studies in turbulent combustion environments.

2.3 Quantitative CO Measurement in Flames

One of the major byproducts of the incomplete combustion of hydrocarbon fuels is carbon monoxide (CO), especially in fuel-rich or sooting flames. Because of its contribution on environmental pollution and as an indicator of combustion efficiency [45], a more detailed understanding of CO formation and distribution is of great interest in various combustion conditions. Therefore numerous laser-based techniques have been employed to measure CO concentrations in flames in past decades, such as Raman spectroscopy [46, 47], gas chromatography [48, 49], mass spectroscopy [50], diode laser wavelength modulation spectroscopy [51], direct tunable diode laser absorption spectrometer (TDLAS) [52-54], 2+1 resonance-enhanced multiphoton ionization [55, 56], amplified stimulated emission [57], and LIF [58-60].

For CO-TPLIF measurements in combustion environments, as shown in Figure 3, several excitation schemes are possible: 1) $C^1\Sigma^+ \leftarrow X^1\Sigma^+$ transition at 217-nm radiation following detection at the $C^1\Sigma^+ \rightarrow A^1\prod$ Herzberg band (360–600 nm); 2) $B^1\Sigma^+ \leftarrow X^1\Sigma^+$ transition at 230.1-nm radiation following detection at the $B^1\Sigma^+ \rightarrow A^1\prod$ Ångström band (400–600 nm); and 3) detection at $b^3\Sigma^+ \rightarrow a^3\prod$ (282–380 nm) the third positive band with the same excitation radiation at 230.1 nm followed by vibrational redistribution [61, 62]. Rosell et al. [61] extensively investigated these three two-photon excitation schemes. They found that the Ångström band was less sensitive to pressure but it suffered from the crosstalk with strong C_2 Swan band interferences. The third positive band was better isolated compared to the Ångström band in terms of C_2 interferences, however, it showed stronger pressure and quenching dependencies, as well as broadband emission interferences from polycyclic aromatic hydrocarbon (PAH) compared with the other two bands. Hence, quantitative CO measurements are difficult by analyzing fluorescence signals from the third positive band. The Herzberg band is more sensitive to pressure than the Ångström band, but less sensitive than the third positive band, and it also suffers from C_2 Swan band and C_2 Deslandres d'Azambuja band emissions. Lindow et al. [62] stated that the Herzberg band is advantageous over the Ångström band in terms of crosstalk of C_2 interferences. Most previously published studies on CO-TPLIF measurements have used the 230.1-nm excitation scheme and analyzed fluorescence signals from the Ångström band [17, 18, 63-67]. To quantitative measurements of CO concentrations in different combustion conditions, numerous investigations have been performed to determine important parameters under various conditions that the CO radicals would undergo in the two-photon LIF process.

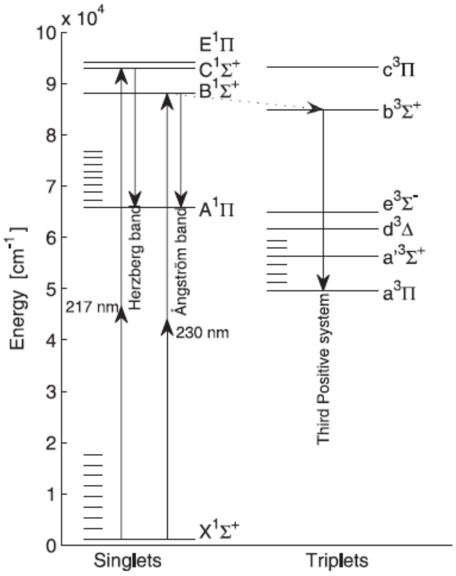

Figure 3. Various excitation/detection energy levels for CO-TPLIF reprinted from [61].

One of the major interferences in a two-photon LIF scheme is photochemical effects. Signal interferences by photodissociation effects have been investigated extensively in research for which the two-photon LIF technique has been used to measure different atoms in flame and plasma systems [12, 68-70]. The photolytically-generated CO interferes with nascent CO in combustion environments and thus deviates from the theoretically expected quadratic dependence. By defocusing the exciting beam in a probe region, photolysis of CO_2 with the 230.1-nm beam can reduce. However, CO quenching processes would increase and thus make absolute CO concentration measurements substantially difficult [71, 72]. Zobnin et al. [71] investigated photodissociation of heated CO_2 and pointed out that the dissociation of CO_2 molecules absorbing radiation at 230 nm could undergo through two pathways:

$$CO_2 \rightarrow CO\ (X^1\Sigma) + O\left(\,^1D\right)\ energy = \ 7.4\ eV \qquad \textbf{(17)}$$

$$CO_2 \rightarrow CO\ (X^1\Sigma) + O\left(\,^3P\right)\ energy = \ 5.45\ eV \qquad \textbf{(18)}$$

Bernstein et al. [73] observed that the results agreed well with the calculations at lower laser energies, and largely deviated from the calculations at higher pulse energies. One possible explanation for this observation was the photodissociation of CO_2 via the process given in Eqn. (6) was followed a two-photon excitation of the CO_2^* state of g-symmetry. Nefedov et al. [72] also stated CO formation as a result of CO_2 photodissociation with the 230.1-nm excitation scheme by comparing CO with OH concentrations. They pointed out that it was necessary to consider CO_2 photodissociation when the CO concentration was low in high-temperature gas mixtures containing CO_2 when using the two-photon LIF method. They further indicated that 2-3% of CO_2 molecules could be dissociated at 2000 K. Moreover, a correction for the contribution of CO produced by the CO_2 photolysis was deduced under certain conditions [72]. Furthermore, the resonant photodissociation of CO itself could underestimate CO concentration measurements in non-sooting flames [59].

Chien et al. [63] pointed out photodissociation of CO_2 depended on temperature in flames, which had a minor contribution when the temperature was below 1400 K, but became important at higher temperature regions.

At higher laser energies, the photoionization process (σI) competes with other processes and thus yields the intensity dependence I^n of $n<2$ ($\sigma I >> (Q+A+P)$). LIF signal is then independent of the quenching rate of the CO state, and scales linearly with laser energy. This linear dependence could be used as a calibration for absolute CO concentration. Everest et al. [74] measured the laser energy dependence of the CO fluorescence signal in flickering methane/air diffusion flames. They observed a linear dependence at higher energies and suggested that the fluorescence signal was independent of laser energy because of photoionization depletion in the focal region at the highest energies. Tjossem et al. [22] reported an $I^{1.5}$ dependence of fluorescence signal at lower laser energies and an $I^{1.0}$ dependence at the highest intensities, they also observed an $I^{2.5}$ dependence of ionization signal at low laser energies. Brackmann et al. [17] investigated a laser energy dependence $I^{1.4}$ of the LIF signal in ethane-air flames with equivalence ratio $\Phi=1.0$, and an $I^{1.0}$ dependence at $\Phi=2.1$ in the range of 0.3-3 GW/cm^2. They stated that the photoionization process dominated over the collisional quenching above 0.2 GW/cm^2 and thus reduced the expected quadratic laser energy dependence for the two-photon excitation scheme.

Another important consideration in quantitative CO-TPLIF measurements is the influence of collisional quenching on fluorescence signal. According to the equation of the observed fluorescence signal shown by Equation (14) above, it increases with the inverse of the quenching rate. Changes such as temperature, pressure and chemical composition in combustion environments can affect the measured fluorescence and thus result in a misinterpretation of CO distributions. One way to eliminate the collisional quenching is to use saturated LIF, in which the fluorescence signal is independent of both the laser energy and collisional quenching [3]. Quenching corrections can be calculated from the temperature and composition of the flame to result in temperature- and species-dependent quenching cross sections. The total quenching rate Q could be calculated as [75]:

$$Q = N_{tot} \sum_i X_i \sigma_i < \nu_i >= N_{tot} \sum_i X_i \, k_i \qquad \textbf{(19)}$$

where N_{tot} represents the total number density, X_i represents the mole fraction of species i, σ_i is the thermally averaged cross-section for quenching by species i, $<\nu_i>$ is the mean relative collision velocity of molecule CO and collider species i, k_i is the quenching rate coefficient which is equal to the product of σ_i and $<\nu_i>$. The mean relative collision velocity $<\nu_i>$ is given by,

$$< \nu_i >= \sqrt{8k_B T / \pi\mu} \qquad \textbf{(20)}$$

where k_B is Boltzmann's constant, T is the absolute temperature and μ is the reduced mass of the CO-quencher collision pair.

A comprehensive data of temperature- and species-dependent cross-sections for quenching of CO molecules is not available for conditions relevant to flames. A direct method to obtain quenching cross-sections is to measure the time-resolved fluorescence signal with a short-pulse laser excitation and observe the relationship between the fluorescence lifetime and the quencher pressure. Agrup and Alden [76, 77] measured the lifetime of CO ($B^1\Sigma^+$) in hydrocarbon flames and observed that the effective lifetime was 250 ps in the reaction zone and increased to 400 ps near the outer reaction zone in methane/oxygen flames. The effective lifetime was 400 ps near the inner reaction zone and increased to 600 ps near the outer reaction zone in ethylene/air flames. However, information about species-specific quenching cross-sections was unknown, although the CO self-quenching rate coefficient was reported. Di Teodoro et al. [14] first investigated pressure-dependent quenching cross sections of CO $B^1\Sigma^+$ (v'=0) state in collisions with Ne, He, N_2, H_2, CO, Ar, CH_4, Kr, Xe, O_2, C_3H_8, CO_2 and H_2O at room temperature. They observed the fluorescence decay rates of CO with those quenchers increased with pressure increased. The fluorescence lifetime of the CO self-quenching initially increased with pressure, and then decreased at higher pressures because the self-quenching overcame the trapping effect. Settersten et al. [78] used short laser pulses (~100 ps pulse duration) to investigate the quenching cross sections of CO $B^1\Sigma^+$ (v=0) state with He, Ne, Ar, Kr, Xe, H_2, N_2, O_2, CO, H_2O, CO_2, and CH_4 as collisional partners at different temperatures. They observed the self-quenching cross section of CO was independent on temperature, the cross sections of the weakest quenchers (He, Ne, H_2, N_2) increased with temperature, while decreased with temperature for strongest quenchers (H_2O, CO_2, Xe, O_2, CH_4, Kr, Ar). The cross section for H_2 had a $T^{0.43}$ dependence which is the largest positive temperature dependence, while H_2O had a $T^{-0.44}$ dependence which is the largest negative dependence. Di Rosa and Farrow [79] used an absorption technique to determine the two-photon absorption in the B←X (0,0) band of CO by analyzing absorption spectra with well-characterized spatial profiles of Fourier-transform-limited laser pulses. Moreover, they further investigated the cross sections of photoionization and ac stark shift, and stated that the cross sections of photoionization and stark shift varied with rotational level [80]. Rosa and Farrow [81] investigated collisional broadening and shift in the B←X (0,0) band of CO in colliding with N_2, CO_2 and CO at various temperatures, then verified the results with measurements in an atmospheric-pressure $CH_4/O_2/N_2$ flame at 1950 K.

Another important interference when using the 230.1-nm excitation scheme is the crosstalk of strong C_2 Swan-bands ($d^3\prod_g$–$a^3\prod_u$) in the 430–700 nm range in hydrocarbon flames [82]. C_2 could be generated by sequential elimination of H atoms of acetylene, ethane and vinyl radicals at efficient laser intensities [59, 83, 84]. For example, C_2 is produced by acetylene in a two-photon process as follows [83]:

$$C_2H_2 \rightarrow C_2H + H \quad \textbf{(21)}$$

$$C_2H \rightarrow C_2 + H \quad \textbf{(22)}$$

Soot could also produce C_2 via laser-induced vaporization or non-thermal desorption [17, 85]. Alden et al. [60] observed C_2 spectra in flames when the detection gate was delayed, its emissions extended longer than CO fluorescence emissions. Tuning the laser wavelength off the CO resonance resulted in disappearing of CO fluorescence and reduction of C_2 emission intensity significantly. With a narrowband detection filter which centers on isolated CO spectral lines, C_2 interference could be reduced, but this also reduces CO signal levels as well [17].

As summarized above, most investigations have been conducted in gaseous hydrocarbon fuels. Direct-injection liquid spray flames are also used in many combustion engines for ground transportation, power generation, aviation, and propulsion applications. The growing demand for advanced liquid-fuel combustors with improved combustion efficiency and reduced pollutant emissions has resulted in growing interest in the fundamental research in liquid-spray combustion. In these combustors, the fuel supplied in the liquid phase is first atomized in a spray nozzle, then evaporates and mixes with a gaseous oxidizer to form a combustible mixture. However, length and time scales associated with these different processes as well as chemical kinetics and turbulent flow-flame interactions considerably complicate the overall combustion process [86-88]. Therefore, sophisticated experimental and numerical approaches are required to better understand the spray combustion process in such challenging environments.

In general, liquid sprays are categorized into dilute and dense regions depending on the relative number of liquid droplets per unit volume of gas, represented by the group number, G. For example, a reaction zone surrounded by a cloud of droplets is represented by a G much larger than one, whereas a reaction zone dominated by droplets burning individually corresponds to G less than one [89]. However, dilution effects are present in the far field from the spray exit of group combustion. Karpetis and Gomez [90] measured droplet number densities in turbulent non-premixed flames and stated that large droplet densities were achieved at the centerline close to the exit while the densities reduced significantly along the axial position due to the dispersion and evaporation of the jet spray. Previous studies of spray combustion mainly focused on the characterization of various sprays using laser-based techniques [91-93]. Well-developed, phase Doppler anemometry (PDA) has been used to measure physical characteristics of sprays, such as velocity statistics, droplet size and concentration [94-96]. The measured droplet size is normally in the order of micrometer (µm) scale and the droplet diameter has an important role in spray combustion [97, 98]. Rodrigues et al. [99] employed CARS to measure temperature distributions in conventional and hot-diluted combustion regimes. Ge et al. [100] measured liquid-phase temperature via two-color LIF of Rhodamine B and gas-phase temperature via multi-line NO-LIF. Moreover, hydroxyl radical (OH) LIF has been widely used for characterizing the reaction zones of spray flames. Stepowski et al. [92, 101] performed OH-PLIF imaging in a near field of a combusting spray jet and the results showed that the two-phase flame was developed of two diverging diffusion-like flame fronts, also predicted by the simulation of spray combustion in a counter-flow laminar diffusion flames. Furthermore, the combination laser-induced incandescence (LII), LIF and droplet Mie scattering has been used to measure soot volume fraction, OH distribution, and spray pattern for investigating the mechanism of soot formation in a swirl-stabilized spray combustor [102, 103]. However, little work has been reported on CO-TPLIF measurements in liquid-spray flames.

2.4 OH Thermometry in Flames

As a key species in the chain-branching reactions for hydrogen and hydrocarbon combustions, hydroxyl radical (OH) has been proven to be a good flame marker of the reaction zones in flames [104]. Therefore, considerable efforts have been investigated on OH-PLIF in various reacting flow systems because of its simple experimental configuration. In addition, the signal-to-noise ratio of OH-LIF is relatively high because of the abundant presence of OH radical in most high-temperature combustion processes, even in 2D imaging measurements [105]. Several excitation schemes such as (0, 0) [7], (1, 0)

[8], (2, 0), and (3, 0) [106] bands of the OH $A^2\Sigma^+ \leftarrow X^2\Pi$ system, have been performed in single-photon [8, 107] and two-photon OH-LIF [108-110] transitions. Furthermore, the combination of OH/CO [8] and OH/CH_2O [111] measurements is used for reaction-rate imaging in various flames.

Temperature is another key parameter in understanding chemical interactions in complex combustion environments. Several laser-based diagnostic techniques, such as Raman scattering, CARS, LIF, absorption spectroscopy and Rayleigh scattering, have been used for temperature measurements [3]. The Raman scattering signal could be significantly affected in fuel-rich flames and liquid-fuel flames [112]. CARS is a point measurement approach and thus time consuming for obtaining temperature distributions in large volumes. Furthermore, crossing of multiple laser beams is present in an complicated experimental setup. However, CARS is well suited for single-shot temperature measurements because of its high accuracy and robustness [113]. Rayleigh scattering shows a temperature accuracy of <1%, but it is difficult to determine the dependence of scattering cross section on temperature for each molecule and its concentration [114]. LIF can be used for single-shot thermometry by exciting two different transitions of an atomic or molecular species simultaneously, then calculating the ratio of the fluorescence signal from the two transitions (two-line OH thermometry) which relates to temperature based on Boltzmann statistics [115]. In addition, OH radicals have sufficient concentrations and naturally exist in flames at high temperatures ($T>1200$ K). Therefore, the two-line, OH-PLIF has been used for thermometry measurements in combustion configurations [112, 116-118].

At lower laser pulse energies, the total fluorescence signal of OH-PLIF can be expressed by [119],

$$I_f = \eta V_C n_a f(T) BE g(\nu_L, \nu_a) \frac{A}{A+Q} \quad \textbf{(23)}$$

where η is the overall efficiency of optics and the detection system; V_C is the collection volume imaged onto the detection system; n_a is the number density of OH radicals; $f(T)$ is the fractional (Boltzmann) population of the lower state without the laser field; $g(\nu_L, \nu_a)$ is the spectral overlap between the laser profile (g_L) and the Doppler-, collision-, and lifetime-broadened adsorption profile (g_a) of the OH radical. The fluorescence yield ϕ is defined by $A/(A+Q)$.

Thus, the ratio (R) of fluorescence signals from the two different excitation lines at the same probe region is given by,

$$R = \frac{I_{f1}}{I_{f2}} = \frac{(\eta BE)_1}{(\eta BE)_2} \frac{g_1}{g_2} \frac{f_1}{f_2} \frac{\phi_1}{\phi_2} \quad \textbf{(24)}$$

Furthermore, it assumes that the temperature dependence on the fluorescence ratio only originates from the relative populations in the absorbing states, then

$$R = C \frac{E_1}{E_2} exp(-\Delta\varepsilon_{12}/kT) \quad \textbf{(25)}$$

where C is a parameter that can be calculated or treated as a calibration constant; $\Delta\varepsilon_{12}$ is the energy difference between the two absorbing states.

And the slope sensitivity of the two-line OH-PLIF is,

$$\left|\frac{dR}{R}\right| = \frac{\Delta\varepsilon_{12}}{kT} \left|\frac{dT}{T}\right| \quad \textbf{(26)}$$

To obtain high accuracies of the two-line OH-PLIF thermometry in flames, the transitions have to be carefully selected for providing good SNR and reducing systematic errors. Seitzman et al. [119] suggested that the rotational level N should be between 5 and

12, and the two transition lines must be isolated from neighboring OH lines. While Cattolica [115] chose adjacent rotational levels, and stated that the rotational level ($N \geq 8$) can make the fluorescence intensity sensitive to the rotational temperature in the range of 1000–3000 K. Other studies have also been investigated on optimizing transition pairs in different types of reacting flows and simulated engine environments [120-122]. It is shown that the pair of OH $A^2\Sigma^+ \rightarrow X^2\prod$ (1,0) $Q_1(5)$ and $Q_1(14)$ transition lines is found to yield the most accurate OH-PLIF thermometry measurements among other transition pairs [116, 123]. Moreover, system errors such as spectral broadening, fluorescence trapping effect and pulse-to-pulse laser fluctuation, have been analyzed in the two-line OH-PLIF thermometry methods [119].

2.5 Fundamentals of Ultrashort Pulse Laser Diagnostics

As discussed above, most laser-based measurements have been performed using conventional continuous-wave and ns-pulsed laser systems. For quantitative species measurements with the LIF technique, interferences such as collisional quenching effects must be corrected in these measurements. The fluorescence lifetime of excited species of interest reduces to a few nanoseconds or even hundreds of picoseconds in atmospheric-pressure hydrocarbon flames [7]. Therefore, the measured species can collide with other species several times during the time of excitation and detection process based on the use of ns laser pulses (~10 ns pulse-duration). Excitation schemes by the traditional lasers are insufficient for time-resolved quenching rate studies. One approach to eliminate collisional effects on species concentrations in the conventional LIF signals is the use of ultrashort laser pulses (i.e., ps and fs). For example, ps laser pulses coupled with fast-gated detection cameras are employed to determine rate constants for fluorescence lifetime, collisional quenching and vibrational energy transfer [124, 125]. Photodissociation is another important interference in the LIF process. High-energy laser pluses are required to generate sufficient signals when ns-duration laser pulses are used for species measurements. Thus, the collected fluorescence signals are susceptible to laser-induced interferences as shown in Figure 4 (a). In contrast, the nearly Fourier-transform-limited, ultrashort fs pulses demonstrate photolytic-interference-free measurements of atoms in flames as shown in Figure 4 (b). Furthermore, the low-average power but high-peak-power fs pulses can enhance two-photon excitation efficiency and mitigate interferences from single-photon-absorption photodissociation processes. Therefore, the fs-TPLIF scheme has been demonstrated of having the potential of interference-free 2D imaging measurements of chemical atomic species [126-128]. The ultrashort laser pulses have been also used for investigating CO detection in combustion systems. Brackmann et al. [17] applied ps pulses to determine CO in premixed laminar flames, stated that ps pulses show stronger signal strengths, as well as reduction of C_2 interference, when a narrower detection gate width is employed. Recently, the fs laser pulses have also been performed in TPLIF of CO measurements in flames [18, 129]. Moreover, low repetition rates of the ns lasers could not reveal turbulent dynamics in complex reacting flows, although several higher repetition rate systems have recently been demonstrated [130]. The high repetition rate (i.e. 1 kHz) of the fs laser pulses also become advantageous in capturing the dynamics of turbulent flows [131].

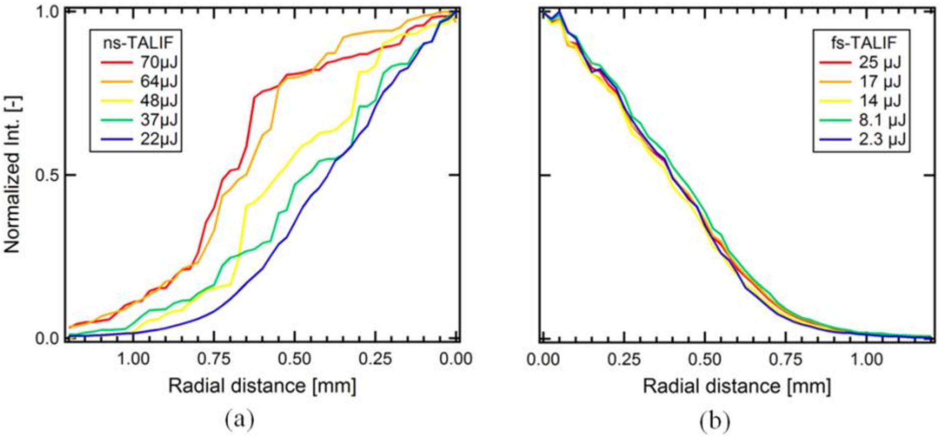

(a) (b)

Figure 4. Peak-normalized TPLIF line profiles of atomic oxygen at various laser-pulse energies recorded in flames using (a) ns pulses and (b) fs pulses reprinted from [132].

3. KRYPTON-TPLIF MEASUREMENTS IN NON-REACTING FLOW SYSTEMS

3.1 Experimental Apparatus

For cold-mixing studies, we used Kr as an inert tracer species and investigated the 5p’←←4p excitation transition of Kr at 204.1 nm with high-repetition-rate (1-kHz), high-intensity fs-duration laser pulses (part of this work has been published in [131]). The 204.1-nm excitation can be particularly advantageous in practical implementations as this wavelength can be easily accessible using a more efficient, fs fourth-harmonic generation scheme [133]. We also investigated the potential of that excitation/detection scheme for mixture-fraction imaging in turbulent flow fields. As shown in Figure 5, in the 204.1-nm excitation scheme, the prominent fluorescence detection that has been used in previous studies is at 826 nm from the 5p’[3/2]$_2$→5s’[1/2]$_1$ decay [134]. However, other possible fluorescence pathways from the 5p’ excited state are also possible. A complete description of such fluorescence channels is lacking in the published literature. Hence, we have first performed a comprehensive investigation of wavelengths and relative intensities of fluorescence emission lines following the 204.1-nm fs excitation of ground-state Kr. Subsequently, high-repetition-rate imaging studies were also conducted to explore the potential of this scheme for turbulent mixing studies in dynamic flow fields.

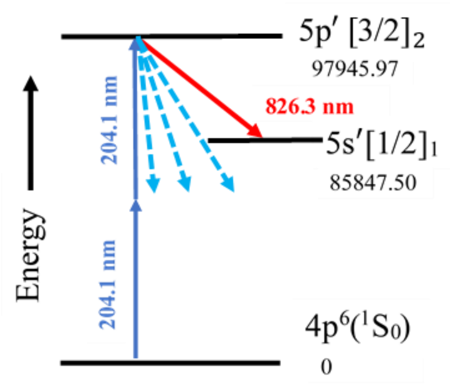

Figure 5. TPLIF excitation/detection scheme for Kr. Level energies shown underneath each level notation are in cm^{-1}. Other potential fluorescence pathways from the 5p′ excited states that were investigated in this work are represented by dotted lines.

The schematic diagram of the Kr-TPLIF experimental apparatus is shown in Figure 6. It consists of a regenerative-amplified fs Ti: Sapphire laser system (Spectra Physics, Model: Solstice Ace), for generating approximately 80-fs full-width at half-maximum (FWHM) laser pulses at 1-kHz repetition rate. The typical output energy was approximately 6 mJ/pulse at 800 nm. The output laser beam was split into two parts, one part with approximately 4.9 mJ of laser energy was used to pump an optical parametric amplifier (OPA) (Light Conversion Model: TOPAS Prime Plus with a NirUVis UV extension module). In OPA, the pump beam was then split into two parts, small fraction of the pump beam was used to produce white-light continuum (WLC) in a sapphire plate and amplify the WLC in the first stage. Majority of the pump beam was used to amplify the WLC in the second stage to obtain signal and idler wavelengths through a parametric conversion process. The 1730-nm idler beam was mixed with the fundamental 800-nm beam to generate 547.6-nm beam and then frequency-doubled to convert the beam to

273.6 nm, and finally that beam was sum-frequency mixed with approximately 1.1 mJ of the fundamental 800-nm beam to produce UV radiation near 204.1 nm with average energy of 13 µJ/pulse. The 204.1-nm beam was passed through several 45^o dielectric laser mirrors (Lattice Electro Optics (LEO), TWB-200-210-45-UF-1025) and a +200-mm-focal-length plano-convex lens (Thorlabs, UF-PX-25.4-200) to focus onto the probe volume. A thin, variable neutral-density (ND) filter (Thorlabs, NDC-100S-4M) was placed before the plano-convex lens to obtain different laser pulse energies at the probe region.

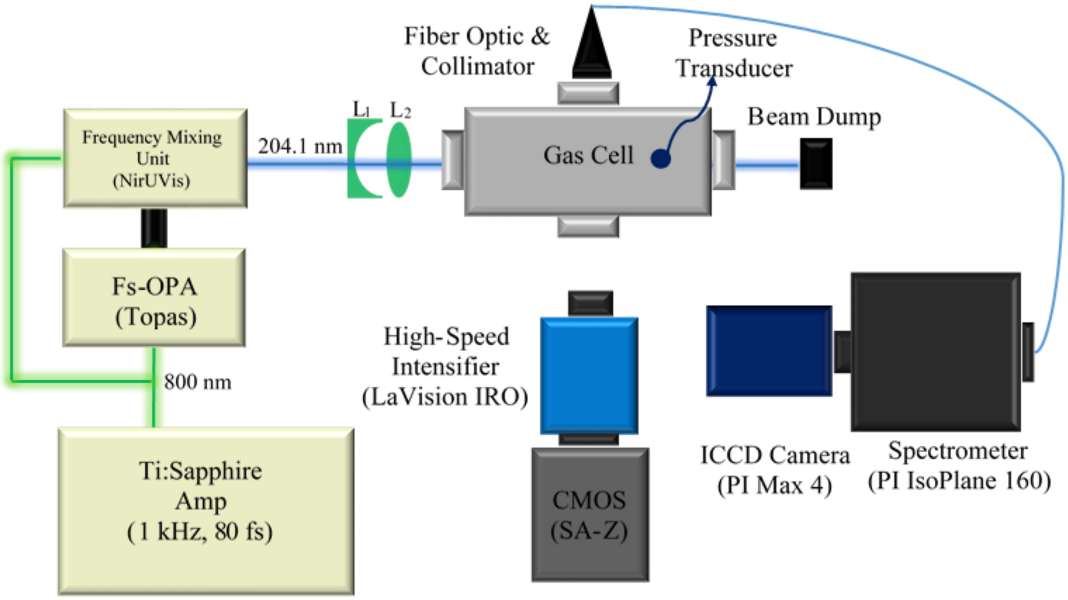

Figure 6. Experimental apparatus for Kr-TPLIF. For the imaging measurements, the gas cell was replaced by an open gas jet.

For spectroscopic studies, a high-pressure gas cell having orthogonal optical windows, was placed in the probe region. Prior to the measurements, the cell was evacuated using a vacuum pump, then filled with pure Kr (research grade) or mixtures of

Kr with other buffer gases. The mixtures were prepared based on the partial pressure of each gas. The cell pressure was monitored using an Omega pressure transducer (Model: PX409-150AUSBH). The fluorescence signal was collected orthogonal to the pump beam path using a fiber collimator and was guided through a 19-core optical fiber onto a spectrometer (Princeton Instruments, Model: IsoPlane 160) coupled with an intensified CCD (ICCD) camera (Princeton Instruments, Model: PI-Max4). The spectrometer has gratings of 300, 1200 and 3600 grooves/mm for low-, medium-, and high-resolution spectral studies. Before characterizing the spectral lines and their relative line strengths using the spectrometer/ICCD camera system, the wavelength and intensity calibrations were conducted using a set of calibration lamps (Princeton Instruments, Model: IntelliCal®) consisting of dual Hg and Ne-Ar atomic emissions, and a calibrated LED-based light source, respectively.

For 2D high-speed imaging measurements in turbulent non-reacting flow fields, the gas cell was replaced by an axi-symmetric gas jet. The inner diameter of the jet tube is 4.76 mm, and 50.8 mm for co-flow region. A +100-mm-focal-length plano-convex lens (LEO, UF-PX-25.4-100-200-230) coupled with a f=-25 mm plano-concave cylindrical lens (Thorlabs, UV LK4767) was used to generate approximately a 25-mm high laser sheet. A 50-mm-focal-length f/1.2 camera lens (Nikkor) was used to collect the fluorescence signal and focus it onto a complementary metal-oxide semiconductor (CMOS) camera (Photron, Model: SA-Z) coupled to a high-speed intensifier (Lavision, Model: HS-IRO). The high-speed camera/intensifier system was capable of capturing turbulent dynamics with sufficient spatial and temporal resolutions.

3.2 Results and Discussion

The Kr fluorescence emission spectrum recorded, using pure krypton at 1-bar cell pressure, is shown in Figure 7. The laser pulse energy at the probe region was 3.65 μJ/pulse (approx. 4.65×10^4 μJ/cm^2). The intensifier gate width and gain were set at 10 ns and 50%, respectively. The spectrum shown is an average of 100 frames with each frame containing on-chip accumulation of 200 laser shots. It can be seen that a series of strong and weak spectral lines were observed in addition to a commonly reported fluorescence emission line near 826.3 nm (line i) [134]. The insets in Figure 7 show parts of the spectra with the vertical scale expanded 40× in order to better illustrate the weaker emission lines. A 300 lines/mm grating was used in the IsoPlane 160 spectrometer. The entire detection channel has spectral resolution better than 0.2 nm.

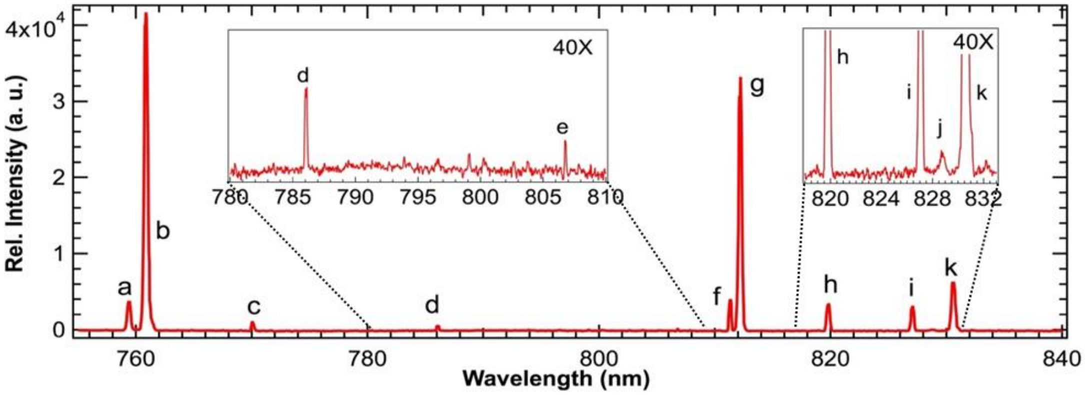

Figure 7. Experimentally recorded fs-TPLIF emission spectra of Kr. For better clarity, the vertical axis is scaled by 40× in the regions shown in insets.

To verify that these spectral lines originate from Kr fluorescence emissions, we compared the observed spectral lines with the information given in the NIST Atomic Spectra Database [135], and the results are given in Table 1. The experimental spectrum

Table 1. Comparison of experimentally measured fluorescence emission spectral lines of Kr with NIST Atomic Spectra Database [135].

Line	Wavelength (nm)	Relative Intensity (a.u.)		Transition					
	NIST	NIST	Exp.	Lower Level	Term	J	Upper Level	Term	J
a	758.74	1000	2500	$(^2P^o_{3/2})5s$	$^2[3/2]^o$	1	$(^2P^o_{3/2})5p$	$^2[1/2]$	0
b	760.15	2000	30200	$(^2P^o_{3/2})5s$	$^2[3/2]^o$	2	$(^2P^o_{3/2})5p$	$^2[3/2]$	2
c	769.45	500	900	$(^2P^o_{3/2})5s$	$^2[3/2]^o$	2	$(^2P^o_{3/2})5p$	$^2[3/2]$	1
d	785.48	200	600	$(^2P^o_{1/2})5s$	$^2[1/2]^o$	0	$(^2P^o_{1/2})5p$	$^2[1/2]$	1
e	805.95	100	200	$(^2P^o_{1/2})5s$	$^2[1/2]^o$	0	$(^2P^o_{1/2})5p$	$^2[3/2]$	1
f	810.44	4000	4000	$(^2P^o_{3/2})5s$	$^2[3/2]^o$	2	$(^2P^o_{3/2})5p$	$^2[5/2]$	2
g	811.29	500	21600	$(^2P^o_{3/2})5s$	$^2[3/2]^o$	2	$(^2P^o_{3/2})5p$	$^2[5/2]$	3
h	819.01	300	3000	$(^2P^o_{3/2})5s$	$^2[3/2]^o$	1	$(^2P^o_{3/2})5p$	$^2[3/2]$	2
i	826.32	400	2500	$(^2P^o_{1/2})5s$	$^2[1/2]^o$	1	$(^2P^o_{1/2})5p$	$^2[3/2]$	2
j	828.11	200	100	$(^2P^o_{1/2})5s$	$^2[1/2]^o$	1	$(^2P^o_{1/2})5p$	$^2[1/2]$	1
k	829.81	500	4900	$(^2P^o_{3/2})5s$	$^2[3/2]^o$	1	$(^2P^o_{3/2})5p$	$^2[3/2]$	1

* J: total electronic angular momentum.

** The experimental relative intensity values (integrated line intensities) are scaled to match the relative intensities of the 810.44-nm line (f), which is the strongest emission line in the 750–840 nm spectral range as indicated in the NIST database.

is red shifted by approximately 0.2 nm, and all spectral lines in the 750–840-nm region (except the line at 768.52 with indicated relative intensity of 400 in the NIST database) are in a good agreement with the NIST database. The relative intensities of the observed LIF lines are also compared with the NIST values. It was observed the spectral lines at 760.15 and 811.29 nm are significantly stronger as compared to the strongest peak at

810.44 nm listed in the NIST database. It should be noted that, according to the NIST database, the relative intensities listed there are source dependent and should only be used as a rough guideline.

In addition to spontaneous fluorescence emission, other competing energy transfer processes, such as absorption, photoionization, stimulated emission and collisional quenching, can significantly interfere with the measured Kr-TPLIF signals in turbulent reaction-flow environments. Such processes would result in reduction of fluorescence signals and make the quantitative measurements much more complex. Furthermore, the collisional quenching is dependent on temperature, pressure and colliding species, it is necessary to investigate these effects before applying it into practical combustion measurements. The effect of seed concentration on the Kr-TPLIF signal investigated as a function of different buffer gases is shown in Figure 8. The Kr seed concentration increased from 0.1% to 10% (based on partial pressure) with different buffer gases, oxygen, air, nitrogen, helium and argon, then it further increased from 10% to 100% in the nitrogen gas. The total pressure was fixed at 1 bar. It can be seen in Figure 8 (a) that the normalized LIF signal scaled linearly with Kr concentration when the concentration was below 10%, although some deviation is observed in the helium-Kr mixture. We have also observed deviations from linear dependence at higher concentrations, in particular when Kr concentration is above 40% (as shown in Figure 8 (b)). This behavior may indicate that stimulated emission resulted in reducing the fluorescence signal at higher concentration. Hsu et al.[41] also stated that a threshold of mole fraction for stimulated emission in turbulent flame was 0.04. The effect of Kr seed concentration on the stimulated emission in turbulent flame environment is a topic for follow-on studies. Especially, at the same Kr seed concentration, the fluorescence signal increases with increase of the molecular weight of quenching partners. For instance, when the Kr seed concentration is 10%, the signals of Kr-He, Kr-Ar, Kr-N_2, Kr-Air and Kr-O_2 mixtures scale as 1, 0.42, 0.04, 0.02 and 0.01, respectively. These results show that He was the weakest quencher among all the buffer gases investigated in the current study. This observation could be explained by the fact that the higher mass of quenching partners generally has larger quenching cross sections. Hence N_2, air and O_2 are the most efficient quenchers. These gases are the most common constituents in fuel-air mixtures and hence, it is important to correct the fluorescence signals to obtain quantitative measurements when seeding krypton into fuel-air stream. These results, except in the case of nitrogen, are in a good agreement with those from Niemi et al.[134], where they measured the quenching coefficients of the 5p'$[3/2]_2$ state with various gases. Hsu et al.[41] also investigated the quenching rates of the 5p$[3/2]_2$ state and obtained the similar results. Other quenching partners, particularly in gaseous hydrocarbons, will be investigated in future studies. Moreover, many intermediate species are produced in flames and they all can be considered as quenching partners, one of the most efficient quenchers is water vapor. In general, water vapor quenching has a significant dependence on temperature and pressure. Moreover, the natural fluorescence lifetime of the 5p' excited state is about 26 ns [42], while it would reduce significantly due to collisional quenching effects in atmospheric-pressure flame environments. The evolution of fluorescence decay of the excited Kr in this study is shown in Figure 9. It is seen that the fluorescence lifetime is less than 2 ns and could be reduced further at elevated temperatures and pressures. Therefore, the utilization of ultrashort fs laser pulses shows the potential for a comprehensive quenching rate investigation of Kr.

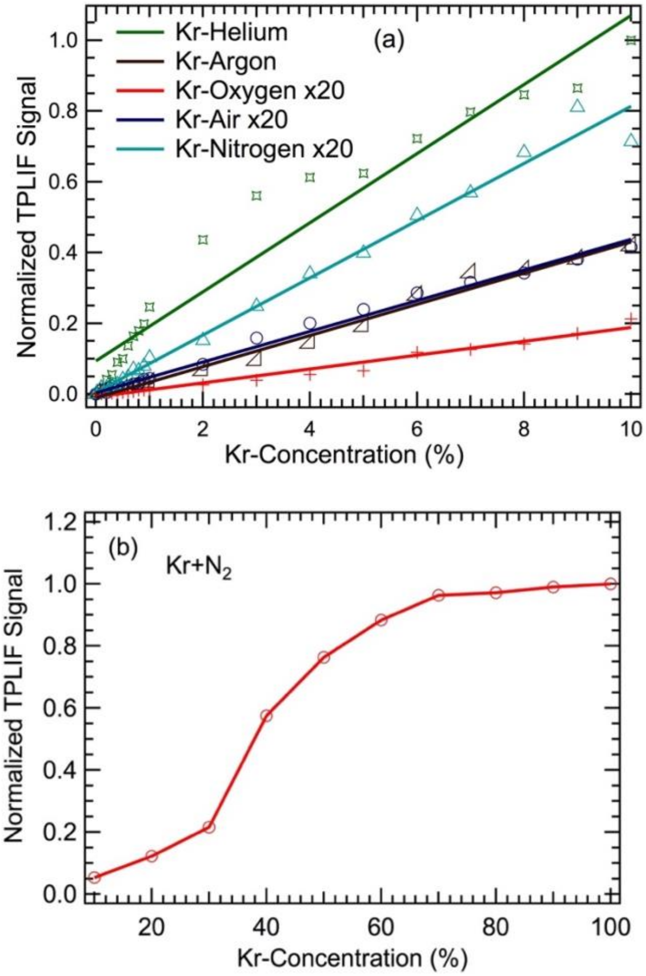

Figure 8. (a) Dependence of fs-TPLIF signal on Kr seed concentration at different buffer gases. The vertical scales of Kr-Oxygen, Kr-Air and Kr-Nitrogen data are expanded by 20× to show the profiles. (b) Dependence of the N_2 quenching where Kr-N_2 ratio is varied between 10-100%.

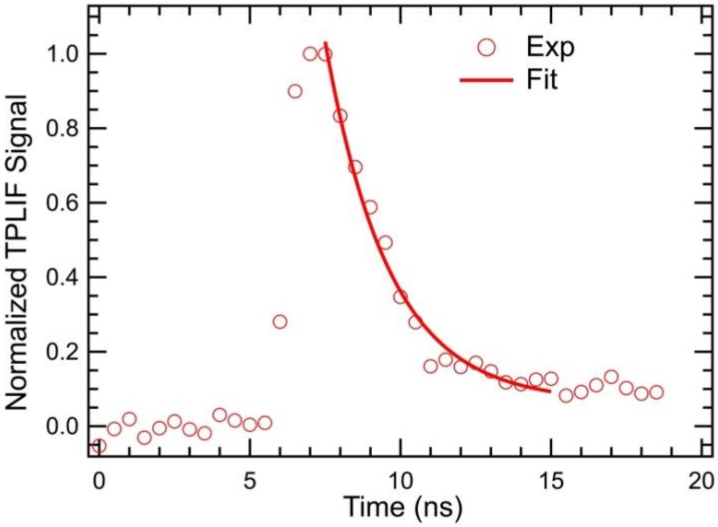

Figure 9. Fluorescence emission signal versus gate-delay time, shown with a single-exponential fit (solid line) of the Kr decay using pure krypton at 1-bar cell pressure.

Similarly, the dependence of fs-TPLIF fluorescence signal on total pressure was investigated and the results are shown in Figure 10. A mixture of 10% Kr was filled into N_2 buffer gas and the total pressure increased from 0.1 bar to 10 bar. The total pressure axis is plotted on a log scale. It can be seen that the relationship between pressure and the normalized LIF signal shows a good linear trend from 0.1 bar to 10 bar. This observation may indicate that other signal loss mechanisms such as photo-ionization and stimulated emission are negligible in this region under current experimental conditions.

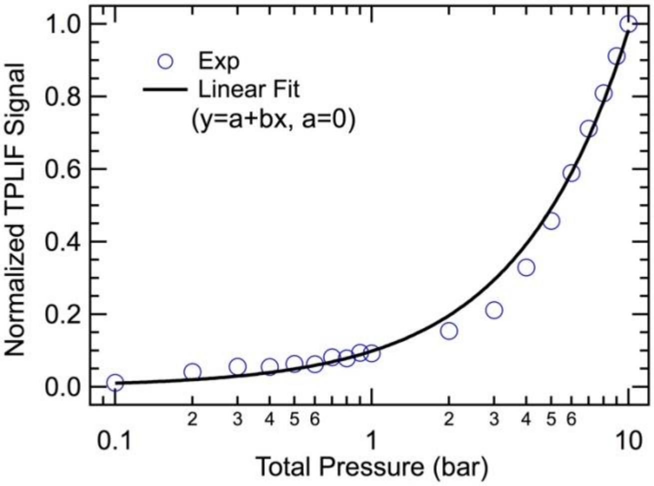

Figure 10. Dependence of fs-TPLIF signal of Kr on total pressure.

Theoretically, at low laser pulse energies, a linear dependence of the square root of the fluorescence signal on the laser pulse energy should be observed in a two-photon excitation process. Interfering schemes such as photoionization and stimulated emission would result in a lower dependence for higher laser pulse energy. The peak-normalized fs-TPLIF signal of atomic krypton in N_2-Kr and Ar-Kr mixtures as a function of the laser pulse energy is shown in Figure 11. The mole fraction Kr was 10%, and the total pressure was kept at 1 bar. For these measurements, we collected fluorescence emission signals using an 832-nm band-pass filter (Semrock FF01-832/37-50). It can be seen that a good linear relationship is observed within the experimental uncertainty, thus it is concluded that the Kr two-photon excitation did not reach saturation and free of photoionization and stimulated emission in the range of laser energies investigated in this experiment. As discussed previously [136], saturation, photoionization and stimulated emission processes would result in less than a quadratic laser pulse energy dependence.

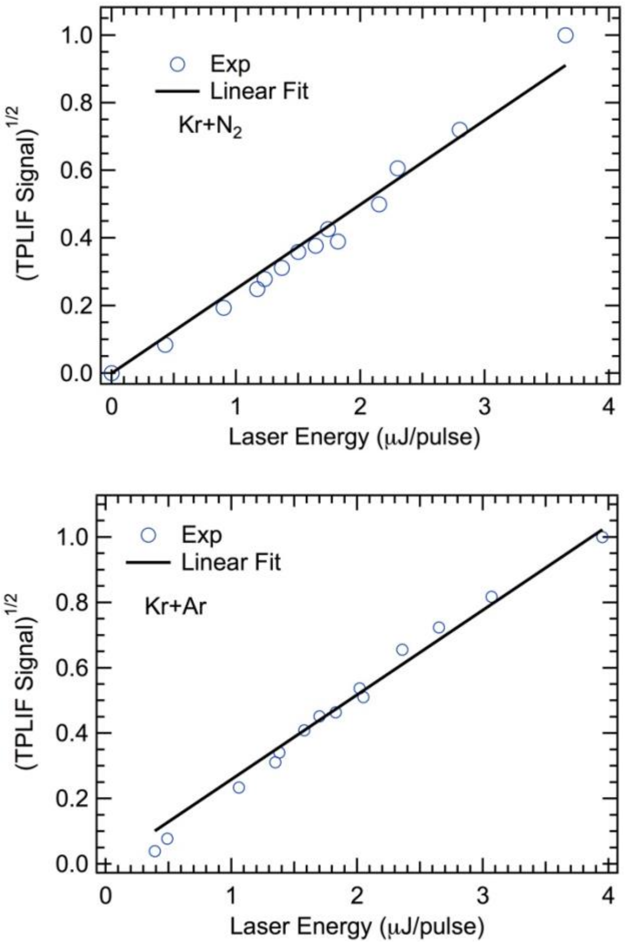

Figure 11. Dependence of fs-TPLIF signal of Kr on laser pulse energy.

In order to demonstrate the feasibility of the fs-pulse excitation/detection scheme of Kr for studies of mixture fraction in turbulent flow fields, we conducted a series of high-speed single-laser-shot 2D imaging experiments. The gas cell was replaced by an axi-symmetric gas jet. Figure 12 shows successive single-laser-shot raw images during the initiation and fully developed turbulent flow of the krypton jet in ambient air, recording at a repetition rate of 1 kHz. Since no interfering emissions were observed, the bandpass filter in the fluorescence collection channel was removed during these experiments. In

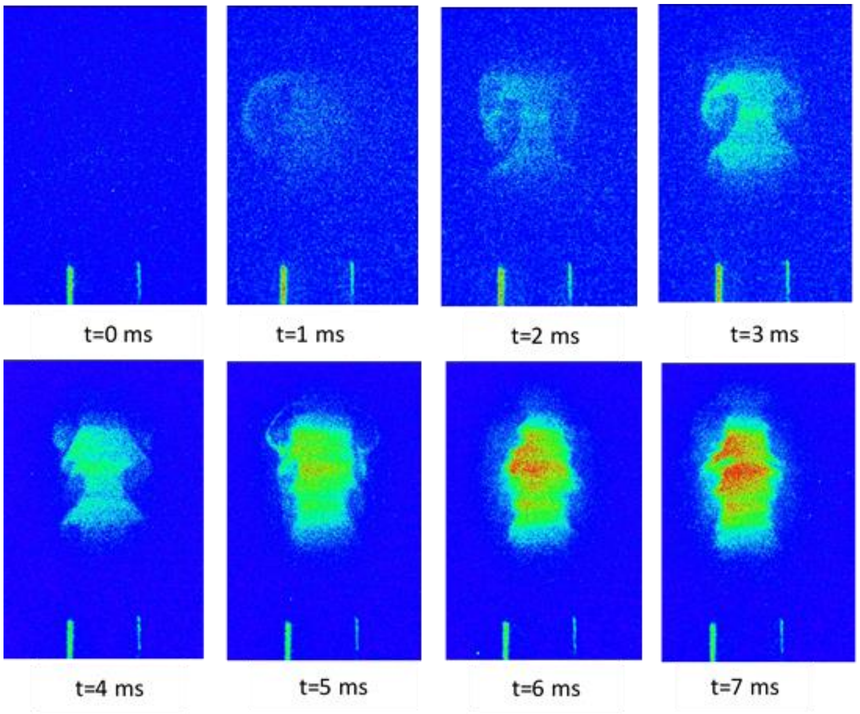

t=0 ms t=1 ms t=2 ms t=3 ms

t=4 ms t=5 ms t=6 ms t=7 ms

Figure 12. Successive single-laser-shot images recorded at the initiation of a krypton jet flow.

Figure 12, the peak single-laser-shot signal values reached approximately 2000 counts. The intensifier gain was set at 75% and the images were recorded at 1 kHz. It can be seen that large vortices were generated for the jet flow at t=1–4 ms, which indicates there was a strong mixing process at the initiation of the jet flow. The small amount of krypton and strong mixing contributed to a low relative intensity and less gradient of Kr-TPLIF signal from t=1 ms to t=4 ms. As further ejection of krypton jet flow transforming to a steady jet, the core of the jet flow has higher relative intensity and less gradient, while it had a lower relative intensity and large gradient towards the periphery of the jet flow due to shear flow and vortex shredding. Small vortex structures were also observed on the periphery of the jet flow.

4. CO-TPLIF MEASUREMENTS IN REACTING FLOW SYSTEMS

4.1 Experimental Apparatus

In this section, we investigate the potential of the cutting-edge, fs-duration, two-photon LIF technique for detecting CO and exploring possible interferences in gaseous and liquid-fuel flames (part of this work has been published in [137]). As discussed above, understanding CO formation becomes especially important in rich flame conditions, where significant levels of soot are also present. Furthermore, the additional phase change could challenge CO measurements using the LIF technique in liquid-fuel flames. Therefore, we investigated possible interferences in a range of CH_4, C_2H_4 and liquid CH_3OH flames. As shown in Figure 13, the radiation at 230.1 nm excites the CO molecules from ground state ($X^1\Sigma^+$) to excited state ($B^1\Sigma^+$), then the fluorescence from the $B^1\Sigma^+ \rightarrow A^1\prod$ Ångström band (400–600 nm) is detected. Furthermore, some CO molecules at $B^1\Sigma^+$ state relax to $b^3\Sigma^+$ state because of the collisional energy transfer in combustion systems, thus fluorescence signal could also be detected from the $b^3\Sigma^+ \rightarrow a^3\prod$ (282–380 nm) third positive band. It can be seen that excitation at 230.1 nm and detection in the third positive system could eliminate most of C_2 and CH interferences in the 400–600 nm region. However, the third positive system also exhibits stronger pressure and quenching effects as compared to the Ångström band [61]. More importantly, fluorescence occurs in the UV spectral region where detection cameras are generally less sensitive. Thus, in these experiments we use the Ångström band emission to detect CO, while accounting for various interferences in sooting flames. Comparison of previously employed ns- and ps-duration pulses for TPLIF, as described above, shows that the fs-duration excitation scheme has advantages of strong signal generation and less susceptibility to interfering photodissociation processes.

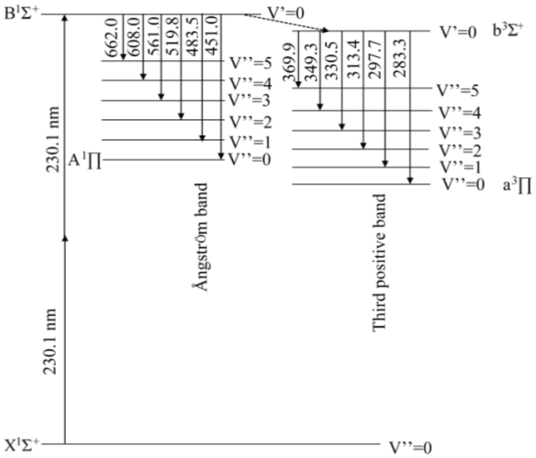

Figure 13. Energy level diagram for femtosecond two-photon LIF of CO.

The experimental apparatus, shown in Figure 14, consists of a fs-duration, Ti: Sapphire, regeneratively amplified laser system, generating approximately 80-fs-duration of laser pulses at 1-kHz repetition rate. The fundamental 800-nm beam was used to pump the OPA to generate signal beam at 1291 nm. Then, the signal beam at 1291-nm wavelength was frequency-doubled twice to generate 322.7 nm beam, then the 322.7-nm beam was sum-frequency mixed with a portion of the fundamental beam to produce radiation at 230.1 nm with average energy of 40 µJ/pulse. The UV laser beam was then guided to the probe region using several 45^o dielectric laser mirrors (LEO, TWB-210-230-45-UF-1025) and focused onto the probe region using a +200-mm-focal-length plano-convex lens (LEO, UF-PX-25.4-200-200-230). A thin, variable ND filter was placed before the plano-convex lens to adjust the laser pulse energy at the probe volume. The laser energy was monitored using a laser power & energy meter (Ophir, Fluke 8845A). the focal spot size of the excitation beam was measured using a beam profiling camera (Spiricon, BGS-USB3-LT655).

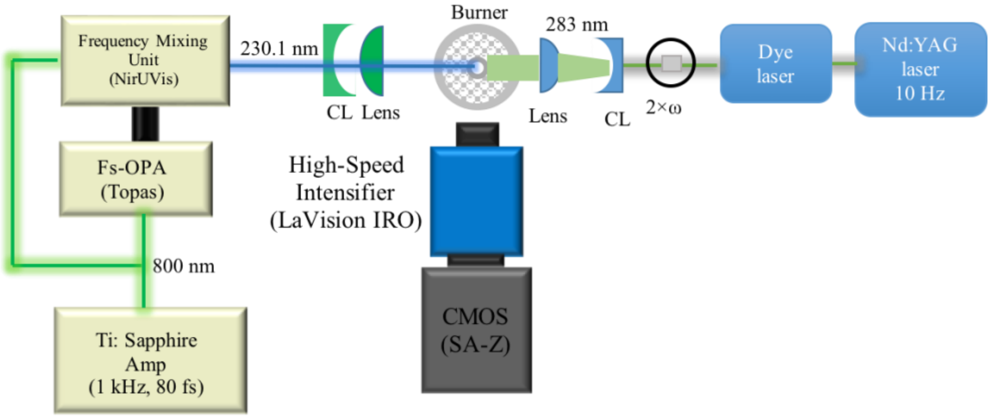

Figure 14. Schematic diagram of the experimental apparatus for fs-TPLIF of CO. Then ns OH-LIF measurement system used to characterize the reaction zone of the flames investigated is also shown on the right-hand side of the diagram (CL: Cylindrical lens).

For CO spectroscopic studies at elevated pressures, a static gas cell having an effective optical path of 20 cm and four orthogonal fused-silica windows was placed in the probe region (where the burner was located). A +500-mm-focal-length plano-convex lens (LEO, UF-PX-25.4-500-200-230) was used to avoid the laser-induced interferences of the C_2 swan band. The gas cell was vacuumed down to 10^{-3} Torr or better, using a vacuum pump, prior to filling in pure CO or mixtures of CO and other gases. The pressure was monitored using an Omega pressure transducer. A collimator coupled with a fiber optic cable was placed orthogonal to the beam path to collect the CO-TPLIF signal, which was transmitted to the entrance slit of the spectrometer using a fiber optic cable consisting of a circular-to-linear fiber array. The spectrometer has different gratings to obtain high-and low-resolution spectra for pressure effect studies. The vertical entrance slit width was set at 150 µm and the ICCD camera was mounted on the exit plane to record spectra. The spectrometer/ICCD camera system was wavelength and intensity calibrated using the Hg/Ne-Ar lamps and calibrated LED-based light source, respectively. For CO measurements in sooting flames, the gas cell was replaced by a 25.4-mm × 25.4-mm Hencken calibration burner, jet burner, or modified Mckenna burner (flat flame burner) coupled with an injector to achieve various flame conditions. The fuels used were methane (CH_4), ethylene (C_2H_4) and liquid methanol (CH_3OH). The flow rates of gases were regulated by mass flow controllers (MKS Instruments, GE50 series), which were connected to a gas system controller (MKS Systems, Model 946). Variable equivalence ratios from very lean to rich conditions could be realized by adjusting the flow rates of gases in gaseous sooting flames. The flow rate of liquid methanol (research grade, >99.5%) was controlled by a syringe pump (New Era Pump Systems, NE-1000). Fluorescence signal collected orthogonal to the beam path using an intensified CCD (ICCD) camera (Princeton Instruments, Model: PIMax4). The detection gate width and gain of the ICCD camera were varied for the spectroscopic and imaging measurements to further suppress laser scattering and flame background.

The experimental apparatus for the two-line OH-PLIF thermometry in liquid-spray flames described in the next section is shown on the right-hand side of Fig. 14. Single photon rotational transitions of $Q_1(5)$ (283.750 nm) and $Q_1(14)$ (286.456 nm) of the OH $A^2\Sigma^+$-$X^2\prod$ (1,0) band are used, and subsequent fluorescence from the OH $A^2\Sigma^+$-$X^2\prod$ (0,0) and (1,1) bands is detected. The experimental apparatus, shown in Figure 14, has a 10-Hz nanosecond-duration Nd: YAG laser (Continuum, Model Powerlite 8000), operating at 1064-nm wavelength. The 1064-nm beam was frequency doubled to generate a 532-nm green beam, then the green beam was used to pump a dye laser (Continuum, Model ND6000). The tunable dye laser output around 565.5 nm or 572.912 nm was subsequently frequency doubled in a beta-barium borate (BBO) crystal to obtain UV radiation in the 282.75 nm or 286.456 nm wavelengths. The output wavelength of the dye laser was monitored using a wavelength meter (Highfinesse, Model WS-7). The UV laser energy was fixed at 6 mJ/pulse for both excitation wavelengths. Then the UV beam was guided to the probe region using several dielectric laser mirrors (LEO, TWB-275-285-45-UF-1025). A +200-mm-focal-length plano-convex lens coupled with a f=-25-mm plano-convex cylindrical lens was used to generate a laser sheet with an effective height of approximately 42 mm. The beam sheet profile was monitored using a beam profiling camera (Spiricon, BGS-USB3-LT665), which has a resolution of 2752×2192 with a 4.4-um square pixels. The fluorescence signal was collected orthogonal to the beam path using the ICCD camera fitted with a 45-mm, f/1.8 UV camera lens (Cerco). A 315-nm bandpass filter (Semrock, FF01-315/15-50) was mounted at the front end of the camera lens to block the laser scatter and to collect only the fluorescence emission bands. The detection gate width was set to 100 ns to minimize background interferences from flames.

4.2 Burner Facilities

The Hencken calibration burner shown in Figure 15, is widely used to produce near-adiabatic premixed flames. It consists of a square honeycomb structure of 37.5

mm×37.5 mm and an uncooled burner holder which is divided into a central flow region of 25.4 mm× 25.4 mm and a surrounding co-flow region. Within the central region, the honeycomb supports stainless-steel fuel tubes in every other honeycomb cell. The fuel and oxidizer are supplied into fuel tubes and nearby honeycomb cells, respectively, then rapidly mix just above the burner surface, forming an array of blended diffusion-like flamelets which quickly mix into a uniform premixed flame region. The main flame region is surrounded by an annular shroud, which flows a non-combustible gas co-flow to create a shroud for the main flame. The total flow rate of this inert gas could be adjusted to match the flow from the central region, therefore reducing shear instabilities between the flame gases and the surrounding environment. The Hencken burner is mostly used as calibration reference sources in laser diagnostics because it is capable of generating a steady state of equilibrium products above the reaction zone [138, 139].

Another type of burners used for CO measurements in liquid-fuel spray flames is a modified McKenna burner (Holthuis & Associates, Flat Flame Burner) [94, 103]. A schematic of the McKenna burner is shown in Figure 16 (a). The McKenna burner has a stainless steel (SS) porous plate of 60-mm diameter with a central tube of 9.5 mm OD × 7.8 mm ID, allowing the introduction of a nebulizer to generate a fuel spray. A 73.5-mm OD, sintered bronze annular shroud enables a gas flow for stabilizing spray flames by minimizing shear perturbations. The burner plate has a coil sintered into it for flowing cooling water in and out to prevent the burner from overheating.

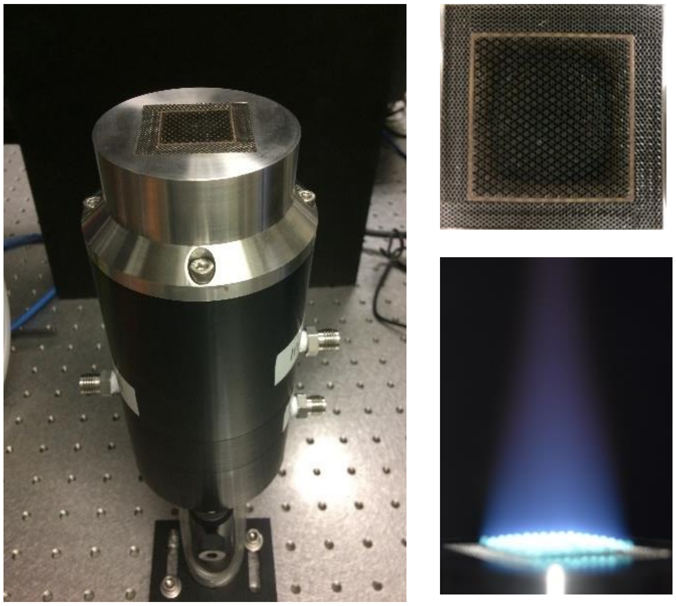

Figure 15. Photograph of the Hencken calibration burner used for CO measurement studies in the laboratory.

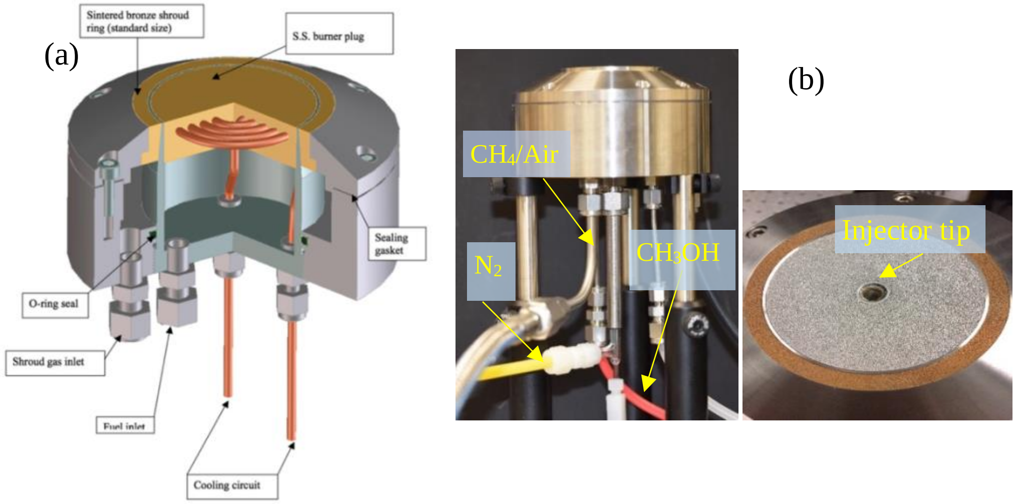

Figure 16. (a) A schematic diagram of the McKenna Burner [140]; (b) Photographs of the modified McKenna burner with a direct-injection high-efficiency nebulizer (DIHEN) used in CO and OH measurements [94, 103].

A glass nebulizer (Meinhard, DIHEN-170-A0.5) was used to atomize the liquid fuel supplied through a syringe pump. The schematic diagram of the nebulizer is shown in Figure 17, The high-speed atomizing gas flowing in the annulus passage having an area of 0.0094 mm^2 entrains the slow liquid fuel flowing in the central 104-µm diameter capillary tube. With this configuration, fine liquid-fuel droplets of diameter less than 40 µm are achievable downstream of the nebulizer exit [94].

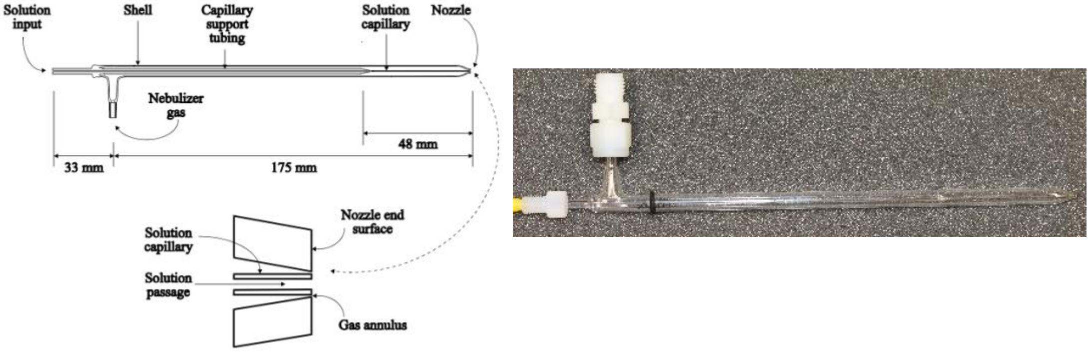

Figure 17. A schematic diagram (left) and a photograph (right) of the DIHEN nebulizer reprinted from [141].

To obtain piloted liquid-spray flames, the nebulizer was passed through the central tube of the McKenna burner. The nozzle exit was held approximately 3 mm below the porous plate surface to prevent the nozzle tip from overheating. After the premixed CH_4/air pilot flame was stabilized in the porous core of the McKenna burner, the liquid methanol fuel was pumped into the nebulizer using the syringe pump, atomized at the exit with the high-speed gas (N_2) flowing in the annular area. Fine droplets are gradually vaporized and burnt downstream of the exit. Various piloted liquid-spray flames (i.e. fuel types and flow rates) can be achieved using this configuration. The flow rates of CH_4, dry air (oxidizer), dry air (shroud gas), and N_2 (atomizing gas) were 0.8, 9.52, 15, and 0.27 slm, respectively. The liquid fuel flow rates used for flame 1, 2, and 3 were 15, 30, and 45 ml/h, respectively. The effective Reynolds number at the nozzle exit was approximately 3200 for all three cases.

The general appearances of spray flames were recorded using a digital SLR camera. Flame images corresponding to the three methanol flow rates are shown in Figure 18. As shown by these images, there is a region of light blue emission close to the burner surface corresponding to the CH_4/air pilot flame, and a yellow/orange zone further downstream corresponding to the spray flame. A ‘dark core’ region can also be seen in the bottom part of the spray flame, which corresponds to the fuel spray that has not fully evaporated yet, and fine droplet clusters are surrounded by a flame envelope in the periphery. Karpetis and Gomez [90] observed that the droplet concentration vary by two orders of magnitude along the centerline of spray flame, and between two to four orders of magnitude across the radial direction. With the spray flame spreading in the radial direction, the fuel droplet concentration decreases along the axial direction because of the spreading of the jet, as well as the droplets evaporate and eventual combust. The spray flame becomes longer as the liquid flow rates are increased. The droplet concentration increases with increasing flow rate of liquid fuel, resulting in increase in the local fuel vapor fraction, and hence, longer gaseous diffusion flames surrounding the droplet clouds.

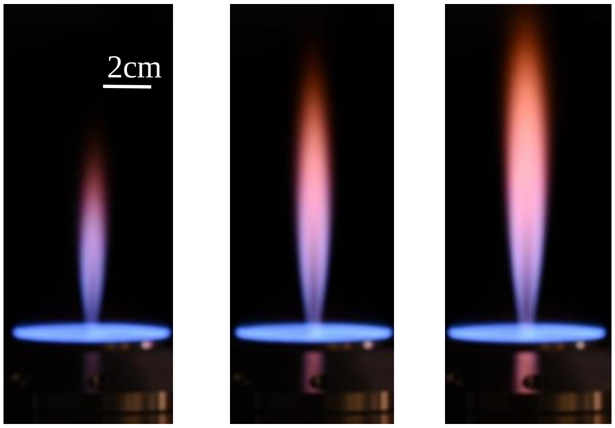

Flames 1
(15 ml/h)

Flames 2
(30 ml/h)

Flames 3
(45 ml/h)

Figure 18. Digital photographs of spray flames 1, 2 & 3.

4.3 Results and Discussion

4.3.1. Spectroscopic Study of fs-TPLIF of CO

The effect of excitation wavelength on the CO fs-TPLIF signal level was studied by recording line images of CO-TPLIF emission in a $\Phi=1.2$ CH_4/air flame stabilized over the Hencken burner. The spectrum of the excitation radiation was monitored using a fiber-coupled spectrometer (Ocean Optics, Model Flame S). Typical excitation laser spectra and corresponding CO TPLIF signals are shown in Figure 19. It shows that the fluorescence signal increases and then decreases as excitation central wavelength scans from blue to red, and the signal peaks at around 230.1 nm. Therefore, 230.1-nm excitation wavelength was used for all subsequent CO measurements in various sooting flames.

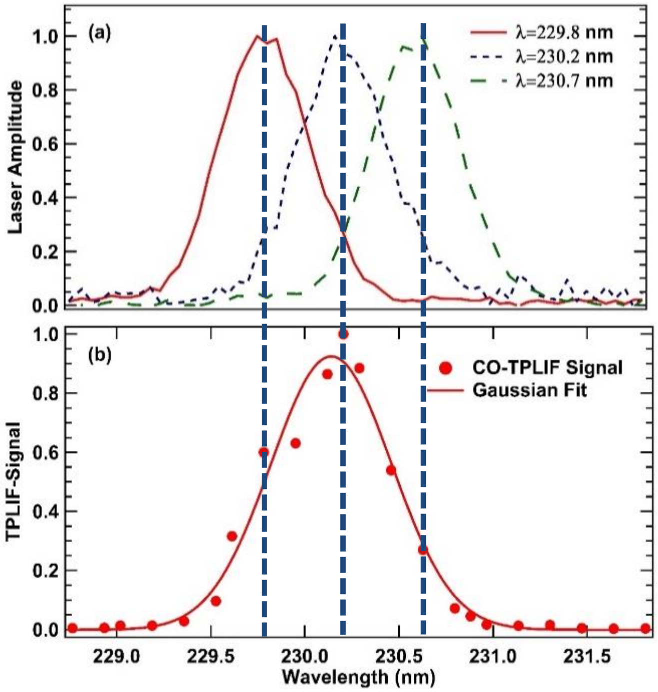

Figure 19. (a) Typical laser spectra of the excitation wavelength; (b) Dependence of the fs CO-TPLIF signal on the excitation wavelength. The integrated experimental signal is shown by red dots, and a Gaussian fit through data is shown by the solid line. The vertical dashed lines represent the central wavelength of the selected excitation spectrum.

The CO fs-TPLIF emission spectra following the 230.1-nm excitation scheme were studied first using pure CO filled in the gas cell at a pressure of 1 bar. The resultant fluorescence emission spectrum is shown in Figure 20. The spectrometer wavelength was calibrated using the calibration lamps discussed above. The fluorescence emission bands were detected at approximately 451, 483, 519, 561 and 608 nm in the Ångström band ($B^1\Sigma^+ \rightarrow A^1\prod$). Furthermore, because of the close energy level between the $b^3\Sigma^+$ triplet state and the $B^1\Sigma^+$ singlet state [142], the fluorescence emission could be also seen in the region of 282–380 nm originating from the third positive band ($b^3\Sigma^+ \rightarrow a^3\prod$) through collisional population. Both bands were verified to originate from CO radicals by tuning the laser wavelength away from the CO resonance peak.

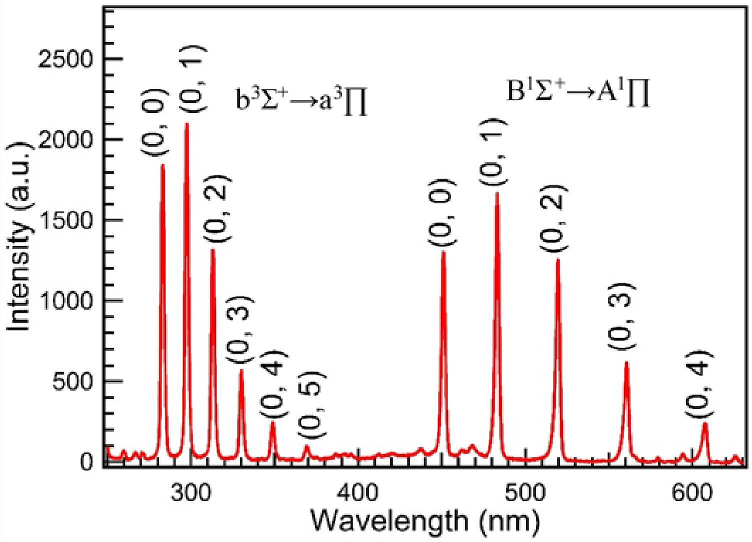

Figure 20. Experimentally recorded fs-TPLIF emission spectra of CO using pure CO in gas cell at 1-bar pressure.

A major complication for quantitative CO measurements using the 230.1-nm two-photon transition scheme is interferences from the C_2 Swam band. Such interferences effectively limit the number of available emission lines for CO detection, thereby limiting the collected signal levels. At higher laser energies, laser-generated C_2 interferences could be present in the fluorescence emission spectra. It is seen that the spectra shown in Figure 21 have several extra spectral lines at 437 nm, 468 nm, 515 nm and 590 nm as compared to those in Figure 20, indicating that the laser-generated C_2 signals present using the CO-TPLIF technique. Furthermore, the strong spectral peak observed at 460 nm is expected to be the second order of the diffraction grating of the 230-nm excitation beam.

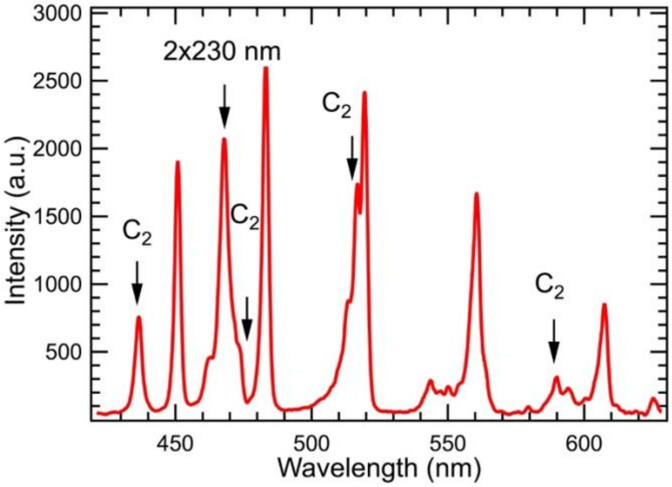

Figure 21. Interference investigation on fs-TPLIF of CO using pure CO in gas cell at 1-bar pressure.

In combustion environments, other possible interferences besides the C_2 interferences could exist because complex emission structure from other hydrocarbon molecules, for example. Shown in Figure 22 is the fluorescence spectra recorded in a C_2H_4/air sooting flame with equivalence ratio Φ =1.5 for three different intensifier gate widths of 10, 100 and 1000 ns. In these spectra, the wavelength and relative intensity have been calibrated for the spectrometer/ICCD camera system. The excitation laser energy used was 40 µJ/pulse. The isolated CH emission signal near 430 nm, as well as the C_2 isolated signals at approximately 437 nm and 468 nm, 515 nm partially overlap with the CO spectral lines. These laser-generated C_2 emissions were also confirmed by observing the emission spectrum at the 10-ns detection gate while detuning the excitation laser away from the resonance peak. Hence, we conclude laser-generated C_2 interference has a pronounced effect on CO fluorescence signal in fuel-rich flames. The C_2 production could be originated from photolysis of CO or soot, or three-photon dissociation processes in the vinyl radical (C_2H_3) and acetylene (C_2H_2) under fuel-rich conditions [59, 84]. Furthermore, the C_2 signal contribution becomes severe with increasing detection gate width of the ICCD camera from 10 to 1000 ns, for example, The C_2/CO peak signal ratio increases from 0.26 to 1.2 near 483-nm spectral line. More importantly, with increasing detection gate width, the overlapped regions between the isolated CO peaks around 451 and 483 nm and C_2 spectral lines are broadened at the base. This effect can be seen clearly in Figure 22 (c) as compared to Figure 22 (a) & (b), indicating that C_2 interferences became evidently predominant at wider detection gates. From the spectral data shown in Figure 22 (a)-(c), it was concluded that while a shorter, 10-ns detection gate width can effectively eliminate nascent flame C_2 emissions, laser-generated C_2 interferences can still be present under these conditions. Furthermore, the temporal evolution of CO and C_2 fluorescence signals as a function of gate delay is shown in Figure 23. The gate width was 0.45 ns and the position of the fs laser pulse was around 0.2 ns where the emission signals started to rise. It indicates that the effective lifetime of CO reduced to be in a picosecond-scale range, in an agreement with measurements from other publications [76, 78]. In addition, the fluorescence signal of CO and C_2 peaks simultaneously and it is not easy to block C_2 interferences using a delay-timing method. Thus, we incorporated a short detection gate and a narrow-band pass filter (Thorlabs, FB450-10) to select the CO (0,0) Ångström band only for CO-TPLIF measurements in sooting flames. The transmission curve of this filter is also shown by dotted lines in Figure 22. Although this spectral filtering method also blocks portion of the CO fluorescence signal, we conclude that is an important measurement to ensure the quantitative TPLIF detection of CO in heavily sooting flames.

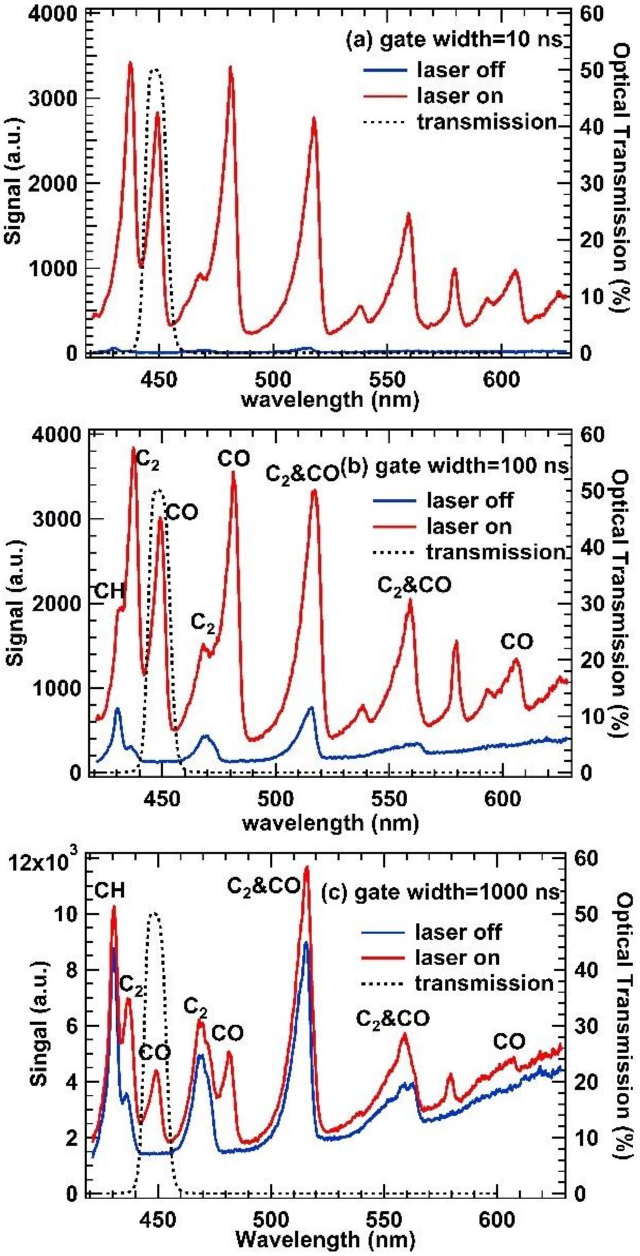

Figure 22. C_2 interference for CO fluorescence in a premixed C_2H_4-air flame with equivalence ratio Φ=1.5. Detection gate width of (a) 10 ns, (b) 100 ns, and (c) 1000 ns.

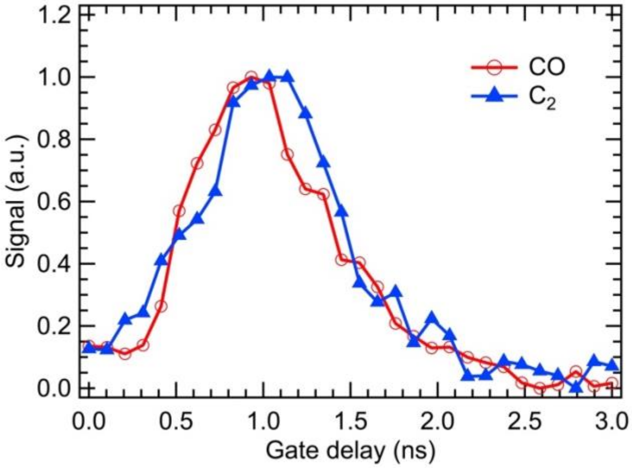

Figure 23. LIF signal vs. gate delay recorded in a premixed C_2H_4-air flame with equivalence ratio Φ=1.5.

The C_2 spectral interferences were also investigated more carefully using a 3600 grooves/mm grating present in the same spectrometer. Although improved C_2 emission filtering may be possible by incorporating a custom-designed bandpass filter, such implementation is not justifiable because of the substantial additional cost and the possibility of variation in the spectral bandwidth due to minor angular changes when mounting the filter.

4.3.2. Spectroscopic Study of CO-TPLIF at Elevated Pressure

Many previous studies on CO-TPLIF measurements have been performed in atmospheric-pressure conditions, which are not necessarily representative of combustion conditions in practical engine devices. At elevated pressure, collisional effects such as line broadening and collisional quenching, and absorption/trapping interferences increase as well as spectral line broadening and shifting can take place. The shift and broadening excitation pulses can lead to redistribute excited state populations and also reduce the excitation quantum efficiency in certain cases. The effect of pressure on the broadband, fs excitation pulses is shown in Figure 24. All spectra were recorded in a mixture of CO/N_2 (CO:N_2=10:90), and each spectrum is normalized to its peak value. It can be seen that the excitation spectra broaden slightly as pressure increases from 1 bar to 20 bar, such that the FWHM of excitation spectrum becomes 1.09 nm at 20 bar as compared to 1.02 nm at 1 bar. These broadening effects however, can be neglected as compared to the FWHM of all excitation spectra and therefore, has less influence on the excitation quantum efficiency of the LIF technique. However, it is reported that a higher pressure could broaden and significantly shift the narrow spectral transitions and therefore can be problematic when using narrowband excitation ns pulses [143].

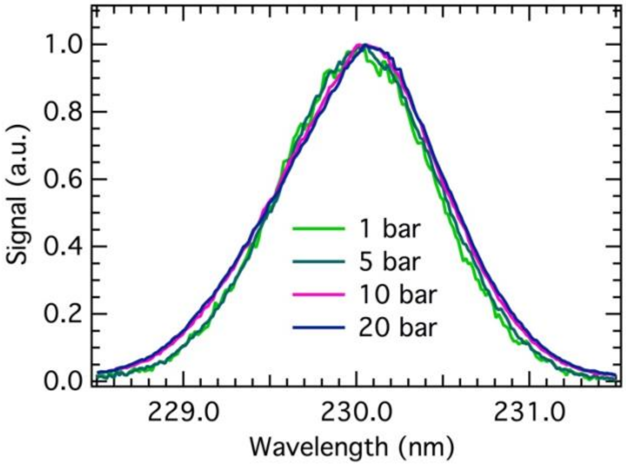

Figure 24. Dependence of the fs CO-TPLIF excitation spectrum on the total cell pressure.

Furthermore, the fluorescence emission spectrum of CO was recorded in the mixture of CO/N_2 using a 150 lines/mm grating. Figure 25 shows only the spectrum of the

CO B→A (0, 1) fluorescence band. The width of the vibrational band increases as pressure increases, such as the FWHM is 3.66, 3.68, 3.68, 3.85 and 3.89 at a pressure of 1, 5, 10, 15 and 20 bar, respectively. The collisional broadening of each rotational line increases with the increase of pressure and thus broaden the entire vibrational manifold. However, the broadening effects are comparatively small with respect to the FWHM of each spectrum.

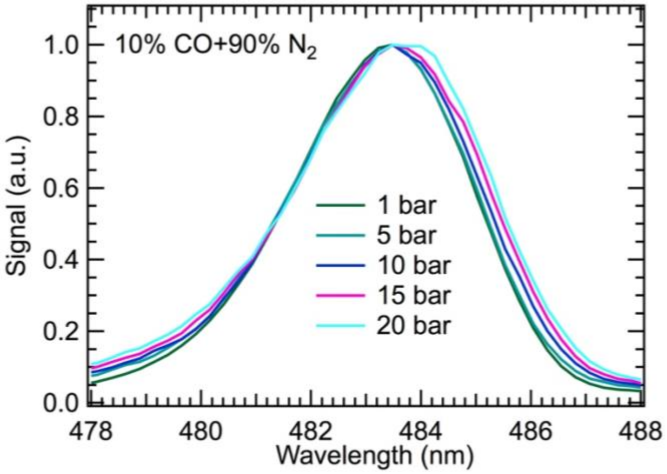

Figure 25. Dependence of the CO B→A (0, 1) fluorescence band on the pressure.

In theory, the fluorescence signal is proportional to I^m where m=2 for the CO-TPLIF process at lower laser intensities. However, other simultaneous competing processes such as photoionization and collisional quenching would reduce the quadratic dependence. The fluorescence signal recorded as a function of the laser pulse fluence in a mixture of 10% CO in N_2 at 1, 5, 10 and 20 bar is shown in Figure 26. At 1-bar cell pressure, the fluorescence signal exhibits a laser fluence dependence I^m where the exponent m=1.86 when the laser fluence is below 0.11 J/cm^2, and it drops down to 1.27. At lower laser pulse intensities, it appears that the signal does not reach saturation or losses

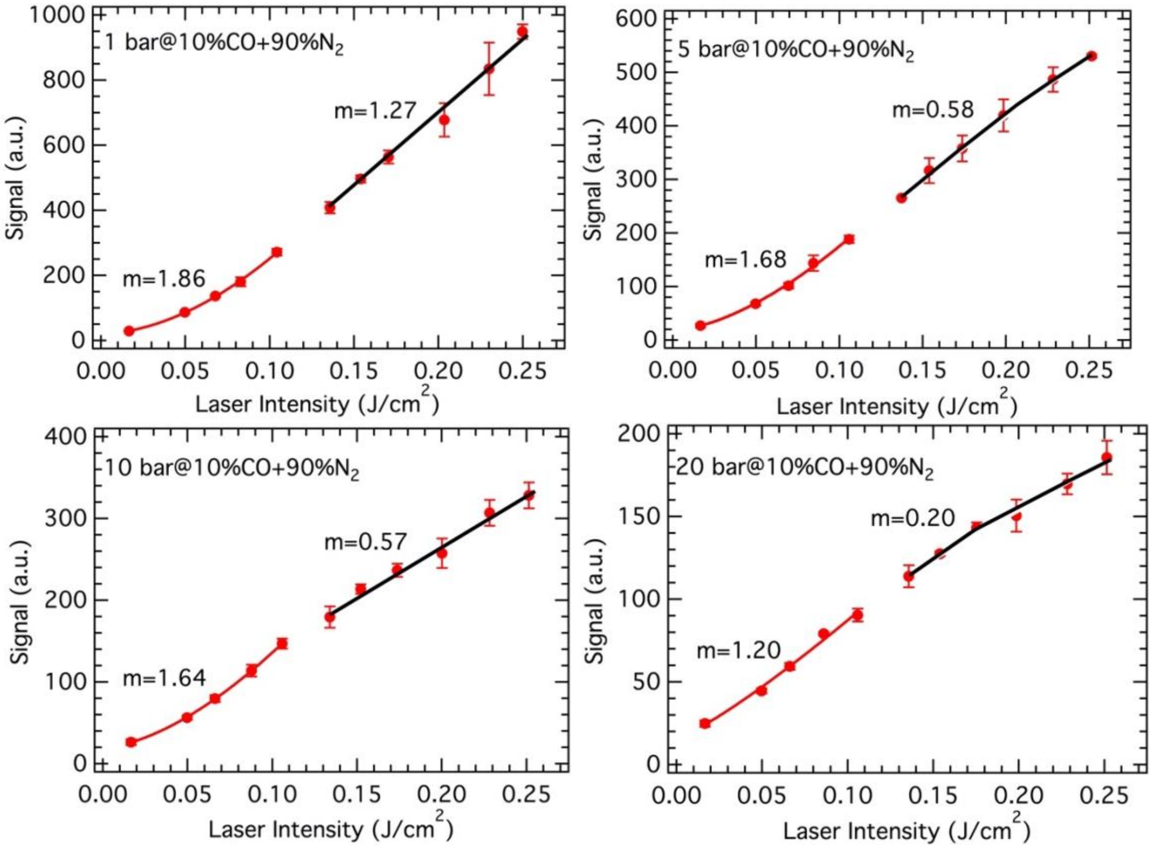

Figure 26. Laser pulse fluence dependence of the fs-TPLIF of CO signal in a mixture of 10% in N_2 at various pressures.

of signal due to stimulated emission and photoionization processes. While the photoionization process begins to dominate over other processes at higher laser intensities. Consequently, all following measurements were conducted below the laser fluence of 0.11 J/cm^2 for elevated-pressure studies. This behavior is also present at higher pressures, such as the exponent *m* decreases from 1.68 to 0.58 with increasing laser fluence at a 5-bar total pressure. In addition, the exponent *m* decreases gradually with the increase of total pressure in the range of laser intensities investigated. For instance, the exponent *m* drops from 1.86 to 1.20 at lower laser intensities when the total pressure rises up to 20 bar, and it reduces from 1.27 to 0.20 at higher laser intensities. The collisions between CO molecules and quenching partners increase with increasing pressure, therefore, the excited molecules non-radiatively decay to lower states resulting in sub-quadratic dependence. Di Rosa et al. [79] also stated that the peak two-photon rate coefficient of CO B←X (0, 0) decreased at elevated pressure.

As compared to traditionally used ns laser pulses, recent studies have shown that the ultrashort, fs laser pulses have numerous advantages in terms of photolytic-interference-free and high-repetition-rate measurements. According to the Heisenberg's uncertainty principle, the fs laser pulses have much wider bandwidths than ns laser pulses. To demonstrate the broadband feature of fs laser pulses that can provide additional advantages in the CO-TPLIF scheme, we compared the effect of pressure on fluorescence signals followed by the ns and fs transition schemes. For a comparison purpose, we used an identical mixture of constant mole fraction of 2.6% CO diluted in N_2/O_2 ($N_2:O_2=80:20$) [144] and a mixture of 2.6% CO in N_2. The variation of the fluorescence signal as a function of total pressure is shown in Figure 27. It is seen that the fluorescence signal decreases by 30% for the fs-excitation scheme and 60% for the ns-excitation scheme, as the total pressure increases from 1 to 13 bar. Furthermore, the LIF signal reduces only by 40% for the fs scheme as the total pressure rises up to 20 bar. For the mixture of 2.6% CO in N_2, the signal drops by 55%. The reduction of the LIF signal in fs excitation scheme is still lower than that of the ns excitation scheme, indicating that the fs scheme has a higher quantum efficiency than the ns scheme at elevated pressure. The broadband fs excitation pulses provide multiple excitation transitions simultaneously as compared to the single line excitation by ns pulses. At higher pressures, the ns excitation laser pulses asymmetrically broaden and shift, and can result in a reduction of the quantum efficiency [143], whereas, broadening effects do not have an noticeable influence in the fs scheme because of the broadband nature of the excitation pulses.

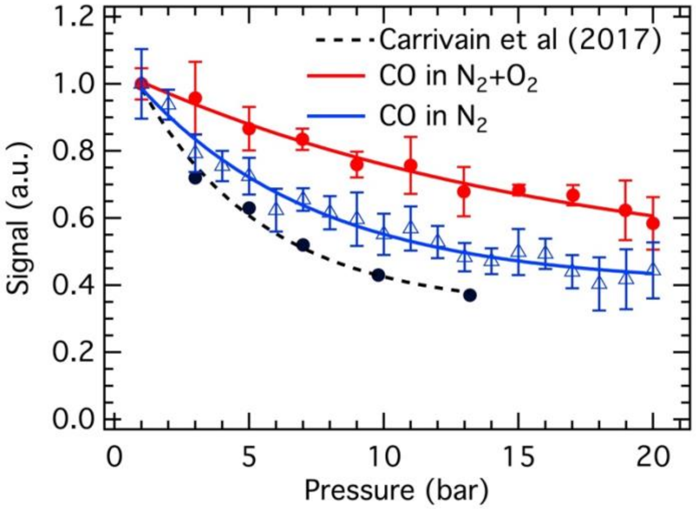

Figure 27. The normalized CO-TPLIF signal as a function of total pressure.

Then high-resolution spectra of the CO B→A (0, 0) and (0, 1) bands were also recorded in the mixture of 2.6% CO diluted in N_2/O_2 using a 2400 lines/mm grating. The spectrum shown here was an average of 500 frames with each frame containing on-chip accumulation of 300 laser shots. As shown in Figure 28, it clearly shows ro-vibrational structures of both bands at 0.1 and 1 bar. However, as pressure increases, the individual rotational lines broaden and become indistinguishable due to the increased pressure broadening. Additionally, compared to the spectra at lower pressures, the vibrational structures become noisier at higher pressures because of reduced signal levels. It also shows that the spectra broaden towards longer wavelengths, which is different from the observation from Carrivain et al. [144]. These broadening behavior is observed because of the high-resolution grating used in this work.

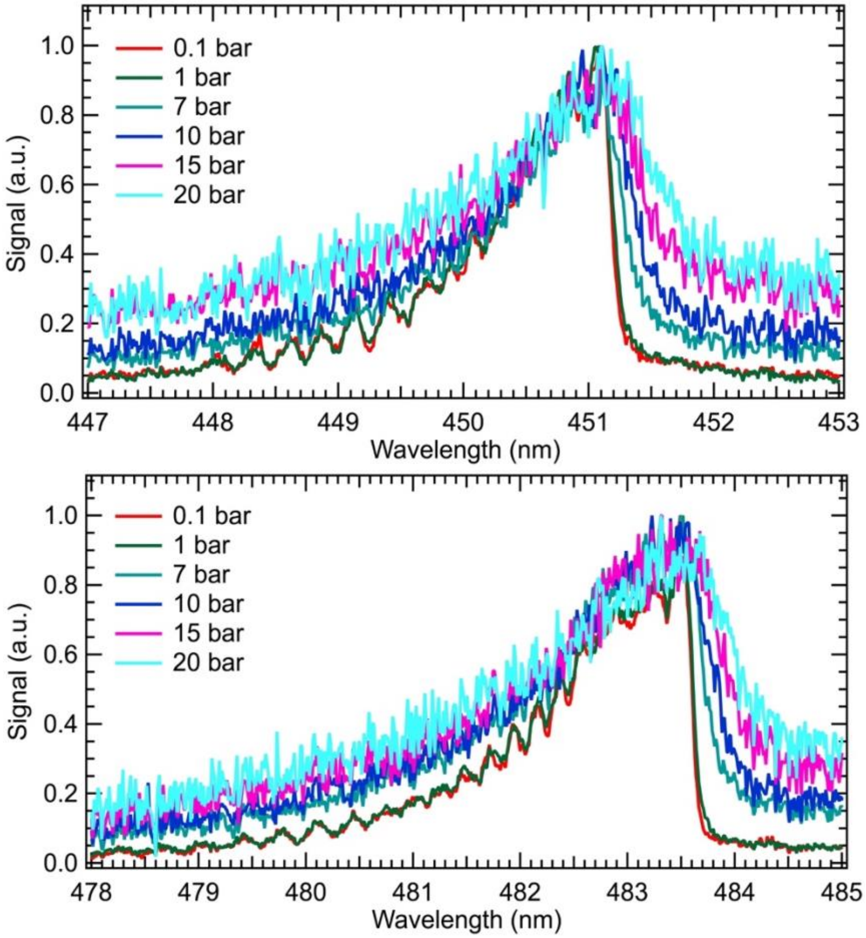

Figure 28. High-resolution spectra of the CO B→A (0, 0) and (0, 1) bands at various cell pressures.

The collisional quenching is also highly dependent on colliding species besides the pressure. The variation of CO-TPLIF signal as a function of total pressure in N_2 and He with various fixed CO number densities is shown in Figure 29. For this purpose, pure CO with different initial pressures was injected into the gas cell, then the partial pressure of N_2 and He gas was gradually increased until the total pressure reached 20 bar. Integrated

CO signals were normalized with respect to the peak signal of each initial pressure condition. As can be seen in Figure 29, all of the normalized signals decrease with the increase of total pressure. Furthermore, the decay rate of the normalized signal in the mixture of N_2/CO is always faster than that in He/CO mixture. As such, for the initial CO pressure of 0.05 bar, the signal decreases by 90% for the N_2/CO mixture when the total pressure rises up to 10 bar; while it drops by 50% for the He/CO mixture at the same pressure. is the total signal remains at 65% level even at 20 bar. Settersten et al. [78] measured the cross sections for collisional quenching of CO by various gases and reported 24.46 and 0.25 Å^2 for N_2 and He at room temperature respectively. Clearly, N_2 is a stronger quenching species and He is a weaker quenching species. Additionally, at a fixed pressure, the fluorescence signal increases with increasing initial CO pressure for both N_2/CO and He/CO mixtures, indicating that the self-quenching of CO has little influence when CO concentration is sufficiently low.

Then we also investigated the CO fluorescence signal as a function of total pressure with a fixed CO mole fraction in mixtures of N_2/CO and He/CO. As shown in Figure 30, except for 1% and 5% CO diluted in He mixtures, similar trends are observed. The normalized CO fluorescence signal decreases as pressure increases for all N_2/CO and He/CO mixtures. Compared to the mixtures of fixed CO number densities, the normalized signal decreases with increasing mole fraction of CO at a fixed pressure, indicating that the self-quenching of CO has a significant influence on CO fluorescence signal loss. For example, the normalized signal drops by 90% when the mole fraction of CO is 50% in He, although He is the weakest quenching species.

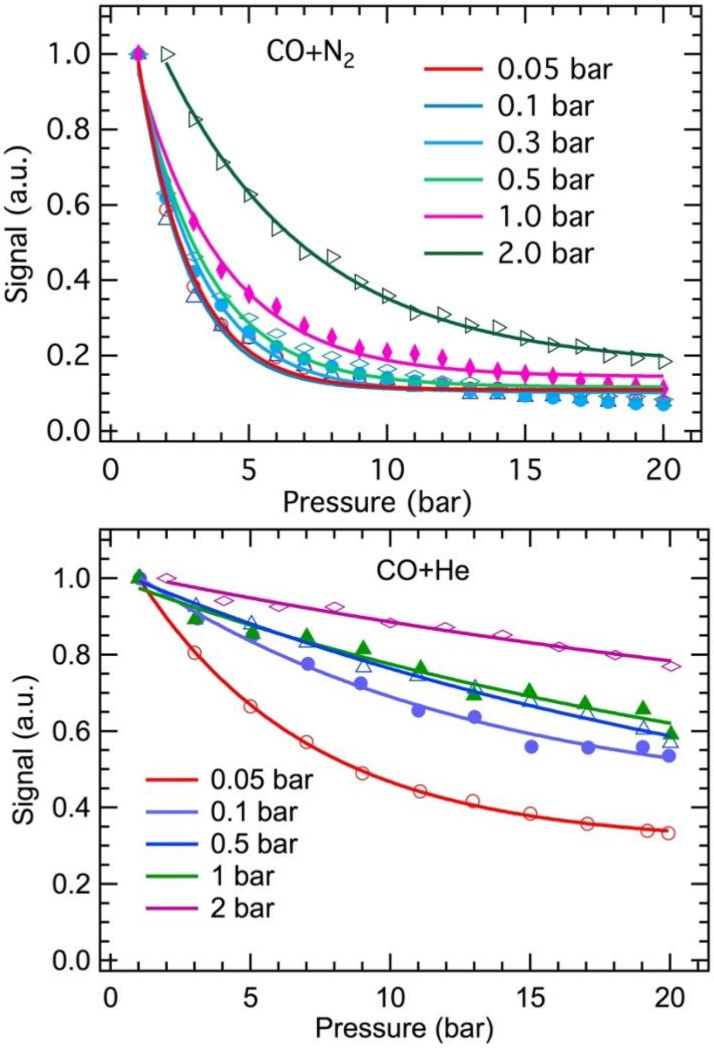

Figure 29. Dependence of CO-TPLIF signal as a function of total pressure in N$_2$ and He with various pressure with fixed CO number densities.

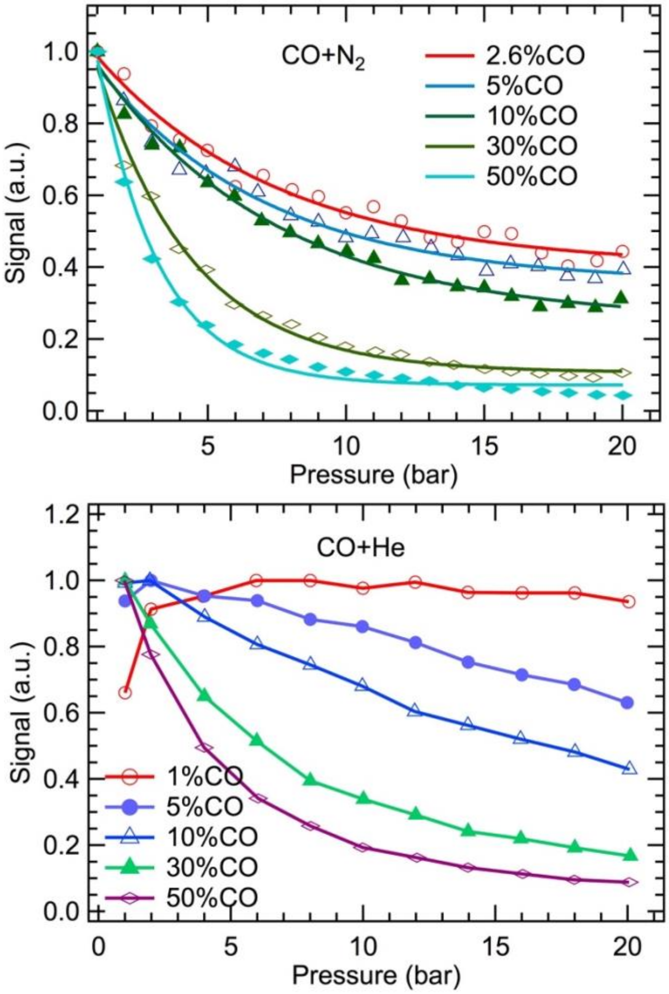

Figure 30. Dependence of CO-TPLIF signal as a function of total cell pressure in N$_2$ and He with various pressure at fixed CO mole fraction.

4.3.3. CO fs-TPLIF Application in Gaseous Sooting Flames

For the CO $B^1\Sigma^+ \leftarrow X^1\Sigma^+$ two-photon transition scheme, the fluorescence signal is expected to be proportional to the square of the laser energy below the saturation regime. However, being a nonlinear loss mechanism of the excited state population, photoionization and stimulated emission interferences in practical sooting flames can both result in sub-quadratic energy dependence of the fluorescence signal. The observed fs-

TPLIF of CO signal as a function of the laser pulse energy in a sooting C_2H_4-air flame of Φ =1.5 is plotted on a log-log scale in Figure 31. Because the spectral lines of CO at 451 nm and 483 nm isolate from C_2 interferences, we only collected the CO fluorescence signal in the 450±5 nm spectral range. The fluorescence signal plotted here was an average of 200 camera frames with each frame containing on-chip accumulation of 100 laser shots. Each data point was repeated three times and the average value is plotted. From these results, it can be seen that the fluorescence signal exhibits a power dependence I^m where the exponent m=1.45 at lower laser energies, and m=1.14 at higher laser energies. These results are in agreement with previously reported power dependence measurements in the literature [17, 22, 72]. At low CO concentrations, sufficient laser energies are required to generate fluorescence signals with a reasonable signal-to-noise ratio. However, at high laser energies, the ionization and stimulated emission processes become significant and can further reduce the expected quadratic power dependence for this two-photon excitation scheme [22].

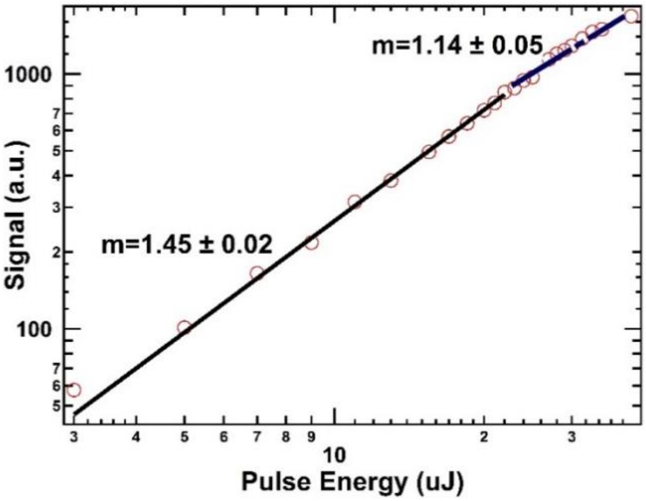

Figure 31. Laser pulse energy dependence of fs-TPLIF of CO signal in a premixed C_2H_4-air sooting flame with Φ =1.5.

After the characterization described in the above experiments, the fs-TPLIF scheme was then used to measure the CO signal level in a wide range of CH_4/air and C_2H_4/air sooting flames that were stabilized over a Hencken calibration burner. For all these measurements, a 10-ns ICCD gate width was used along with the bandpass filter described above. The adiabatic flame conditions achievable in the Hencken burner allows direct comparison of the measured CO number density profile with the calculated equilibrium CO number densities. As shown in Figure 32, the CO fluorescence signal keeps constant at the height of 5—15 mm. Thus, the laser beam was set approximately 10 mm above the burner surface, all the experimental measurements were taken at this height. The laser pulse energy in the probe region was set at approximately 22 µJ/pulse.

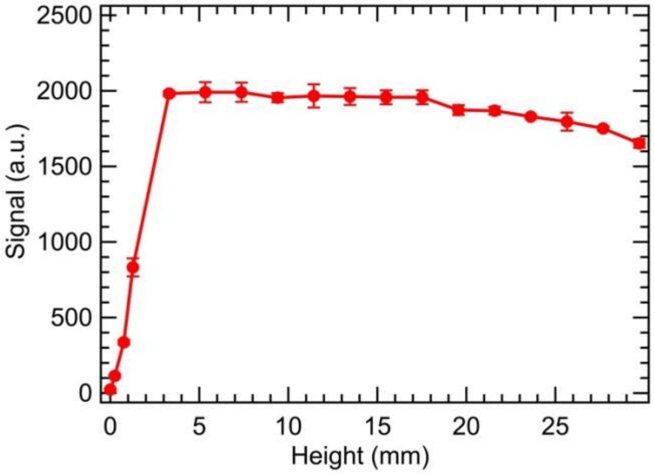

Figure 32. Dependence of the CO-TPLIF signal on height above the burner surface in a premixed C_2H_4-air sooting flame of Φ =1.5.

Figure 33 and Figure 34 show the CO-TPLIF emission spectra at various equivalence ratios in CH_4/air and C_2H_4/air sooting and non-sooting flames. It can be seen clearly that C_2 interferences become prominent with increasing equivalence ratio, even the isolated CO peaks around 451 and 483 nm are affected to some degree by neighboring strong C_2 emission bands despite time gating the signal using a 10-ns ICCD gate. Spectrally integrating the fluorescence signal only in the 445–455 nm region is the best possible solution to minimized C_2 interferences based on our current studies.

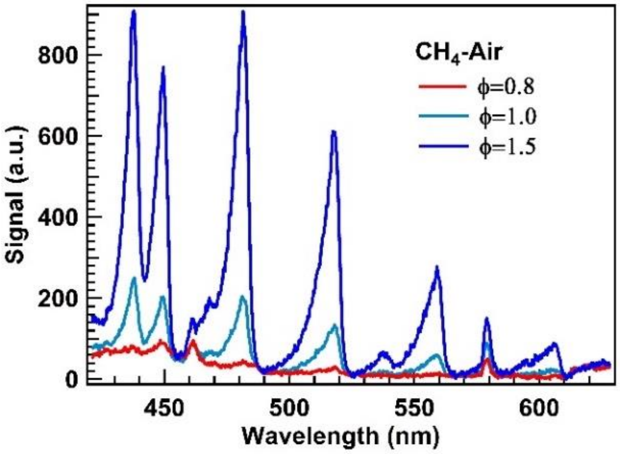

Figure 33. CO-TPLIF emission spectra recorded at various equivalence ratios in sooting flames with premixed CH_4/air flames.

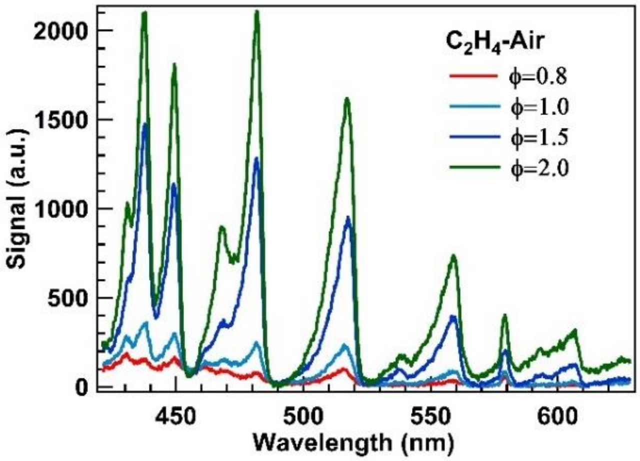

Figure 34. CO-TPLIF emission spectra recorded at various equivalence ratios in sooting flames of premixed C_2H_4/air.

The corresponding fs-TPLIF signal of CO as a function of flame equivalence ratio in CH_4/air and C_2H_4/air sooting flames is shown in Figure 35 and Figure 36. As discussed above, we used a 10-ns detection gate and only collected the CO fluorescence signal near 451 nm using the bandpass filter to minimize the contributions from C_2 interferences. The equilibrium CO number densities were calculated using the STANJAN chemical equilibrium code and compared with the experimental CO fs-TPLIF profiles. It can be seen that the measured CO fluorescence signals show a good agreement with the calculated CO concentrations for both premixed CH_4/air and C_2H_4/air flames over a wide range of equivalence ratios. The experimentally observed CO concentrations are slightly lower than the equilibrium calculations at higher equivalence ratios or fuel-rich flames. Note that no quenching or photolytic interference (photodissociation of CO_2 and CO) corrections were applied for measured the CO-TPLIF signals in these results. These observations suggest that the fs-TPLIF excitation scheme can provide significant advantages in quantitative detection and imaging measurement of CO radicals in sooting flames. A signal correction may be applied using respective quenching cross section, provided the flame temperature and major collision partner concentrations.

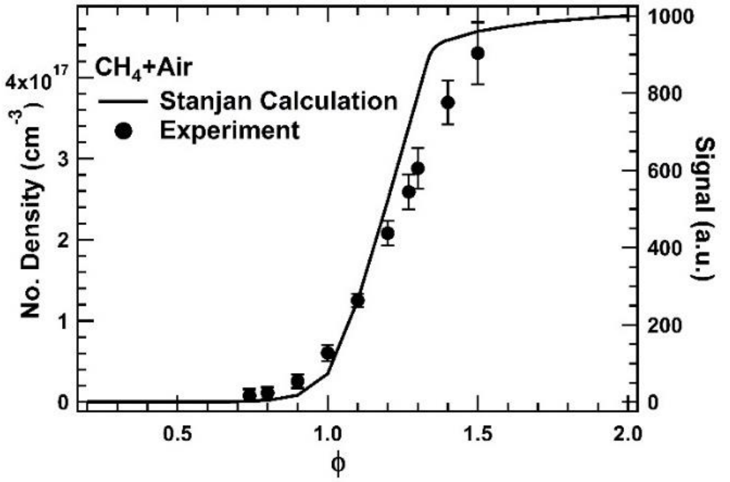

Figure 35. Fs-TPLIF signal of CO as a function of flame equivalence ratio in a premixed CH_4/air sooting flame. Solid line represents the calculated equilibrium CO number density using STANJAN.

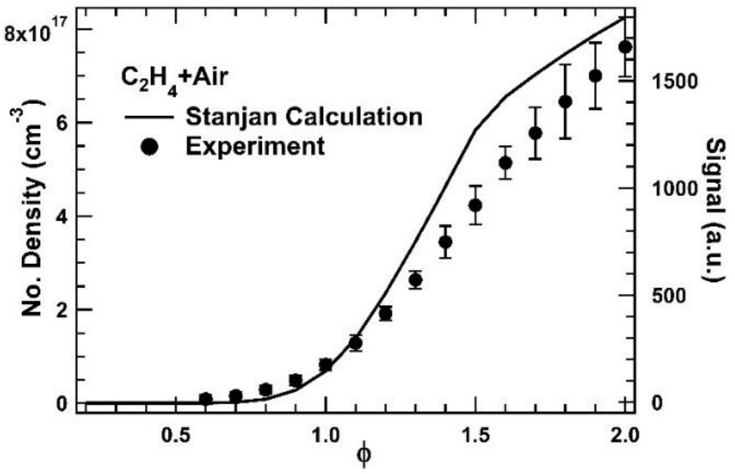

Figure 36. Fs-TPLIF signal of CO as a function of flame equivalence ratio in a premixed C_2H_4/air sooting flame. Solid line represents the calculated equilibrium CO number density using STANJAN.

To illustrate the planar TPLIF imaging of CO in premixed sooting flames, the Hencken calibration burner was replaced with a premixed Bunsen-type jet flame. A +100-mm-focal-length plano-convex lens coupled with a plano-concave cylindrical lens (f=-150 mm) was used to generate a laser sheet with an effective height of about 5 mm. A 50-mm-focal-length f/1.2 camera lens along with a 36-mm extension lens tube was used to collect the fluorescence signal and focus it onto the ICCD camera. As discussed above, a broadband detection filter and gate width would increase C_2 interference for CO imaging measurements in sooting flames [18]. Hence, the 450-nm bandpass filter described above was mounted at the back end of the camera lens inside the lens extension tube. All images were acquired with a 10-ns detection gate width. The total laser energy used for the imaging measurement was ~25 µJ/pulse at the probe region. Sample fs-TPLIF images of CO in stable $C_2H_4/O_2/N_2$ jet flames at Φ=1.0, 1.5 and 2.0 are shown in Figure 37. The images in the top panel were acquired by a SLR camera at three different equivalence ratios, The PLIF images were generated by stacking a total of 60 images, each image containing on-chip accumulation of 200 laser shots. The burner was scanned vertically in steps of 0.5 mm between each image frame. As seen from the bottom panel of Figure 37, the CO-LIF signal exhibits a steep gradient in the transition between the cold reactants zone in the middle through the conical flame front, and gradually decays when moved radially outwards into the product zone and decays to near zero when entrained with the surrounding air. This behavior can be observed more clearly in Figure 38, where the radial CO line profiles generated 10 mm above the nozzle exit are plotted. The corresponding vertical location is also indicated by the white lines in the CO images in Figure 37. As seen in Figure 38 the peak CO-TPLIF signals increase with increasing equivalence ratio.

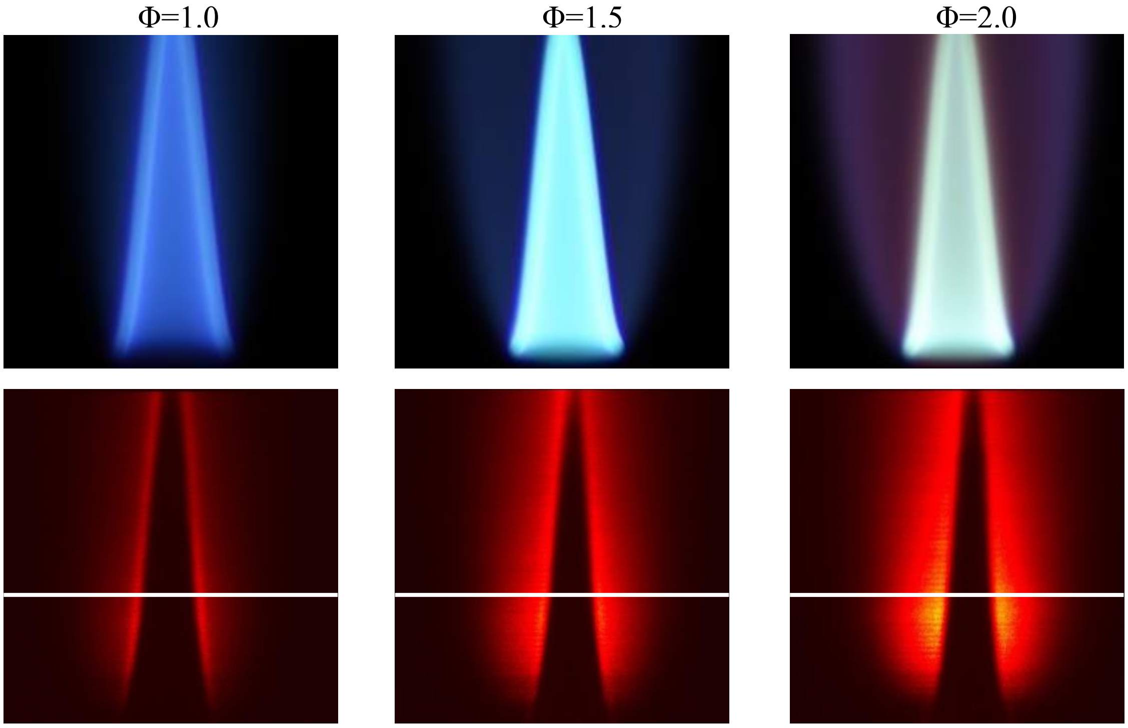

Figure 37. Fs-TPLIF images of CO recorded at three different equivalence ratios in $C_2H_4/O_2/N_2$ jet sooting flames.

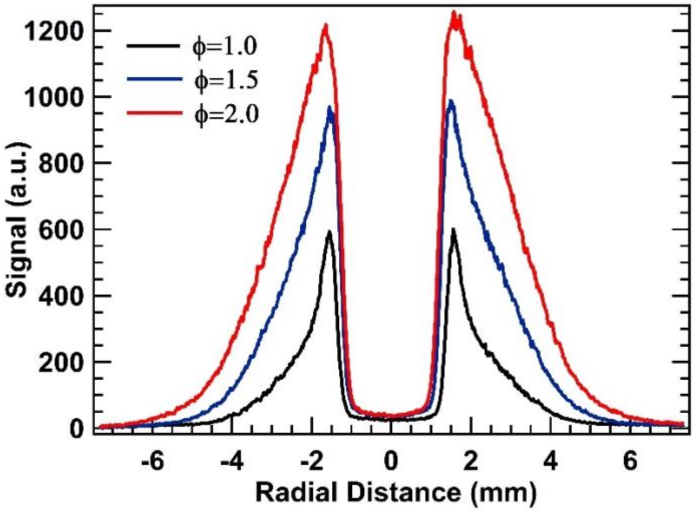

Figure 38. Fs-TPLIF line profiles of CO at varying equivalence ratios in $C_2H_4/O_2/N_2$ jet sooting flames at 10 mm above the nozzle exit (the white lines shown in Figure 30).

The potential for the high-repetition-rate (i.e., 1-kHz), single-laser-shot CO detection was investigated by replacing the ICCD camera by a high-speed CMOS camera coupled with a high-speed intensifier. Single-shot line images could be recorded using a 10-ns intensifier gate while incorporating the same spectral filter as described above. Figure 39 shows total integrated LIF signals from 1000 consecutive single-shot images recorded at 1-kHz repetition rate in a Φ=1.2 premixed $C_2H_4/O_2/N_2$ jet flame. It is seen that the shot-to-shot signal level fluctuations increases up to ~10% of the averaged signal level even in the stabilized sooting flames. We believe this fluctuation to result from a combination of minor flame instability, shot-to-shot laser fluctuations and detection noise. It is important to consider such fluctuations when investigating temporally-resolved CO measurements in turbulent sooting flames. The primary constraint for single-laser-shot 2D imaging in the current experimental setup is the limited laser energy available near 230 nm, thereby reducing the height of an excitation laser sheet only to a few millimeters. Also, the spectral filtering scheme implemented here limits the amount of CO fluorescence detected. However, such tight spectral filtering is essential for quantitative CO measurements in sooting flames as evident from the results of the present study.

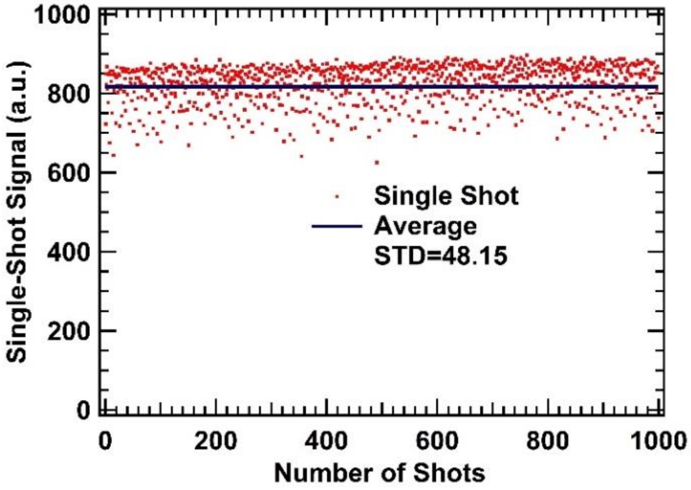

Figure 39. Consecutive single-laser-shot signal distribution recorded at a pulse repetition rate of 1 kHz in a Φ=1.2 premixed $C_2H_4/O_2/N_2$ jet flame. Height of the laser line is 10 mm above the nozzle exit.

4.3.4. CO fs-TPLIF Application in Liquid-Fuel Spray Flames

The additional phase change results in the overall combustion processes being more complicated and hence less well understood as compared to gaseous fuels. After investigating fs-TPLIF of CO measurements in gaseous hydrocarbon fuels, we then extended the fs-TPLIF technique to demonstrate CO measurements and investigate possible interferences in liquid-fuel spray flames. For the primary study on liquid-fuel spray flames, we used the liquid methanol (CH_3OH) with a simple chemical structure to make the demonstration less complicated. First, the chemiluminescence images were captured to characterize general structures of spray flames. The chemiluminescence of

OH* and CH* is natural emission of radiation from flames when chemically generated, energized OH and CH radicals return to their lower energy states. Previous studies have shown that the intensities of OH* and CH* chemiluminescence can act as a flame marker to locate the reaction zone and flame front location, respectively [145, 146]. Therefore, OH* and CH* chemiluminescence images were recorded to investigate the overall structures of these piloted liquid-spray flames. Figure 40 shows the averaged chemiluminescence images of OH* and CH*. It can be seen that the OH* and CH* chemiluminescence signals peak in the middle part of the spray flames, indicating that the reaction and heat release mainly occur in this region. Because these signals are the line-of-sight path averaged, no further information on flame structure can be derived from them.

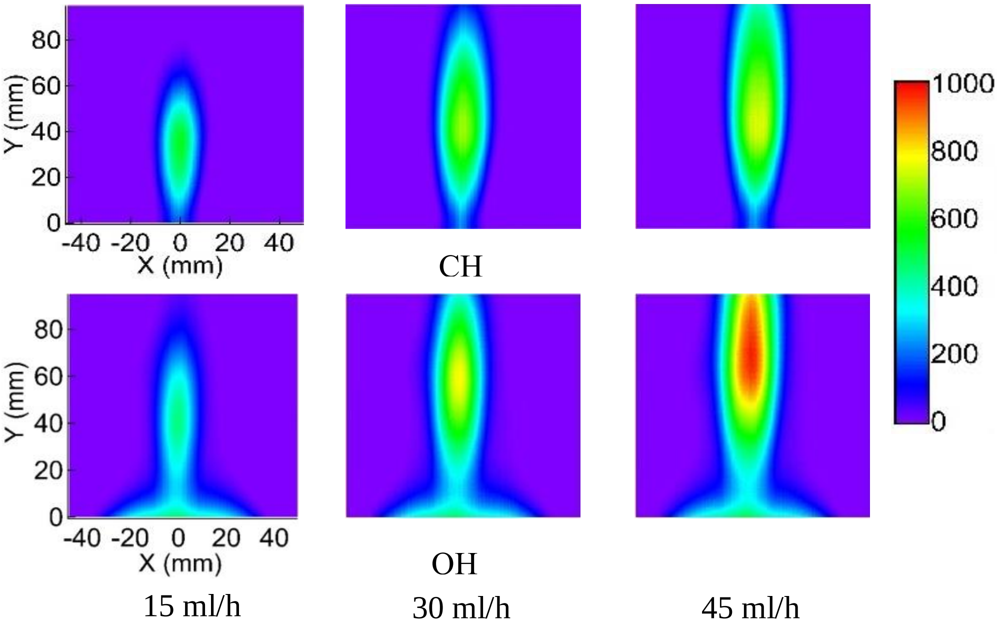

Figure 40. Averaged chemiluminescence images of OH* and CH* in three different liquid-spray flames.

Then we recorded OH-PLIF images in these liquid-spray flames to understand the structures of spray flames in detail. Single-laser-shot OH-PLIF images were recorded in a liquid spray flame at 30 ml/h of liquid methanol. As shown in Figure 41, the OH-LIF signal is zero in the central region because of the dense liquid droplets, then increases at the flame front where the fuel entrained and react with the surrounding air, and then decays to zero in the surrounding environment. Moreover, the variation of the OH-PLIF image structures shows the presence of strong turbulent mixing processes in these spray flames. Subsequently, images of 100 single-laser-shot averaged OH-PLIF images were recorded at each height. The measured OH-PLIF signals along the axial direction were combined to map the overall OH-PLIF profile distribution. Figure 42 shows the overall OH-PLIF images at different flow rates in spray flames. In this figure, the dark regions in the middle (i.e., those with low OH-signal levels) represent the dispersion and evaporation of liquid methanol. These images clearly show that the primary reaction mainly occurs around the periphery of the liquid core near the nozzle exit region. At higher location, the reaction zone spreads more uniformly since the liquid droplets are now fully evaporated and behaved as a gaseous fuel. Moreover, with increasing flow rates of liquid methanol, the core region becomes longer corresponding to the longer residence time of liquid droplets.

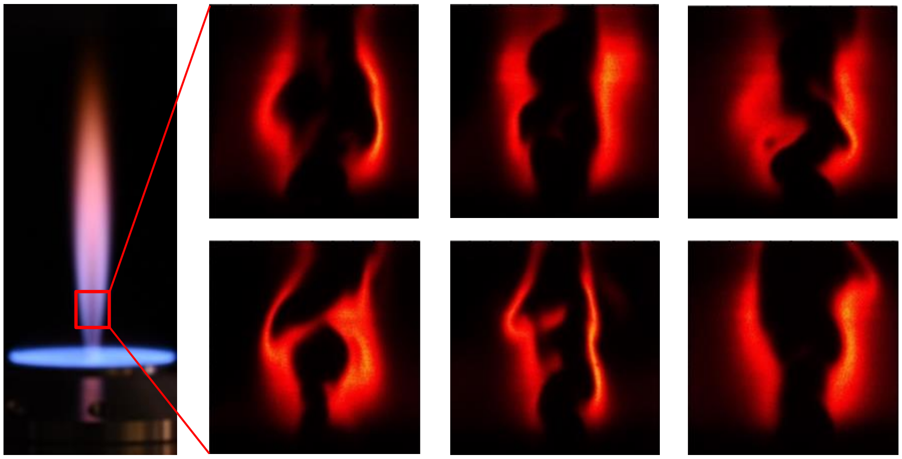

Figure 41. Samples single-laser-shot OH-PLIF images recorded in a piloted-liquid spray flame of 30 ml/h of liquid methanol. Each frame corresponds to an area of 20 mm×20 mm.

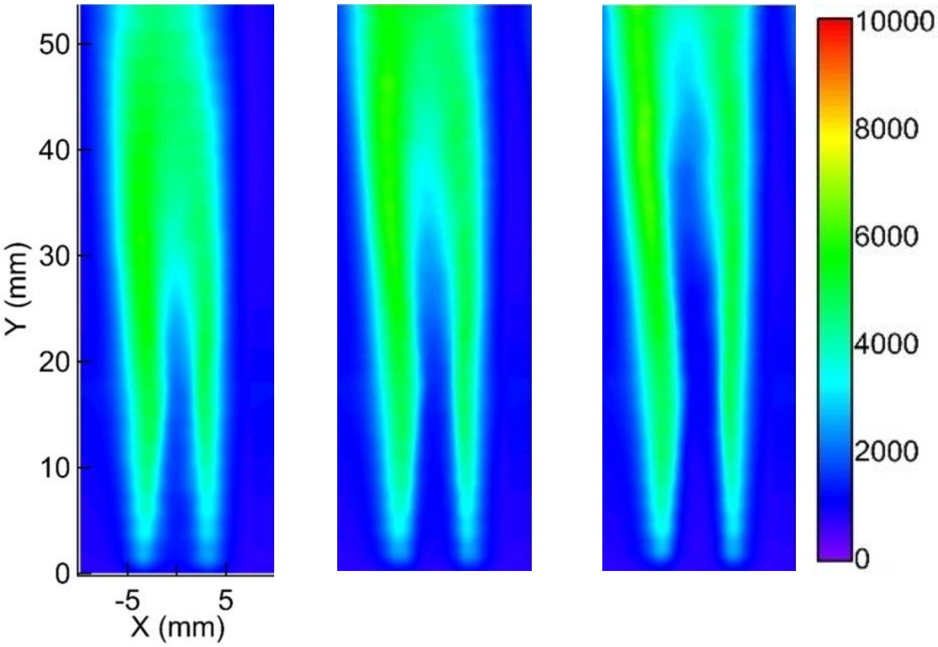

Flame 1
(15 ml/h)

Flame 2
(30 ml/h)

Flame 3
(45 ml/h)

Figure 42. OH-PLIF images at three different flow rates in liquid-spray flames.

After gaining sufficient understanding of the flame structure, fs CO-TPLIF studies were performed. Besides known C_2 Swan-band interferences as in gaseous sooting flames, other possible interferences from liquid droplet region were also investigated. Figure 43 shows fluorescence emission spectra detected for the three spray flames at various height-above-burner (HAB) locations. It can be seen in Figure 43 (a) & (b) that near the nozzle exit region, the spectral line near 460 nm is order of magnitude stronger than other CO emission lines. As seen in Figure 43 (c)–(f), the intensity of this peak gradually decreases and become negligible at increasing HAB locations, indicating this interference may result from the liquid core region of the spray. Because the unevaporated, dense droplet clusters exist close to the nozzle exit, the 230.1-nm excitation laser gets second-order expansion, and results in a strong 460-nm emission line. At further downstream HAB locations, liquid droplets are gradually evaporating and the second-order laser interference becomes insignificant. Furthermore, the interferences from C_2 Swan bands always present in downstream locations for all spray flames as seen in Figure 43 (c)–(f). All these spectra were recorded using a short detection ICCD gate of 10 ns. Therefore, we conclude that short detection gates and carefully selected spectral filtering scheme [30] are necessary for avoiding interferences during CO fs-TPLIF in piloted methanol flames.

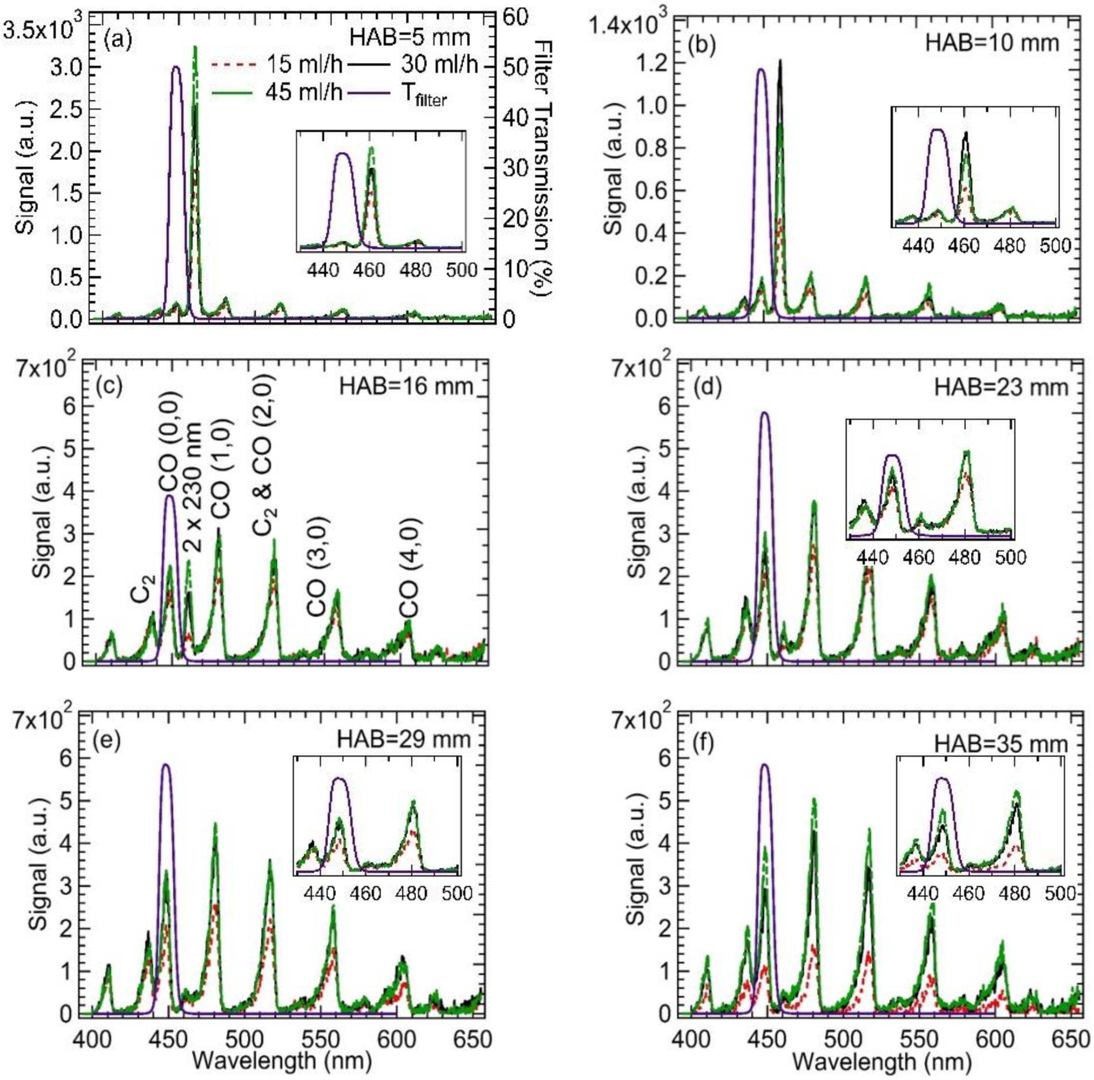

Figure 43. CO TPLIF spectra in spray flames as a function of height-above-burner (HAB). The transmission spectrum of the bandpass filter used for 2D CO imaging is represented by T_{filter}.

Therefore, during all subsequent CO imaging studies, a narrow detection gate (10 ns) and 450-nm band-pass filter were incorporated to minimize the interferences from C_2 Swan bands and nonlinear effects. CO TPLIF line images were recorded using laser pulse energy of approximately 10 µJ/pulse at the probe region. Figure 44 shows the axial CO distributions of the three spray flames. Each data point was repeated four times and the average value is plotted. It can be seen that the CO signal increases first and then decreases in the downstream of the spray flames as the fuel droplets gradually evaporate. After a certain height, the spray flame behaved similar to a gas-phase diffusion flame, then the CO concentration decays because of entrainment with surrounding air. Moreover, at a higher flow rates of liquid fuel, the droplet concentration increases everywhere of a spray flame needing longer residence times to fully vaporize and react. Hence, the axial CO distributions peak at different heights for these spray flames.

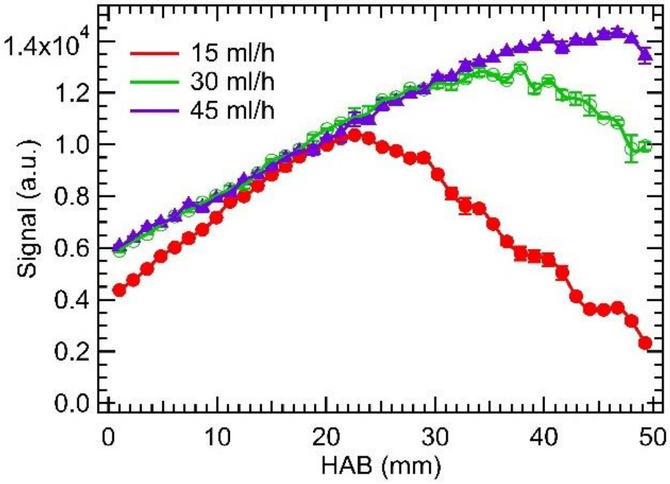

Figure 44. Axial CO distributions of the spray flames with three different flow rates.

Figure 45 shows the radial CO and OH profiles of the three spray flames at different HAB locations. As discussed above, near the nozzle exit, the droplet clouds present in the core region and the primary reaction takes place around the periphery of the liquid core. Hence the CO and OH intensities exhibit a dip in the center, form symmetric peaks around the flame front and decrease in radially outward locations due to entrainment of the ambient air. As the HAB gradually increases, outside air partially diffuses into the central core and hence the two CO peaks merge together. Interestingly, peak CO radial positions are closer to the central axis as compared to peak OH locations, indicating that CO is formed rapidly in the low-temperature, rich inner boundary region of the liquid core. This observation qualitatively agrees with the generally accepted behavior of partial oxidation in rich, low-temperature regions in hydrocarbon flames giving rise to CO, polyaromatic hydrocarbons (PAHs) and soot. In the future, we expect collaboration with a combustion modeling team to develop a 2D laminar flame model with full reaction chemistry to further explore this behavior well. Such efforts are beyond the scope of the present study and will be discussed in detail in a forthcoming publication.

To obtain 2D CO images in these spray flames, a f=-100-mm plano-concave cylindrical lens and f=+150-mm plane-convex spherical lens were used to generate a laser sheet with an effective height of approximately 2 mm. Full 2D CO profiles were obtained by vertically scanning burner height in steps 2 mm and are shown in Figure 46. The radial and axial CO profiles described in Figures 44 and 45 are well represented in these 2D CO images as well. It should be noted that the bright double peaks near the burner surface may still have some contribution from the leakage of the wings of the second-order interference of 230-nm excitation beam, resulting from the dense liquid regions.

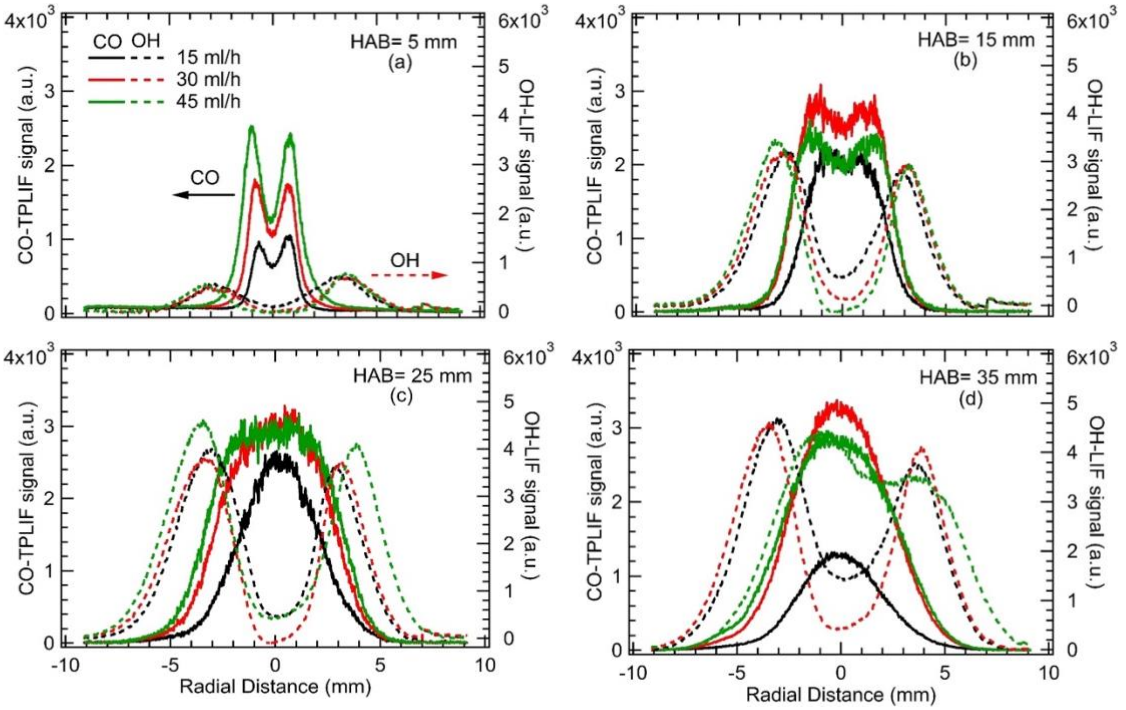

Figure 45. Radial CO and OH distributions of the spray flames at four different HAB locations. Solid lines represent CO profiles and dashed lines represent OH profiles.

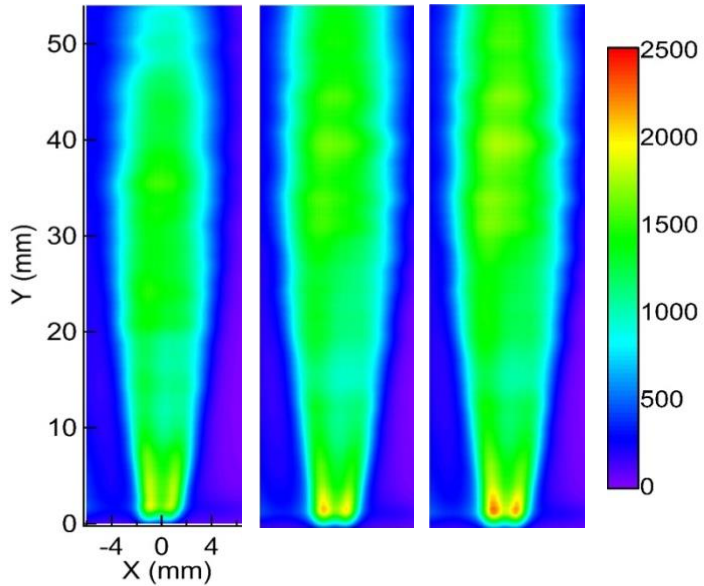

Flame 1
(15 ml/h)

Flame 2
(30 ml/h)

Flame 3
(45 ml/h)

Figure 46. Relative 2D CO images recorded using fs-TPLIF at three liquid-spray flames.

4.3.5. Two-line OH PLIF Thermometry in Liquid-Fuel Spray Flames

In order to further understand the structure and heat release, two-line OH PLIF thermometry was performed to obtain temperature profiles in these piloted liquid-spray flames. In this method, two separate spectral transitions $Q_1(5)$ and $Q_1(14)$ of the OH $A^2\Sigma^+$-$X^2\prod$ (0,0) band are excited. Because the characterization of the average flow fields is of primary importance in the current study, the two-line OH-PLIF imaging was recorded successively using a single laser system. In addition to the experimental simplicity, use of only one laser system mitigates uncertainties associated with the use of two laser and detection systems, which could have different laser bandwidths, laser energy fluctuations, detection efficiencies, and fields of view. It has been reported previously that the temperatures obtaining using sequentially-recorded images with a single laser system are comparable to those of simultaneous measurements with two different laser systems [116].

Shown in Figure 47 is the OH-excitation scan recorded by scanning the dye laser over the $Q_1(5)$ and $Q_1(14)$ lines in a piloted spray flame with 30 ml/h of liquid methanol. For both scans, the excitation pulse energy was 3 mJ, and the signal was averaged over 100 laser shots at each point. It shows that the normalized signals peak at $Q_1(5)$ and $Q_1(14)$ respectively, another weaker transition of $Q_{21}(5)$ is also observed. The line positions of excitation scans are in a good agreement with the predictions from the LIFBASE database.

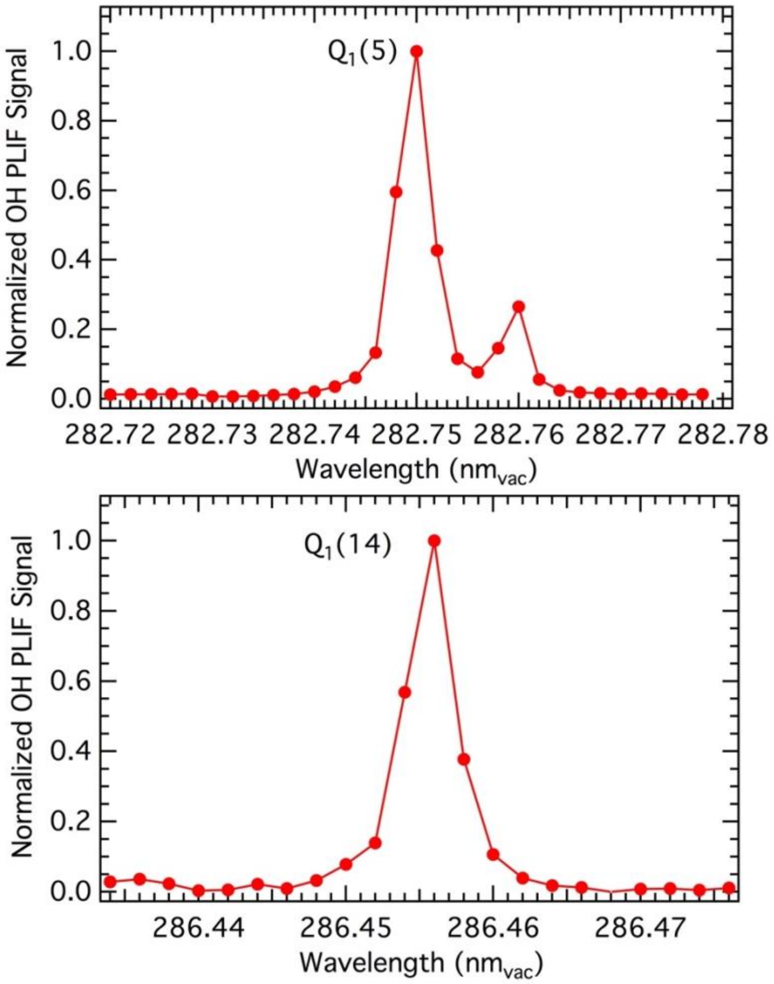

Figure 47. Excitation scan of $Q_1(5)$ and $Q_1(14)$ lines in a piloted liquid spray flame with 30 ml/h of liquid methanol.

Then the dependence of OH-PLIF signal on the excitation laser energy was investigated to ensure that the two-line OH-PLIF thermometry was conducted in the linear LIF regime. The UV excitation laser energy was adjusted by tuning the angle of frequency-doubling BBO crystal. As shown in Figure 48, the signal always scales linearly with the laser pulse energy in the range of laser energies investigated. Therefore, the laser energy was fixed around 6 mJ/pulse for both excitation lines during the following investigations.

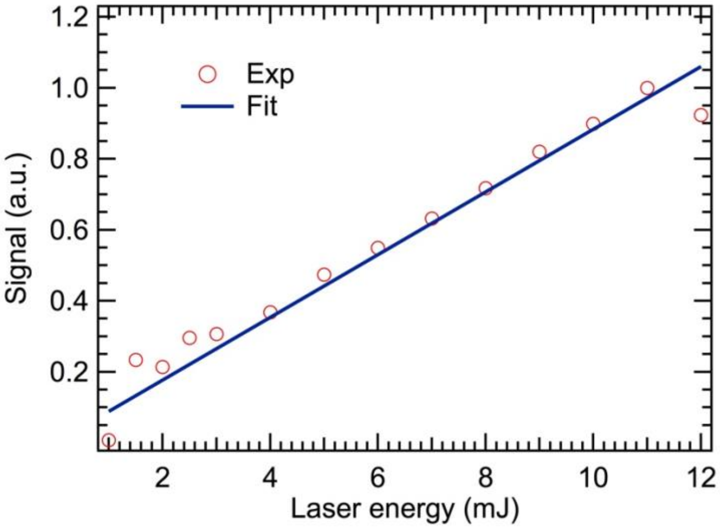

Figure 48. Dependence of the OH-PLIF signal on the excitation laser pulse energy.

Averaged OH-PLIF images of the $Q_1(5)$ and $Q_1(14)$ transition lines are shown in Figure 49 for three piloted spray flames. These images were averaged from 800 consecutive singlelaser shots to reduce fluctuations due to shot-to-shot laser energy and detection system fluctuations. Then, images with off-resonance were obtained to subtract background noises. Figure 49 also shows the dispersion and evaporation of liquid methanol (the dark regions in the middle), and the core region becomes longer corresponding to a longer residence time of liquid droplets as flow rates of liquid methanol increase.

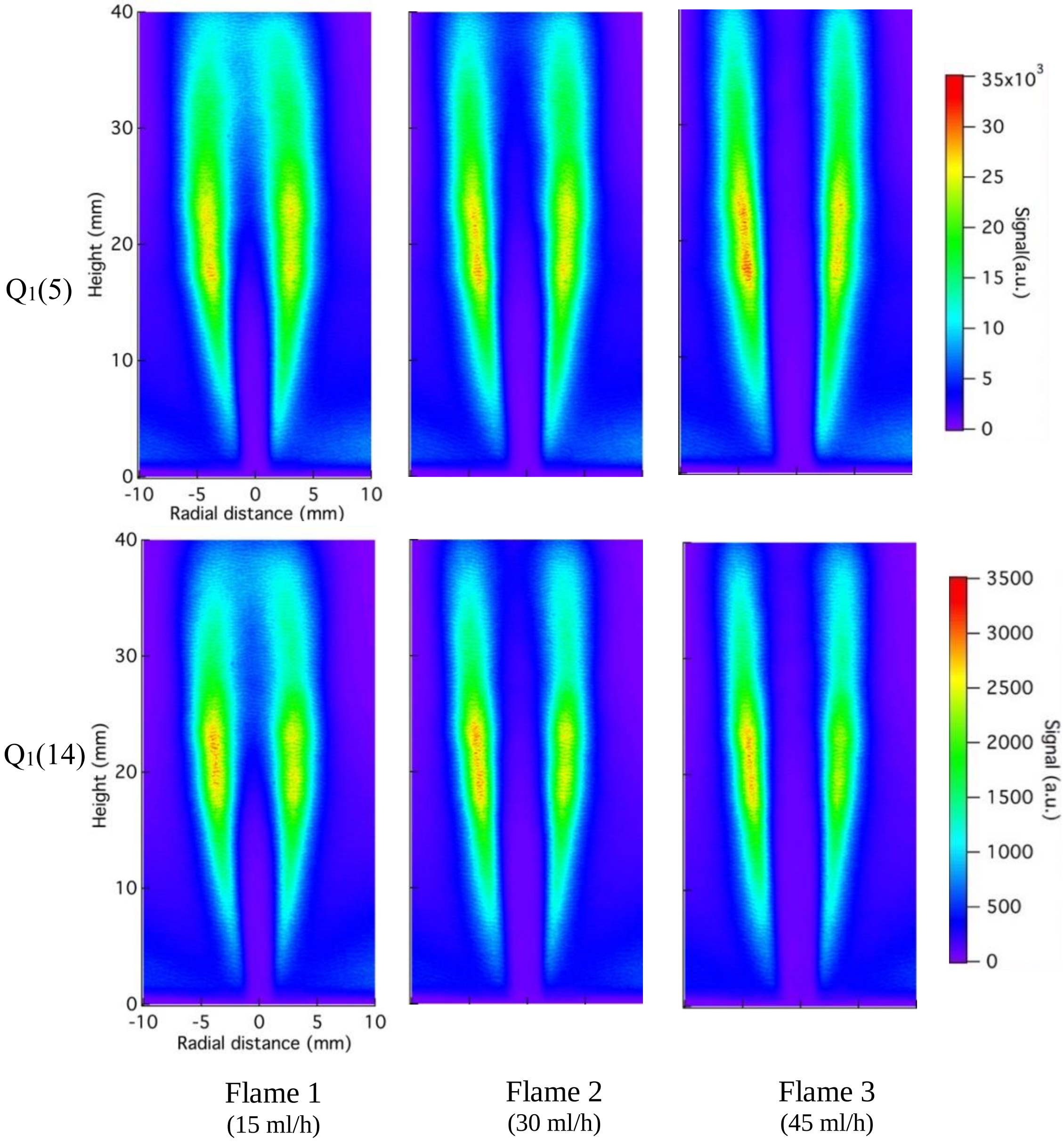

Figure 49. Average OH-PLIF images of the $Q_1(5)$ and $Q_1(14)$ transition lines in these piloted spray flames.

Then we recorded laser sheet energy profiles of the $Q_1(5)$ and $Q_1(14)$ transition lines. The UV laser sheets was striking on a 50-mm×50-mm UV image conversion plate and generating visible fluorescence. The induced visible fluorescence was then monitored using a beam-profile camera. Sample beam sheets of these two transition lines are shown in Figure 50. The intensity curves shown at the bottom were obtained from an average of 40 single sheet images. The OH-PLIF signal was then intensity calibrated by dividing by the beam sheet intensity at each pixel, and the resultant OH-PLIF images are shown in Figure 51.

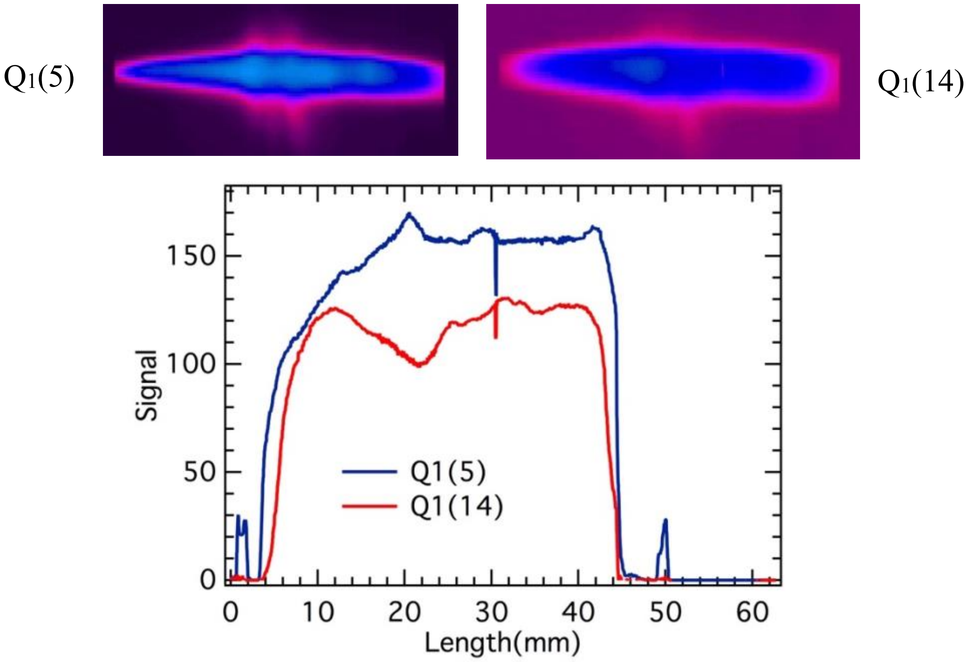

Figure 50. Excitation laser sheet intensity profiles of the $Q_1(5)$ and $Q_1(14)$ transition lines recorded using a beam profiling camera.

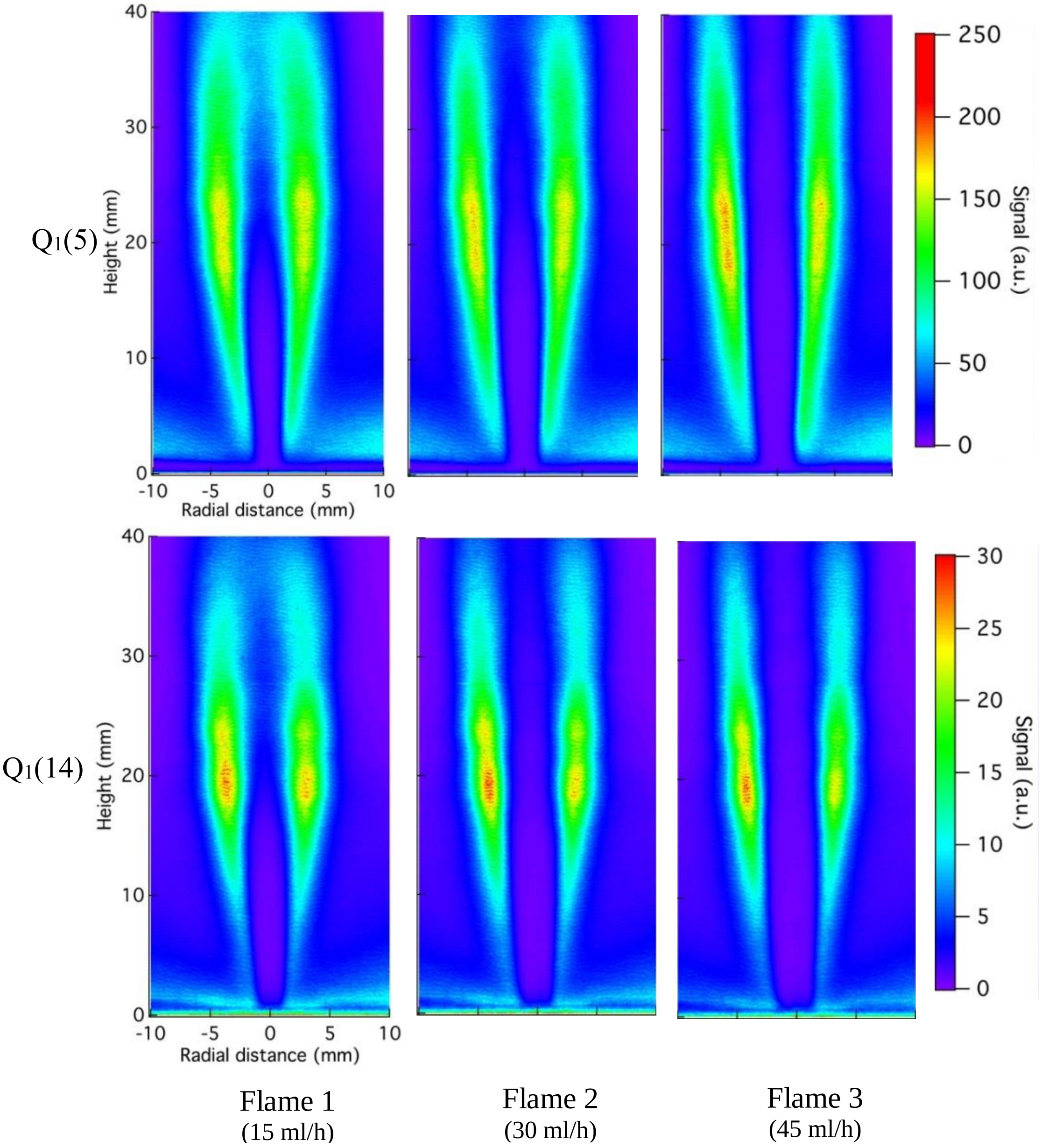

Figure 51. Intensity-calibrated OH-PLIF images of the $Q_1(5)$ and $Q_1(14)$ transition lines in the piloted liquid-spray flames.

The temperature was then determined by calculating the ratio of average OH-PLIF signal from the two $Q_1(5)$ and $Q_1(14)$ transition lines. LIFBASE software package was used for determining the mapping function from the fluorescence signal ratio to temperature. The relationship between the gas-phase temperature and the ratio of the two transition lines is shown in Figure 52.

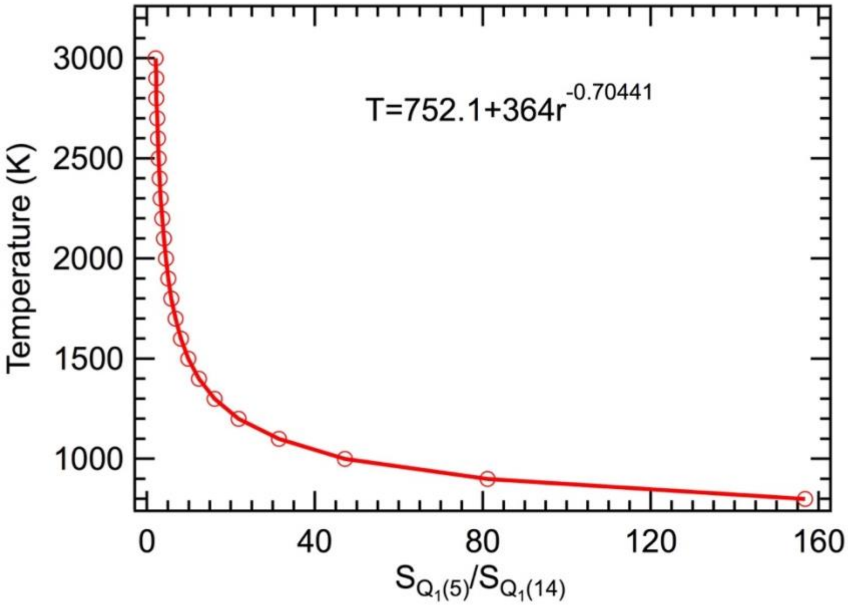

Figure 52. Simulated two-color OH PLIF temperature as a function of the fluorescence signal ratio (open symbols) and a power fit (solid line given by the equation).

The 2D temperature profiles are shown in Figure 53 in these liquid spray flames. It should be noted that the simulated temperature only works well for gaseous flame regions where sufficient OH-PLIF signals are present. In liquid spray flames, the majority of liquid particles are present in the core region of spray flames, then dispersed and evaporated along the propagation direction of the spray. In particular, close to the injector exit (or the surface of the McKenna burner), the unburnt liquid droplet density reaches the highest values. Hence, little or no OH-PLIF signal could be detected in these regions. In order to avoid significant fluctuations of the measured temperatures, a threshold was applied to the OH-PLIF images before calculating the signal ratio. Signals in the region below the threshold were forced to be 300 K and are colored blue in the temperature profiles. As shown in Figure 53, the temperature increases as the HAB gradually increases, and peaks at a height of ~20 mm. The peak temperature in the Flame 1 is higher than other two flames because more liquid particles are ejected with a higher flow rate of methanol. At the same height location, more heat is required to evaporate these particles and thus result in a lower peak temperature. Furthermore, the temperature decreases at radially outward locations due to entrainment of the ambient air. Overall, the temperature is in the range of 1000–2000 K at the height investigated in the current work. Other interferences in the two-line OH-PLIF thermometry technique, such as quenching, signal trapping, excitation efficiency, detection efficiency, and other sources of systematic errors are neglected in this study. These errors collectively can result in temperature errors up to 15% of the actual temperature [116, 118, 120, 123, 147].

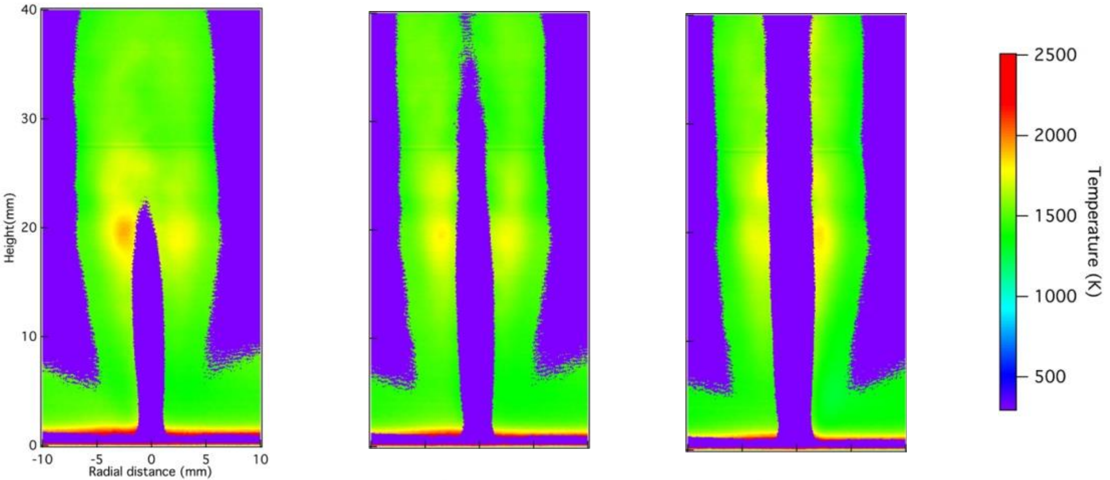

Flame 1
(15 ml/h)

Flame 2
(30 ml/h)

Flame 3
(45 ml/h)

Figure 53. Average temperature distributions of the three piloted spray flames obtained using the two-color OH PLIF method.

5. OH-PLIF IMAGING MEASUREMENTS IN FLAMES

5.1 Experimental Apparatus

A series of studies were conducted to investigate the potential of the fs-duration laser pulses for OH-PLIF imaging measurements in flames. As shown in Figure 54, laser radiation centered at 283 nm excites OH radicals from ground state ($X^2\prod$ (v''=0)) to excited state ($A^2\Sigma^+$ (v'=1)) via a single-photon transition, followed by fluorescence signal detection in the $A^2\Sigma^+ \rightarrow X^2\prod$ (0,0) and (1,1) bands. The experimental apparatus shown in Figure 55 consists of a regenerative-amplified Ti: Sapphire laser system, generating approximately 80-fs-duration laser pulses at 1-kHz repetition rate at the 800-nm wavelength. The fundamental output beam was used to pump an OPA for generating UV radiation for the excitation of the $A^2\Sigma^+ \leftarrow X^2\prod$ (1, 0) transition of OH near 283 nm. The UV beam was directed through several 45° dielectric laser mirrors and focused onto the probe region using a +200-mm-focal-length plano-convex lens. A thin, variable ND filter (Thorlabs, NDC-100C-4M) was placed before the plano-convex lens to adjust the laser pulse energy at the probe volume. A typical excitation spectrum of the fs-laser pulses is shown in Figure 56. With respect to the commonly used ns excitation of individual rotational lines such as $Q_1(5)$, $Q_1(7)$ and $Q_1(9)$, the broadband fs-laser pulses provide multiple excitation ro-vibrational transitions and thus significantly increase the excitation efficiency. For the fs OH-LIF spectroscopic studies, a series of flames stabilized over the Hencken calibration burner was used. The fluorescence signal was collected by a collimator placed orthogonal to the beam path, and was transmitted to the entrance slit of a spectrometer (Princeton Instruments, Model: IsoPlane 320) using a fiber optic cable. The spectrometer has 150, 1200 and 2400 lines/mm gratings to obtain low-, medium- and high-resolution spectra. The entrance slit width was set at 100 µm and the ICCD camera was fitted onto the entrance plane of the spectrometer to record fluorescence spectra. The detection gate width and gain of the ICCD camera were set to 30 ns and 100%, respectively. The spectrometer/ICCD camera system was wavelength calibrated using the same set of calibration lamps described above.

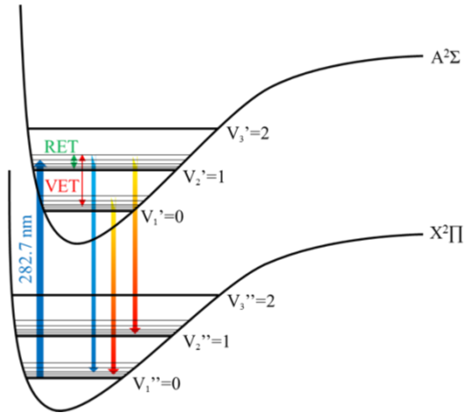

Figure 54. Energy level diagram for femtosecond single-photon-excited LIF of OH.

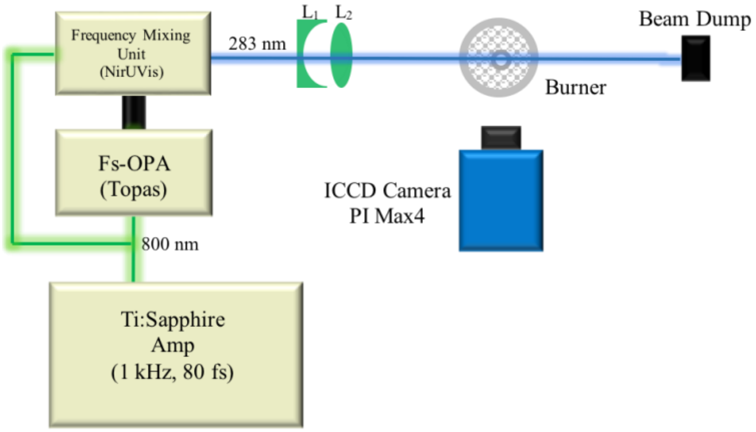

Figure 55. Schematic of the experimental apparatus for OH fs-LIF measurements.

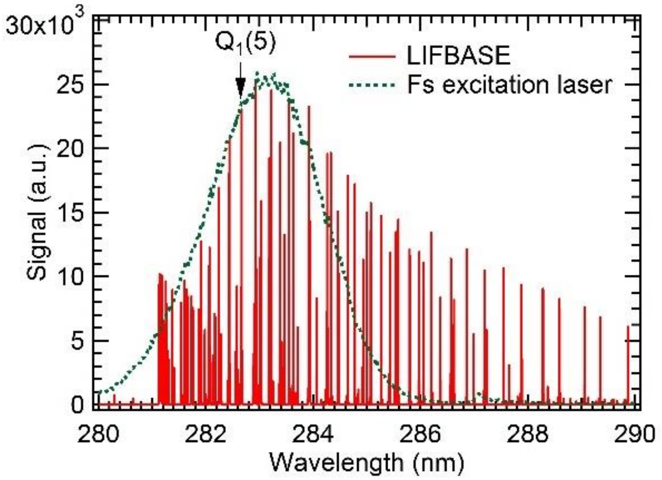

Figure 56. A typical spectrum of the broadband excitation laser having approximately 100-fs pulse duration overlaid with the calculated OH LIF spectrum using LIFBASE software package.

5.2 Results and Discussion

For OH spectroscopic studies, a range of flames stabilized over a 25.4-mm×25.4-mm Hencken calibration burner was used. The laser beam was fixed at the height of 10 mm above the burner surface. Shown in Figure 57 is the dependence of the OH fs-LIF signal on the excitation wavelength, obtained by recording spectra with different excitation wavelengths in a Φ=1.0 CH_4/air flame. For this case, the excitation pulse energy employed was fixed at 13 μJ/pulse, and the fluorescence signal was averaged over 30 frames with 600 laser shots accumulated in each frame. It is seen that the excitation wavelength centered at 283 nm results in the maximal LIF signal. The spectral bandwidth of this excitation wavelength is approximately 6 nm full-width at half maximum (FWHM); which is significantly broader than that of ns laser pulses [148].

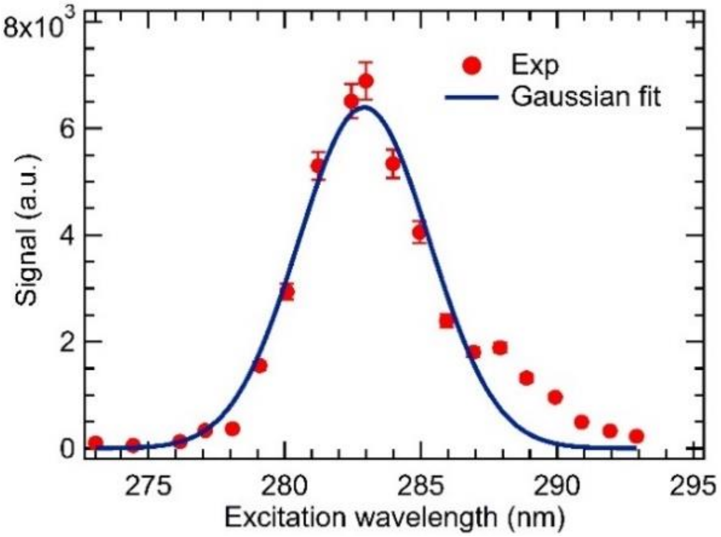

Figure 57. Dependence of the fs OH-LIF signal on the excitation wavelength.

Typical fluorescence emission spectra of the OH (1, 0), (0, 0) and (1, 1) bands followed by the excitation of the $A^2\Sigma^+ \leftarrow X^2\Pi$ (1, 0) transition in a stoichiometric CH_4/air flame are shown in Figure 58. The spectra were recorded with a 2400 lines/mm grating, then compared with simulated spectra using the LIFBASE program. The simulated spectra were obtained at 2200 K and 1 atm. A Gaussian profile was used to account for the collisional and Doppler broadenings. As seen in Figure 58, a detailed ro-vibrational fluorescence emission spectrum could be obtained using the broadband fs pulses. An excellent match is observed between the experimental and simulated spectra in the OH (1, 0), (0, 0) and (1, 1) bands. It should be noted that the simulated spectrum is rotationally thermalized (2200 K) but far from vibrationally thermalized states. Additionally, as shown in Figure 59, a temporal evolution of the two OH (1, 0) and (0, 0) fluorescence emission bands was recorded by scanning the ICCD gate delay while maintaining a 500-ps gate width. Hence, with temporally-, spatially- and spectrally-resolved fs-LIF emission spectrum, it is possible to obtain the variation of the effective collisional lifetime of excited OH transitions. It may also be possible to obtain vibrational and rotational energy transfer rates as well as collisional quenching effects using the fs-excitation schemes described here. As discussed above, collisional effects would result in the narrowband OH rotational transitions to broaden and shift at elevated pressures, resulting in reduced spectral overlap, thus decreasing the excitation efficiency. The broadband ultrashort pulses on the other hand, will result in minimal loss of spectral overlap and hence could be used for chemical species measurements at higher pressures.

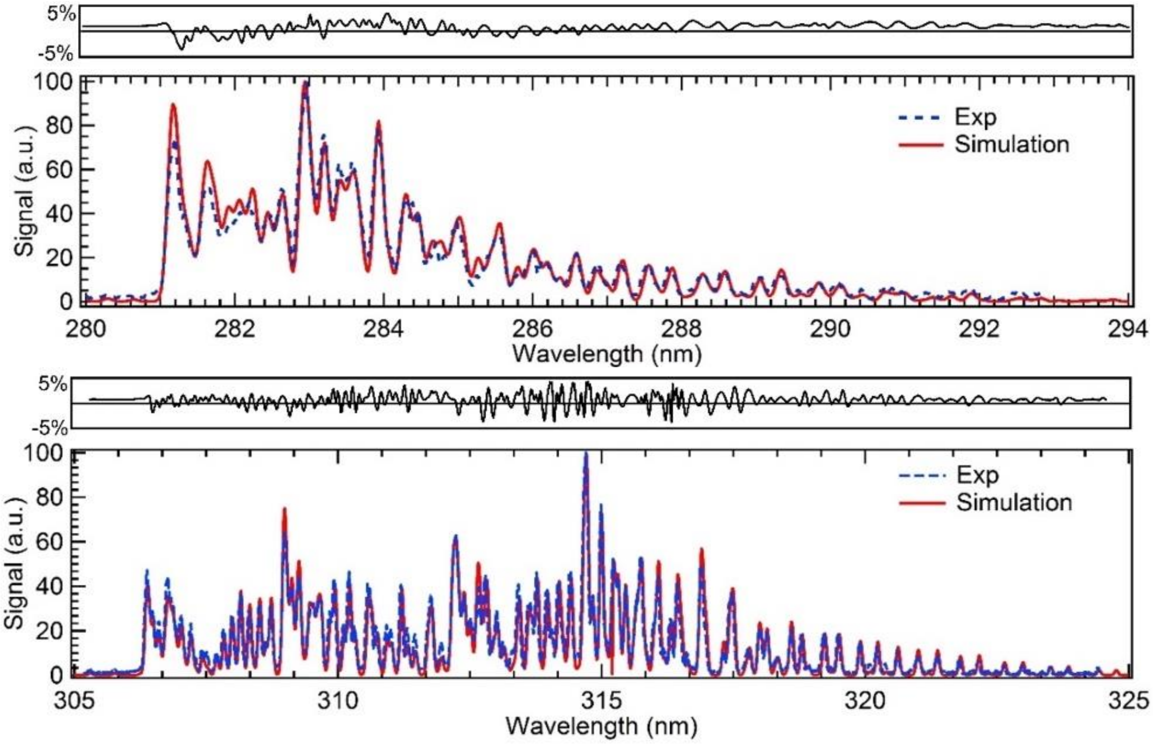

Figure 58. Comparison of fs-LIF emission spectra of the OH (1, 0) band (top) and OH (0, 0) & (1, 1) bands (bottom) in a stoichiometric CH_4/air flame with simulated spectra obtained using the LIFBASE software.

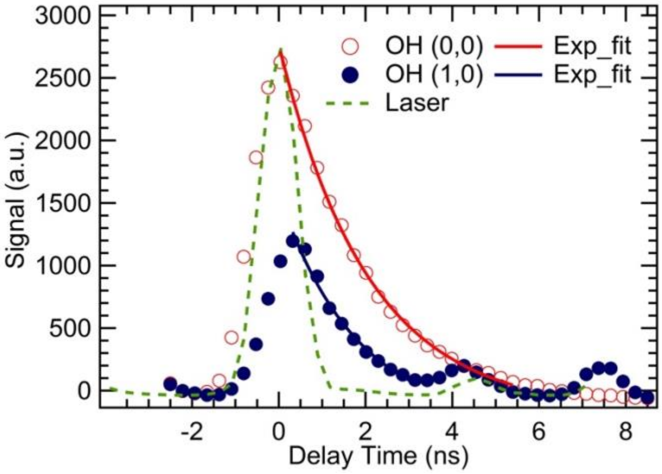

Figure 59. Temporal evolution of the two OH (1,0) and (0,0) fluorescence emission bands recorded in a stoichiometric CH_4/air flame.

The dependence of OH fs-LIF signal on laser pulse energy recorded in a Φ=1.0 CH_4/air flame is shown in Figure 60. We used a 1200 lines/mm grating to record the fluorescence emission spectra at different laser energies, and then integrated them in the range of 305–325 nm. As shown in Figure 60, the OH-LIF signal scales linearly with laser pulse energy below 15 µJ/pulse, while it deviates from linear behavior and gradually reaches saturation at higher laser pulse energies. Therefore, the laser pulse energy was fixed at 10 µJ/pulse to avoid saturation effects for all following experiments.

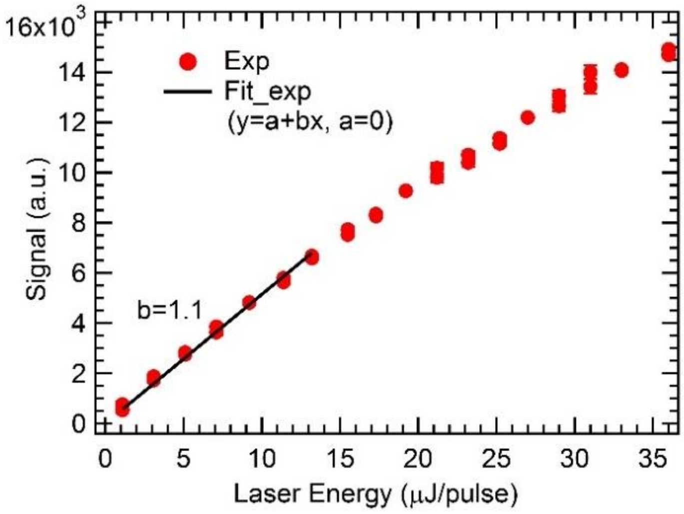

Figure 60. Laser pulse energy dependence of OH fs-LIF signal recorded in a stoichiometric CH_4/air flame. The estimated beam waist is approximately 80 μm.

To demonstrate the broadband, fs excitation scheme is a promising method for OH concentration measurements in flames, a 1200 lines/mm grating was used to record the fluorescence emission spectra in CH_4/air, C_2H_4/air and H_2/air flames from lean to rich conditions. Figure 61 shows the peak-normalized OH-LIF emission spectra of OH (0, 0) and (1, 1) bands in CH_4/air flames at different equivalence ratios. It is seen that the spectra are nearly identical in all equivalence ratios investigated, indicating that no evidence of additional spectral interferences are present, in particular in rich flames. Therefore, it suggests that the broadband, fs pulses could be used while collecting fluorescence emission signal through a commonly used broadband OH filter having transmission spectrum similar to the one shown in Figure 61. The signal magnitude at a given line position varies with the flame equivalence ratio. This observation can be explained by the variation of equilibrium flame temperature at different equivalence ratios, thereby resulting in varying OH concentrations in the flame zone.

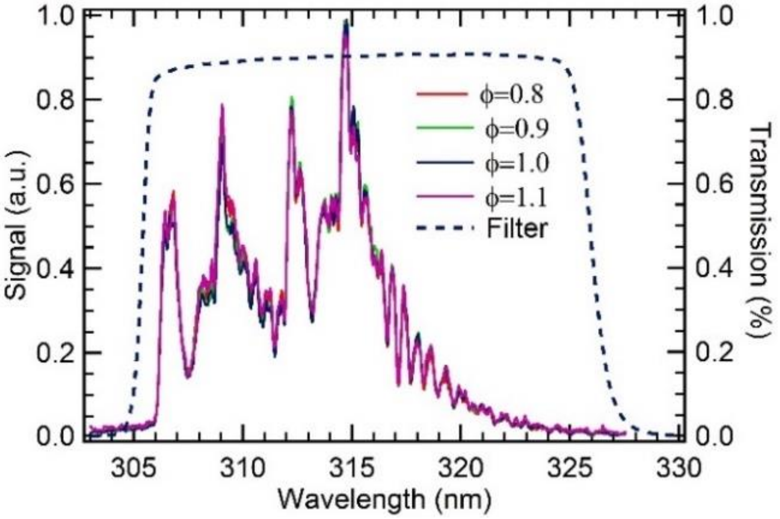

Figure 61. Peak-normalized OH-LIF emission spectra recorded at different equivalence ratios in the CH$_4$/air flame. The transmission window of the OH detection filter is also shown by the dotted line.

Subsequently, the fs-LIF scheme was used to measure OH concentrations in a range of CH$_4$/air, C$_2$H$_4$/air and H$_2$/air flames. To obtain stabilized flames, the total flow rates of CH$_4$/air and C$_2$H$_4$/air flames were maintained at 10 slm (standard liters per minute) to achieve the equivalence ratios varied between 0.7–1.5 and 0.5–1.5 respectively. For H$_2$/air flames, the air flow rate was fixed at 52 slm and the H$_2$ flow rate was varied between 15–35 slm to obtain the equivalence ratios in the range of Φ=0.7–1.6. The measured total OH-LIF signals in these flames are shown in Figure 62 as a function of flame equivalence ratio. The equilibrium number density shown was calculated using CANTERA and STANAN chemical equilibrium codes, and the temperature was obtained using the STANAN chemical equilibrium code. It is seen that a reasonable agreement was obtained between the measured and calculated OH profiles. The OH concentrations increase with increasing Φ and then decrease with a further increase in Φ for all these flames. The peak OH concentrations are observed slightly below the stoichiometric conditions for CH_4/air and C_2H_4/air

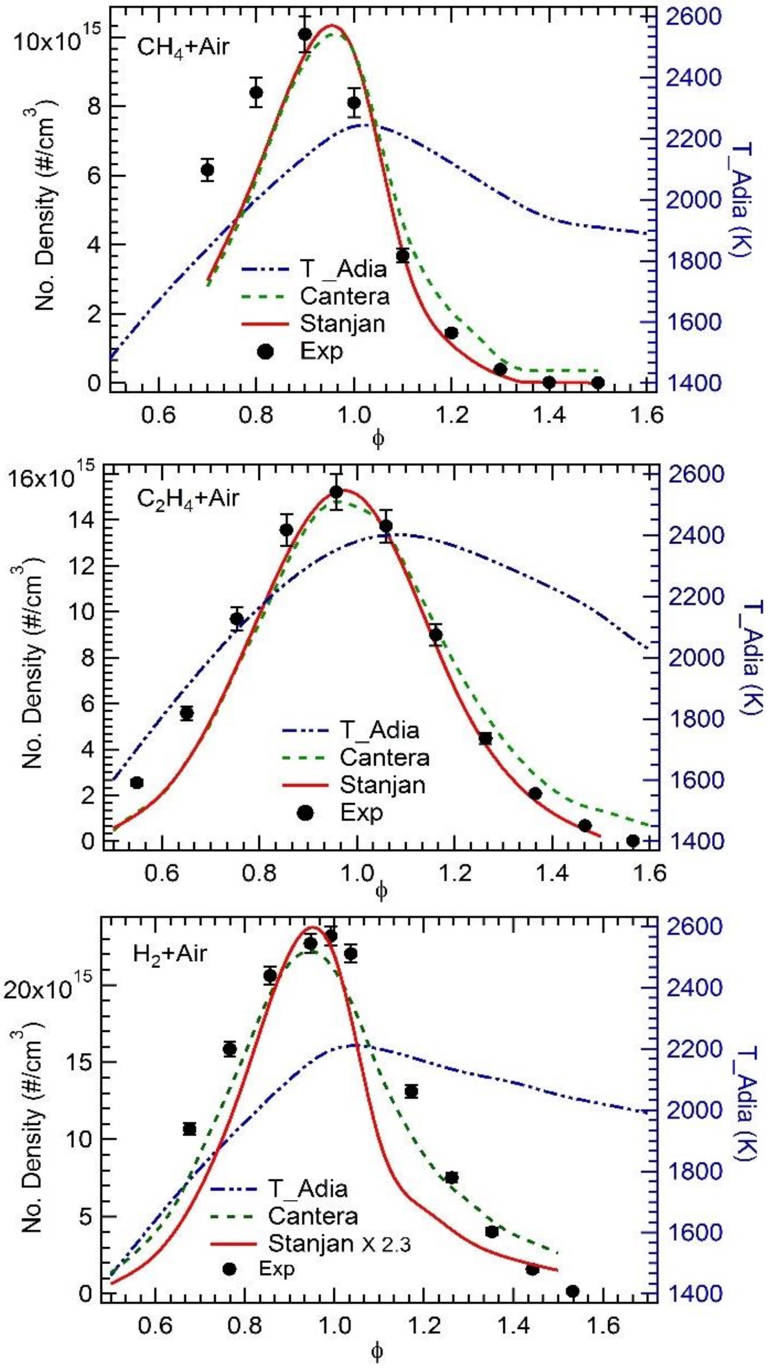

Figure 62. Fs-LIF signal of OH as a function of equivalence ratio in CH_4/air, C_2H_4/air and H_2/air flames stabilized over the Hencken calibration burner.

flames, while it peaks near Φ=1.0 for H_2/air flames. Furthermore, the OH-LIF signals have certain deviations from the equilibrium calculations on the lean sides. The reason for these deviations may be the potential heat loss to the burner surface at slower gas flow rates used to obtain the lean flames.

Then, we compared the fs-LIF experimental OH profiles with previously reported ns-LIF as well as numerically calculated OH profiles at different heights in C_2H_4/air flames [149] stabilized over the Hencken calibration burner. The results are shown in Figure 63, the simulation data had been obtained using a well-validated, time-dependent, axisymmetric CFD code with detailed chemical kinetics known as UNICORN (unsteady ignition and combustion using reactions). As shown in the top panel of Figure 63, near the close proximity to the burner surface at HAB=5 mm height, both ns and fs OH profiles deviate from the calculated values for all equivalence ratios. This observation can be explained by the fact that the fuel and oxidizer rapidly mix just above the surface and could not have reached to an equilibrium state near the surface. Thus, the simulation can underestimate OH concentrations with the assumption of an equilibrium state. However, at 10 and 20 mm HAB, the OH profiles with the fs excitation scheme show a good agreement with the simulation results for all equivalence ratios. The previously reported ns OH profiles show some deviations from the simulation, especially on the rich flames. This observation indicates that the fs-LIF technique is an effective method for OH concentration measurements in a wide range of flame equivalence ratios.

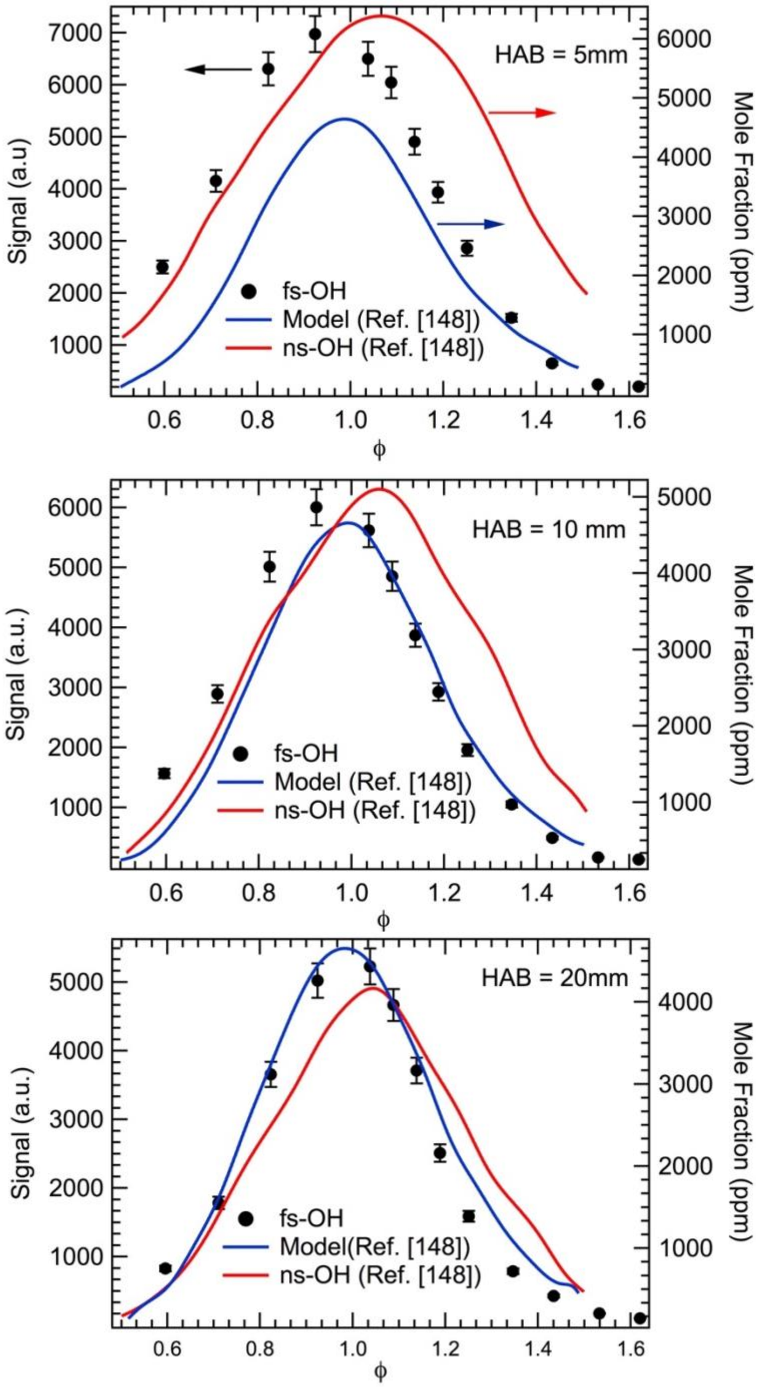

Figure 63. Comparison of fs OH profiles with previously reported ns OH profiles and model predictions at different heights in C_2H_4/air flames.

We then extended the fs transition scheme to 2D OH-PLIF imaging measurements in flames. For PLIF measurements, the f=+200 mm plano-convex lens was replaced by an f=+100 mm plano-convex lens coupled with an f=-25 mm rectangular cylindrical lens, thereby generating a laser sheet with an effective height of approximately 15 mm at the probe region. The Hencken calibration burner was replaced with a Bunsen-type jet burner. The flames used for OH-PLIF studies were premixed C_2H_4/air and diffusion CH_4:H_2 (1:1) jet flames. A high-speed CMOS camera (Photron, Model: SA-Z) coupled with an intensifier (LaVision, Model: HS-IRO) was used to study the turbulent dynamics of the diffusion flames. A 50-mm-focal-length f/1.2 camera lens was used to collect the fluorescence signal and focus it onto the high-speed camera/intensifier system. A 315±10-nm bandpass filter was mounted at the front of the camera lens. The filter transmission efficiency is shown by the dashed-lines in Figure 61. As discussed above, we have found no evidence of spectral interferences with the OH $A^2\Sigma^+ \leftarrow X^2\prod$ transition in the transmission window of this filter. Therefore, the same broadband OH detection filter could be used in this study. A sample single-laser-shot fs-PLIF image of OH in the premixed flame is shown in Figure 64. It can be seen that the cone structure of the steady-state jet flame (shown in the inset) is well demonstrated in the OH PLIF flame. Furthermore, statistics obtained from 2000 consecutive single-laser-shot images recorded at 1-kHz repetition rate shows approximately 10% signal fluctuation with respect to the mean value. These fluctuations could be originated from shot-to-shot laser fluctuations, minor flame instabilities and detection system noise. Moreover, several consecutive single-laser-shot OH-PLIF images recorded at a repetition rate of 1 kHz are shown in Figure 65. These PLIF images were taken at the location indicated by a red rectangular

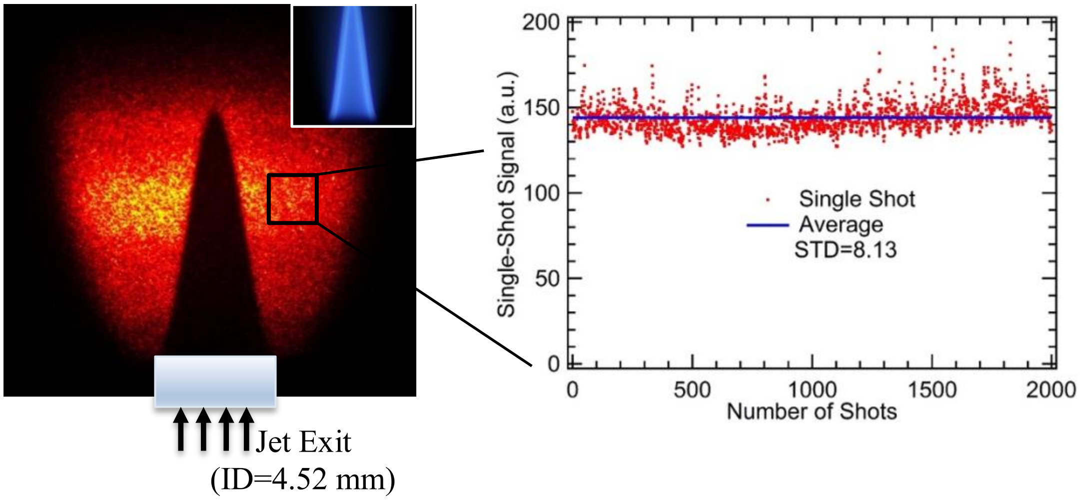

Figure 64. A sample single-laser-shot fs-PLIF image of OH (left) and consecutive single-laser-shot integrated signal distribution (right) recorded in a premixed $C_2H_4/O_2/N_2$ jet flame.

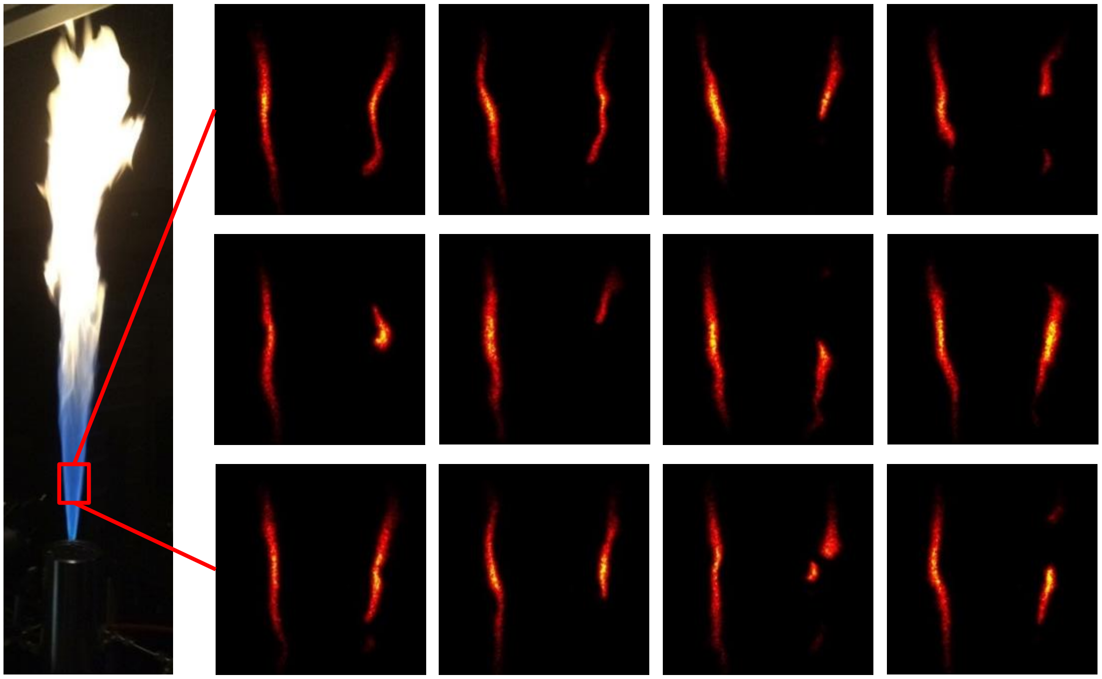

Figure 65. Consecutive single-laser-shot OH-PLIF images recorded at a pulse repetition rate of 1 kHz in a CH_4:H_2 (1:1) diffusion jet flame. Jet exits Reynolds number is approx. 2000. Each frame corresponds to an area of 16 mm×16 mm.

region of the turbulent diffusion flame. As seen from these images, the OH-LIF signal is zero in the central cold reactant zone, then increases at the flame front where the fuels are entrained with the surrounding air, and then decays to zero in the outer radial locations. The variation of the OH-PLIF imaging structure is well captured, along with local flame extinction events from these successive single-laser-shot OH-PLIF images.

6. CONCLUSION & RECOMMENDATIONS FOR FUTURE WORK

6.1 Conclusion

Ultrafast laser pulses have been successfully demonstrated for LIF diagnostics in non-reacting and reacting flow systems. Because of their high peak power but low average power, as well as high pulse-repetition rate, ultrafast laser pulses provide significant advantages over traditionally used ns-duration laser pulses. In experimental studies involving 204.1-nm, fs-TPLIF of Kr for mixing and potential velocimetry applications, the observed Kr line positions agree well with the NIST database. Improved relative intensity values for Kr emission transitions in the 750–840 nm spectral range were obtained. Fluorescence emissions at the 760.15 and 811.29 nm wavelengths are the strongest lines in this spectral range. These results show the potential of the 204.1-nm, fs-TPLIF excitation scheme of Kr for flow mixing and velocimetry studies in practical flow applications.

In the fs-TPLIF measurement studies of CO in gaseous and liquid spray flames, although laser-generated C_2 emissions can be reduced by using low-average-power fs pulses, complete elimination of such interference becomes rather difficult. The second-order scattering interference of the 230-nm excitation laser could also affect the CO fluorescence signal level. The present study suggests a carefully selected spectral filtering scheme coupled with signal time gating in the order of 10 ns, are necessary for reduced interferences on CO detection in gaseous and liquid-fuel flames. As pressure increases, the excitation spectrum broadens towards longer wavelengths. However, that effect has less influence on the excitation quantum efficiency of the LIF process using fs excitation as compared to narrow-band ns excitation scheme. Additionally, the dependence of CO fluorescence signal on the laser energy in the fs-duration excitation scheme indicates the presence of three-photon ionization and stimulated emission processes. These effects are evident from less-than-quadratic laser energy dependence at higher laser energies in the two-photon excitation scheme. A comparison of the measured CO fs-TPLIF signal with the calculated equilibrium CO number densities shows good agreements for both CH_4/air and C_2H_4/air sooting flames in a wide range of flame equivalence ratios. Two-dimensional CO-TPLIF imaging in gaseous and liquid spray flames are also demonstrated. Furthermore, two-line, OH-PLIF thermometry was used to investigate temperature profiles in those liquid spray flames.

Finally, OH-LIF imaging measurements using the broadband, ultrashort-pulse excitation scheme was developed for the first time. A detailed ro-vibrational fluorescence spectroscopy of OH $A^2\Sigma^+ \leftarrow X^2\prod$ (1, 0), (0, 0) and (1, 1) bands can provide details of time-resolved rotational and vibrational energy transfer processes in various reacting flow systems. A reasonable agreement was obtained between the measured OH fluorescence signals and that from equilibrium calculations, in a range of flames. The demonstration of single-laser-shot, 2D OH-PLIF images recorded at 1-kHz repetition rate in a turbulent CH_4/H_2 flame suggests that the OH fs-PLIF is a promising approach for imaging the reaction zone and flame structure in complex reacting flow systems.

6.2 Recommendations for Future Work

One obstacle encountered in quantitative measurements of atoms and molecules of interest in complex combustion environments using the LIF technique is the presence of collisional quenching. Strong temperature-, pressure- and species-dependent collisions result in excited state population decay via non-radiative processes, and thus, reduce the fluorescence quantum yield [150]. Coherent laser technique, four-wave-mixing (FWM) spectroscopy could be a solution for this problem. Previously, FWM has been used successfully for detecting Ammonia, nitric oxide and atomic hydrogen in gas cells or flames [151-153], primarily using ns laser pulses. However, the timescales of collisional quenching are usually sub-nanoseconds, or even in the range of picoseconds for some molecular species in combustion relevant conditions. Therefore, nanosecond laser pulses could not satisfy the temporally-resolved quenching investigation in practical combustion environments. Recently Stauffer et al. [154] combined femtosecond laser pulses and parametric FWM technique to measure NO in the gas phase. They found the time-domain fs-FWM signal associated with the two-photon excitation process exhibit negligible dependence on the concentration of collisional partners. Therefore, in the future work, the single and two-photon LIF schemes investigated during the present study can be extend using fs-FWM to determine quenching-independent species concentration in reacting and non-reacting flow systems.

REFERENCES

1. IEA, "World energy outlook 2016," International Energy Agency, Paris (2016).
2. K. Kohse-Höinghaus, "Laser techniques for the quantitative detection of reactive intermediates in combustion systems," Prog. Energy Combust. Sci. **20**, 203-279 (1994).
3. A. C. Eckbreth, *Laser Diagnostics for Combustion Temperature and Species* (CRC Press, 1996), p. 630.
4. P. Glarborg, "Hidden interactions—Trace species governing combustion and emissions," Proc. Combust. Inst. **31**, 77-98 (2007).
5. R. S. Barlow, G. J. Fiechtner, and J. Y. Chen, "Oxygen atom concentrations and no production rates in a turbulent H_2/N_2 jet flame," Symposium (International) on Combustion **26**, 2199-2205 (1996).
6. S. R. Turns, *An Introduction to Combustion: Concepts and Applications*, 3 ed. (McGraw-Hill Education, 2011), p. 752.
7. M. Jonsson, A. Ehn, M. Christensen, M. Alden, and J. Bood, "Simultaneous one-dimensional fluorescence lifetime measurements of OH and CO in premixed flames," Appl. Phys. B-Lasers Opt. **115**, 35-43 (2014).
8. J. H. Frank, S. A. Kaiser, and M. B. Long, "Reaction-rate, mixture-fraction, and temperature imaging in turbulent methane/air jet flames," Proc. Combust. Inst. **29**, 2687-2694 (2002).

9. J. Haumann, J. M. Seitzman, and R. K. Hanson, "Two-photon digital imaging of CO in combustion flows using planar laser-induced fluorescence," Opt. Lett. **11**, 776-778 (1986).

10. R. P. Lucht, J. T. Salmon, G. B. King, D. W. Sweeney, and N. M. Laurendeau, "Two-photon-excited fluorescence measurement of hydrogen atoms in flames," Opt. Lett. **8**, 365-367 (1983).

11. F. H. Myhr and J. F. Driscoll, "Oxygen-atom concentrations measured in flames: a method to improve the accuracy of laser-induced fluorescence diagnostics," Appl. Opt. **40**, 5388-5394 (2001).

12. W. D. Kulatilaka, J. H. Frank, B. D. Patterson, and T. B. Settersten, "Analysis of 205-nm photolytic production of atomic hydrogen in methane flames," Appl. Phys. B-Lasers Opt. **97**, 227-242 (2009).

13. W. D. Kulatilaka, S. Roy, N. Jiang, and J. R. Gord, "Photolytic-interference-free, femtosecond, two-photon laser-induced fluorescence imaging of atomic oxygen in flames," Appl. Phys. B **122**, 1-7 (2016).

14. F. Di Teodoro, J. E. Rehm, R. L. Farrow, and P. H. Paul, "Collisional quenching of CO $B^1\Sigma^+$ (v'=0) probed by two-photon laser-induced fluorescence using a picosecond laser," J. Chem. Phys. **113**, 3046-3054 (2000).

15. S. S. Dimov and C. R. Vidal, "Cross section for electronic quenching of the CO $B^1\Sigma^+$ state in collisions with hydrogen and helium," Chem. Phys. Lett. **221**, 307-310 (1994).

16. G. W. Loge, J. J. Tiee, and F. B. Wampler, "Multiphoton induced fluorescence and ionization of carbon monoxide (B $^1\Sigma^+$)," J. Chem. Phys. **79**, 196-202 (1983).

17. C. Brackmann, J. Sjoholm, J. Rosell, M. Richter, J. Bood, and M. Alden, "Picosecond excitation for reduction of photolytic effects in two-photon laser-induced fluorescence of CO," Proc. Combust. Inst. **34**, 3541-3548 (2013).

18. D. R. Richardson, S. Roy, and J. R. Gord, "Femtosecond, two-photon, planar laser-induced fluorescence of carbon monoxide in flames," Opt. Lett. **42**, 875-878 (2017).

19. M. Aldén, A. L. Schawlow, S. Svanberg, P. L. Zhang, and W. Wendt, "Three-photon-excited fluorescence detection of atomic hydrogen in an atmospheric-pressure flame," Opt. Lett. **9**, 211-213 (1984).

20. J. H. Frank and T. B. Settersten, "Two-photon LIF imaging of atomic oxygen in flames with picosecond excitation," Proc. Combust. Inst. **30**, 1527-1534 (2005).

21. S. Agrup, U. Westblom, and M. Alden, "Detection of atomic nitrogen using 2-photon laser-induced stimulated emission-application to flames," Chem. Phys. Lett. **170**, 406-410 (1990).

22. P. J. H. Tjossem and K. C. Smyth, "Multiphoton excitation spectroscopy of the $B^1\Sigma^+$ and $C^1\Sigma^+$ Rydberg states of CO," J. Chem. Phys. **91**, 2041-2048 (1989).

23. W. K. Bischel, B. E. Perry, and D. R. Crosley, "Detection of fluorescence from O-atoms and N-atoms induced by 2-photon absorption," Appl. Optics **21**, 1419-1429 (1982).

24. R. S. Barlow and A. N. Karpetis, "Measurements of Scalar Variance, Scalar Dissipation, and Length Scales in Turbulent Piloted Methane/Air Jet Flames," Flow, Turbulence and Combustion **72**, 427-448 (2004).

25. J. A. Sutton and J. F. Driscoll, "A method to simultaneously image two-dimensional mixture fraction, scalar dissipation rate, temperature and fuel consumption rate fields in a turbulent non-premixed jet flame," Exp. Fluids **41**, 603-627 (2006).

26. S. V. Naik, W. D. Kulatilaka, K. K. Venkatesan, and R. P. Lucht, "Pressure, Temperature and Velocity Measurements in Underexpanded Free Jets using Laser-Induced Fluorescence Imaging," Aiaa J. **47**, 839-849 (2009).

27. J. A. Inman, P. M. Danehy, D. W. Alderfer, G. M. Buck, and A. C. McCrea, "Planar Fluorescence Imaging and Three-Dimensional Reconstructions of Capsule Reaction-Control-System Jets," Aiaa J. **47**, 803-812 (2009).

28. N. T. Clemens and M. G. Mungal, "Large-scale structure and entrainment in the supersonic mixing layer," J. Fluid Mech. **284**, 171-216 (2006).

29. M. D. Di Rosa, A. Y. Chang, and R. K. Hanson, "Continuous wave dye-laser technique for simultaneous, spatially resolved measurements of temperature, pressure, and velocity of NO in an underexpanded free jet," Appl. Optics **32**, 4074-4087 (1993).

30. B. Hiller and R. K. Hanson, "Simultaneous planar measurements of velocity and pressure fields in gas flows using laser-induced fluorescence," Appl. Optics **27**, 33-48 (1988).

31. D. G. Fletcher and J. C. McDaniel, "Laser-induced iodinefluorescence technique for quantitative measurement in a nonreacting supersonic combustor," Aiaa J. **27**, 575-580 (1989).

32. S. Cheng, M. Zimmermann, and R. B. Miles, "Supersonic-nitrogen flow-field measurements with the resonant Doppler velocimeter," Appl. Phys. Lett. **43**, 143-145 (1983).

33. J. Yoo, D. Mitchell, D. F. Davidson, and R. K. Hanson, "Planar laser-induced fluorescence imaging in shock tube flows," Exp. Fluids **49**, 751-759 (2010).

34. M. C. Thurber and R. K. Hanson, "Simultaneous imaging of temperature and mole fraction using acetone planar laser-induced fluorescence," Exp. Fluids **30**, 93-101 (2001).

35. V. Narayanaswamy, R. Burns, and N. T. Clemens, "Kr-PLIF for scalar imaging in supersonic flows," Opt. Lett. **36**, 4185-4187 (2011).

36. N. J. Parziale, M. S. Smith, and E. C. Marineau, "Krypton tagging velocimetry of an underexpanded jet," Appl. Opt. **54**, 5094-5101 (2015).

37. R. M. Magee, M. E. Galante, N. Gulbrandsen, D. W. McCarren, and E. E. Scime, "Direct measurements of the ionization profile in krypton helicon plasmas," Phys. Plasmas **19**, 6 (2012).

38. J. Mills, C. Sukenik, and R. Balla, "hypersonic wake diagnostics using laser induced fluorescence techniques," Presented at 42nd AIAA Plasmadynamics and Lasers Conference, Honolulu, Hawaii, June 27-30, 2011 (2011).

39. J. Hargus, William A , G. M. Azarnia, and M. R. Nakles, "Demonstration of Laser-Induced Fluorescence on Krypton Hall Effect Thruster," 32nd International Electric Propulsion Conference, Wiesbaden, Germany, 11-15 Sep 2011 (2011).

40. C. A. Whitehead, B. D. Cannon, and J. F. Wacker, "Trace detection of krypton using laser-induced fluorescence," Appl. Opt. **34**, 3250-3256 (1995).

41. A. G. Hsu, V. Narayanaswamy, N. T. Clemens, and J. H. Frank, "Mixture fraction imaging in turbulent non-premixed flames with two-photon LIF of krypton," Proc. Combust. Inst. **33**, 759-766 (2011).

42. R. S. F. Chang, H. Horiguchi, and D. W. Setser, "Radiative lifetimes and 2-body collisional deactivation rate constants in argon for Kr(4P 55P) and Kr(4P^{5}5P') states," J. Chem. Phys. **73**, 778-790 (1980).

43. J. Jolly and J. P. Booth, "Atomic hydrogen densities in capacitively coupled very high-frequency plasmas in H-2: Effect of excitation frequency," J. Appl. Phys. **97**, 6 (2005).

44. B. N. Ganguly and J. W. Parish, "Absolute H atom density measurement in pure methane pulsed discharge," Appl. Phys. Lett. **84**, 4953-4955 (2004).

45. M. Richter, Z. S. Li, and M. Alden, "Application of two-photon laser-induced fluorescence for single-shot visualization of carbon monoxide in a spark ignited engine," Appl. Spectrosc. **61**, 1-5 (2007).

46. A. V. Mokhov, B. A. V. Bennett, H. B. Levinsky, and M. D. Smooke, "Experimental and computational study of C2H2 and CO in a laminar

axisymmetric methane–air diffusion flame," Proc. Combust. Inst. **31**, 997-1004 (2007).

47. A. V. Mokhov, S. Gersen, and H. B. Levinsky, "Spontaneous Raman measurements of acetylene in atmospheric-pressure methane/air flames," Chem. Phys. Lett. **403**, 233-237 (2005).

48. F. Xu and G. M. Faeth, "Structure of the soot growth region of laminar premixed methane/oxygen flames," Combust. Flame **121**, 640-650 (2000).

49. H. Tsuji and I. Yamaoka, "Structure analysis of counterflow diffusion flames in the forward stagnation region of a porous cylinder," Symposium (International) on Combustion **13**, 723-731 (1971).

50. T. R. Melton, F. Inal, and S. M. Senkan, "The effects of equivalence ratio on the formation of polycyclic aromatic hydrocarbons and soot in premixed ethane flames," Combust. Flame **121**, 671-678 (2000).

51. J. Wang, M. Maiorov, D. S. Baer, D. Z. Garbuzov, J. C. Connolly, and R. K. Hanson, "In situ combustion measurements of CO with diode-laser absorption near 2.3 µm," Appl. Opt. **39**, 5579-5589 (2000).

52. M. E. Webber, J. Wang, S. T. Sanders, D. S. Baer, and R. K. Hanson, "In situ combustion measurements of CO, CO_2, H_2O and temperature using diode laser absorption sensors," Proc. Combust. Inst. **28**, 407-413 (2000).

53. S. Wagner, M. Klein, T. Kathrotia, U. Riedel, T. Kissel, A. Dreizler, and V. Ebert, "Absolute, spatially resolved, in situ CO profiles in atmospheric laminar counter-

flow diffusion flames using 2.3 mu m TDLAS," Appl. Phys. B-Lasers Opt. **109**, 533-540 (2012).

54. R. M. Mihalcea, D. S. Baer, and R. K. Hanson, "Diode laser sensor for measurements of CO, CO_2, and CH_4 in combustion flows," Appl. Opt. **36**, 8745-8752 (1997).

55. M. A. Hines, H. A. Michelsen, and R. N. Zare, "2+1 resonantly enhanced multiphoton ionization of CO via the $E^1\prod$-$X^1\Sigma^+$ transition: From measured ion signals to quantitative population distributions," J. chem. Phys. **93**, 8 (1990).

56. R. W. Jones, N. Sivakumar, B. H. Rockney, P. L. Houston, and E. R. Grant, "A $^1\Pi \leftarrow \chi^1\Sigma^+$ resonance-enhanced multiphoton ionization of jet-cooled CO," Chem. Phys. Lett. **91**, 271-272 (1982).

57. N. Georgiev, K. Nyholm, R. Fritzon, and M. Alden, "Developments of the amplified stimulated stimulated-emission technique for spatially-resolved species detection in flames," Opt. Commun. **108**, 71-76 (1994).

58. A. V. Mokhov, H. B. Levinsky, C. E. Vandermeij, and R. Jacobs, "Analysis of laser-induced-fluorescence carbon-monoxide measurements in turbulent nonpremixed flames," Appl. Opt. **34**, 7074-7082 (1995).

59. J. M. Seitzman, J. Haumann, and R. K. Hanson, "Quantitative 2-photon LIF imaging of carbon-monoxide in combustion gases," Appl. Opt. **26**, 2892-2899 (1987).

60. M. Alden, S. Wallin, and W. Wendt, "Applications of 2-photon absorption for detection of CO in combustion gases," Appl. Phys. B **33**, 205-212 (1984).

61. J. Rosell, J. Sjoholm, M. Richter, and M. Alden, "Comparison of Three Schemes of Two-Photon Laser-Induced Fluorescence for CO Detection in Flames," Appl. Spectrosc. **67**, 314-320 (2013).

62. S. Linow, A. Dreizler, J. Janicka, and E. P. Hassel, "Comparison of two-photon excitation schemes for CO detection in flames," Appl. Phys. B **71**, 689-696 (2000).

63. Y.-C. Chien, D. Escofet-Martin, and D. Dunn-Rankin, "CO emission from an impinging non-premixed flame," Combust. Flame **174**, 16-24 (2016).

64. S. Blomberg, J. Zetterberg, J. Gustafson, J. Zhou, C. Brackmann, and E. Lundgren, "Comparison of AP-XPS and PLIF Measurements During CO Oxidation Over Pd Single Crystals," Topics in Catalysis **59**, 478-486 (2016).

65. A. Singh, M. Mann, T. Kissel, J. Brubach, and A. Dreizler, "Simultaneous Measurements of Temperature and CO Concentration in Stagnation Stabilized Flames," Flow Turbul. Combust. **90**, 723-739 (2013).

66. A. N. Karpetis, T. B. Settersten, R. W. Schefer, and R. S. Barlow, "Laser imaging system for determination of three-dimensional scalar gradients in turbulent flames," Opt. Lett. **29**, 355-357 (2004).

67. N. Georgiev and M. Alden, "Two-dimensional imaging of flame species using two-photon laser-induced fluorescence," Appl. Spectrosc. **51**, 1229-1237 (1997).

68. U. Meier, K. Kohsehoinghaus, and T. Just, "H-atom and O-atom detection for combustion applications-study of quenching and laser photolysis effects," Chem. Phys. Lett. **126**, 567-573 (1986).

69. J. E. M. Goldsmith, "Photochemical effects in 2-photon-excited fluorescence detection of atomic oxygen in flames," Appl. Optics **26**, 3566-3572 (1987).

70. U. Westblom, S. Agrup, M. Alden, and P. Cederbalk, "Detection of nitrogen-atoms in flames using 2-photon laser-induced fluorescence and investigations of photochemical effects," Appl. Opt. **30**, 2990-3002 (1991).

71. A. V. Zobnin, A. P. Nefedov, V. A. Sinel'shchikov, and A. D. Usachev, "Role of photochemical processes in the use of laser-induced fluorescence at 230.1 nm for the diagnostics of hydrocarbon flames," Opt. Spectrosc. **87**, 23-28 (1999).

72. A. P. Nefedov, V. A. Sinel'shchikov, A. D. Usachev, and A. V. Zobnin, "Photochemical effect in two-photon laser-induced fluorescence detection of carbon monoxide in hydrocarbon flames," Appl. Opt. **37**, 7729-7736 (1998).

73. J. S. Bernstein, A. Fein, J. B. Choi, T. A. Cool, R. C. Sausa, S. L. Howard, R. J. Locke, and A. W. Miziolek, "Laser-based flame species profile measurements-a comparison with flame model predictions," Combust. Flame **92**, 85-105 (1993).

74. D. A. Everest, C. R. Shaddix, and K. C. Smyth, "Quantitative two-photon laser-induced fluorescence imaging of CO in flickering CH_4/air diffusion flames," Symposium (International) on Combustion **26**, 1161-1162 (1996).

75. W. D. Kulatilaka, J. H. Frank, and T. B. Settersten, "Interference-free two-photon LIF imaging of atomic hydrogen in flames using picosecond excitation," Proc. Combust. Inst. **32**, 955-962 (2009).

76. S. Agrup and M. Aldén, "Measurements of the Collisionally Quenched Lifetime of CO in Hydrocarbon Flames," Appl. Spectrosc. **48**, 1118-1124 (1994).

77. S. Agrup and M. Alden, "Measurement of the collision-quenched lifetime of CO molecules in a flame at atmospheric-pressure," Chem. Phys. Lett. **189**, 211-216 (1992).

78. T. B. Settersten, A. Dreizler, and R. L. Farrow, "Temperature- and species-dependent quenching of COB probed by two-photon laser-induced fluorescence using a picosecond laser," J. Chem. Phys. **117**, 3173-3179 (2002).

79. M. D. Di Rosa and R. L. Farrow, "Two-photon excitation cross section of the B <-X(0,0) band of CO measured by direct absorption," J. Opt. Soc. Am. B-Opt. Phys. **16**, 1988-1994 (1999).

80. M. D. Di Rosa and R. L. Farrow, "Cross sections of photoionization and ac Stark shift measured from Doppler-free B ← X(0,0) excitation spectra of CO," J. Opt. Soc. Am. B **16**, 861-870 (1999).

81. M. D. D. Rosa and R. L. Farrow, "Temperature-dependent collisional broadening and shift of Q-branch transitions in the B←X(0,0) band of CO perturbed by N_2, CO_2 and CO," J. Quant. Spectrosc. Radiat. Transfer **68**, 363-375 (2001).

82. J. E. M. Goldsmith and D. T. B. Kearsley, "C_2 creation, emission, and laser-induced fluorescence in flames and cold gases," Appl. Phys. B **50**, 371-379 (1990).

83. B. Balko, J. Zhang, and Y.-T. Lee, "193 nm photodissociation of acetylene," J. Chem. Phys. **94**, 7958-7966 (1991).

84. D. L. Osborn and J. H. Frank, "Laser-induced fragmentation fluorescence detection of the vinyl radical and acetylene," Chem. Phys. Lett. **349**, 43-50 (2001).

85. P.-E. Bengtsson and M. Aldén, "Optical investigation of laser-produced C2 in premixed sooty ethylene flames," Combust. Flame **80**, 322-328 (1990).

86. P. Jenny, D. Roekaerts, and N. Beishuizen, "Modeling of turbulent dilute spray combustion," Prog. Energy Combust. Sci. **38**, 846-887 (2012).

87. W. A. Sirignano, "Fuel droplet vaporization and spray combustion theory," Prog. Energy Combust. Sci. **9**, 291-322 (1983).

88. C. K. Law, "Recent advances in droplet vaporization and combustion," Prog. Energy Combust. Sci. **8**, 171-201 (1982).

89. H. H. Chiu, H. Y. Kim, and E. J. Croke, "Internal group combustion of liquid droplets," Symposium (International) on Combustion **19**, 971-980 (1982).

90. A. N. Karpetis and A. Gomez, "An experimental study of well-defined turbulent nonpremixed spray flames," Combust. Flame **121**, 1-23 (2000).

91. R. J. Sornek, R. Dobashi, and T. Hirano, "Effect of turbulence on vaporization, mixing, and combustion of liquid-fuel sprays," Combust. Flame **120**, 479-491 (2000).

92. A. Cessou and D. Stepowski, "Planar Laser Induced Fluorescence Measurement of [OH] in the Stabilization Stage of a Spray Jet Flame," Combust. Sci. Technol. **118**, 361-381 (1996).

93. V. G. McDonell and G. S. Samuelsen, "An Experimental Data Base for the Computational Fluid Dynamics of Reacting and Nonreacting Methanol Sprays," J. Fluids Eng. **117**, 145-153 (1995).

94. R. Lemaire, M. Maugendre, T. Schuller, E. Therssen, and J. Yon, "Original use of a direct injection high efficiency nebulizer for the standardization of liquid fuels spray flames," Rev. Sci. Instrum. **80**, 105105 (2009).

95. M. Mikami, S. Miyamoto, and N. Kojima, "Counterflow diffusion flame with polydisperse sprays," Proc. Combust. Inst. **29**, 593-599 (2002).

96. R. Hadef and B. Lenze, "Measurements of droplets characteristics in a swirl-stabilized spray flame," Exp. Therm Fluid Sci. **30**, 117-130 (2005).

97. G. M. Faeth, "Evaporation and combustion of sprays," Prog. Energy Combust. Sci. **9**, 1-76 (1983).

98. M. Mikami, K. Yamamoto, O. Moriue, and N. Kojima, "Combustion of partially premixed spray jets," Proc. Combust. Inst. **30**, 2021-2028 (2005).

99. H. Correia Rodrigues, M. J. Tummers, E. H. van Veen, and D. J. E. M. Roekaerts, "Spray flame structure in conventional and hot-diluted combustion regime," Combust. Flame **162**, 759-773 (2015).

100. H. W. Ge, I. Düwel, H. Kronemayer, R. W. Dibble, E. Gutheil, C. Schulz, and J. Wolfrum, "Laser-Based Experimental and Monte Carlo PDF Numerical Investigation of an Ethanol/Air Spray Flame," Combust. Sci. Technol. **180**, 1529-1547 (2008).

101. D. Stepowski, A. Cessou, and P. Goix, "Flame stabilization and OH fluorescence mapping of the combustion structures in the near field of a spray jet," Combust. Flame **99**, 516-IN511 (1994).

102. T. R. Meyer, S. Roy, V. M. Belovich, E. Corporan, and J. R. Gord, "Simultaneous planar laser-induced incandescence, OH planar laser-induced fluorescence, and droplet Mie scattering in swirl-stabilized spray flames," Appl. Opt. **44**, 445-454 (2005).

103. R. Lemaire, A. Faccinetto, E. Therssen, M. Ziskind, C. Focsa, and P. Desgroux, "Experimental comparison of soot formation in turbulent flames of Diesel and surrogate Diesel fuels," Proc. Combust. Inst. **32**, 737-744 (2009).

104. I. Boxx, C. Slabaugh, P. Kutne, R. P. Lucht, and W. Meier, "3 kHz PIV/OH-PLIF measurements in a gas turbine combustor at elevated pressure," Proc. Combust. Inst. **35**, 3793-3802 (2015).

105. M. J. Dyer and D. R. Crosley, "Two-dimensional imaging of OH laser-induced fluorescence in a flame," Opt. Lett. **7**, 382-384 (1982).

106. K. L. Steffens, J. Luque, J. B. Jeffries, and D. R. Crosley, "Transition probabilities in OH $A^2\Sigma^+-X\,^2\Pi^i$: Bands with $v'=2$ and 3," J. Chem. Phys. **106**, 6262-6267 (1997).

107. A. Matynia, M. Idir, J. Molet, C. Roche, S. de Persis, and L. Pillier, "Absolute OH concentration profiles measurements in high pressure counterflow flames by coupling LIF, PLIF, and absorption techniques," Appl. Phys. B **108**, 393-405 (2012).

108. J. Kojima and Q.-V. Nguyen, "Entangled biphoton virtual-state spectroscopy of the $A^2R^+–X^2P$ system of OH," Chem. Phys. Lett. **396**, 323-328 (2004).

109. J. E. M. Goldsmith and N. M. Laurendeau, "Two-photon-excited fluorescence measurements of OH concentration in a hydrogen–oxygen flame," Appl. Opt. **25**, 276-283 (1986).

110. D. R. Crosley and G. P. Smith, "Two-photon spectroscopy of the A $^2\Sigma^+$–X $^2\Pi^i$ system of OH," J. Chem. Phys. **79**, 4764-4773 (1983).

111. P. H. Paul and H. N. Najm, "Planar laser-induced fluorescence imaging of flame heat release rate," Symposium (International) on Combustion **27**, 43-50 (1998).

112. R. Giezendanner-Thoben, U. Meier, W. Meier, J. Heinze, and M. Aigner, "Phase-locked two-line OH planar laser-induced fluorescence thermometry in a pulsating gas turbine model combustor at atmospheric pressure," Appl. Opt. **44**, 6565-6577 (2005).

113. S. Roy, T. R. Meyer, R. P. Lucht, V. M. Belovich, E. Corporan, and J. R. Gord, "Temperature and CO_2 concentration measurements in the exhaust stream of a liquid-fueled combustor using dual-pump coherent anti-Stokes Raman scattering (CARS) spectroscopy," Combust. Flame **138**, 273-284 (2004).

114. G. Sutton, A. Levick, G. Edwards, and D. Greenhalgh, "A combustion temperature and species standard for the calibration of laser diagnostic techniques," Combust. Flame **147**, 39-48 (2006).

115. R. Cattolica, "OH rotational temperature from two-line laser-excited fluorescence," Appl. Opt. **20**, 1156-1166 (1981).

116. D. R. Richardson, N. B. Jiang, D. L. Blunck, J. R. Gord, and S. Roy, "Characterization of inverse diffusion flames in vitiated cross flows via two-

photon planar laser-induced fluorescence of CO and 2-D thermometry," Combust. Flame **168**, 270-285 (2016).

117. J. L. Palmer and R. K. Hanson, "Temperature imaging in a supersonic free jet of combustion gases with two-line OH fluorescence," Appl. Opt. **35**, 485-499 (1996).

118. J. M. Seitzman and R. K. Hanson, "Two-line planar fluorescence for temporally resolved temperature imaging in a reacting supersonic flow over a body," Appl. Phys. B **57**, 385-391 (1993).

119. J. M. Seitzman, R. K. Hanson, P. A. DeBarber, and C. F. Hess, "Application of quantitative two-line OH planar laser-induced fluorescence for temporally resolved planar thermometry in reacting flows," Appl. Opt. **33**, 4000-4012 (1994).

120. S. Kostka, S. Roy, P. J. Lakusta, T. R. Meyer, M. W. Renfro, J. R. Gord, and R. Branam, "Comparison of line-peak and line-scanning excitation in two-color laser-induced-fluorescence thermometry of OH," Appl. Opt. **48**, 6332-6343 (2009).

121. R. Devillers, G. Bruneaux, and C. Schulz, "Development of a two-line OH-laser-induced fluorescence thermometry diagnostics strategy for gas-phase temperature measurements in engines," Appl. Opt. **47**, 5871-5885 (2008).

122. G. Laufer, T. M. Quagliaroli, R. H. Krauss, I. R. B. Whitehurst, J. C. McDaniel, and J. H. Grinstead, "Planar OH density and apparent temperature measurements in a supersonic combusting flow," AIAA J. **34**, 463-469 (1996).

123. E. J. Welle, W. Roberts, C. D. Carter, and J. M. Donbar, *The response of a propane-air counter-flow diffusion flame subjected to a transient flow field* (2003), Vol. 135, pp. 285-297.

124. F. C. Bormann, T. Nielsen, M. Burrows, and P. Andresen, "Picosecond planar laser-induced fluorescence measurements of OH $A^2 \Sigma^+$ ($v' = 2$) lifetime and energy transfer in atmospheric pressure flames," Appl. Opt. **36**, 6129-6140 (1997).

125. R. Schwarzwald, P. Monkhouse, and J. Wolfrum, "Picosecond fluorescence lifetime measurement of the OH radical in an atmospheric pressure flame," Chem. Phys. Lett. **142**, 15-18 (1987).

126. W. D. Kulatilaka, S. Roy, and J. R. Gord, "Interference-Free, High-Repetition-Rate Imaging of Atomic-Hydrogen in Flames Using Femtosecond, Femtosecond, Two-Photon-Excited, Laser-Induced Fluorescence (fs-TPLIF)," in *Laser Applications to Chemical, Security and Environmental Analysis*, (Optical Society of America, 2012), LT3B. 1.

127. J. Schmidt, W. Kulatilaka, S. Roy, K. Frederickson, W. Lempert, and J. R. Gord, "Fs-TALIF imaging of atomic species in non-equilibrium plasmas at moderate pressures," in *Laser Applications to Chemical, Security and Environmental Analysis*, (Optical Society of America, 2014), LM3D. 3.

128. W. Kulatilaka, J. Gord, and S. Roy, "Femtosecond two-photon LIF imaging of atomic species using a frequency-quadrupled Ti:sapphire laser," Appl. Phys. B **116**, 7-13 (2014).

129. B. Li, X. Li, D. Zhang, Q. Gao, M. Yao, and Z. Li, "Comprehensive CO detection in flames using femtosecond two-photon laser-induced fluorescence," Opt. Express **25**, 25809-25818 (2017).

130. T. Brian, J. Naibo, and L. Walter, "Review of ultra-high repetition rate laser diagnostics for fluid dynamic measurements," Meas. Sci. Technol. **24**, 012002 (2013).

131. Y. Wang, C. Capps, and W. D. Kulatilaka, "Femtosecond two-photon laser-induced fluorescence of krypton for high-speed flow imaging," Opt. Lett. **42**, 711-714 (2017).

132. K. P. Anil, A. Igor, R. G. James, and R. Sukesh, "Recent advances in ultrafast-laser-based spectroscopy and imaging for reacting plasmas and flames," Plasma Sources Sci. Technol. **26**, 103001 (2017).

133. W. D. Kulatilaka, J. R. Gord, and S. Roy, "Femtosecond two-photon LIF imaging of atomic species using a frequency-quadrupled Ti:sapphire laser," Appl. Phys. B-Lasers Opt. **116**, 7-13 (2014).

134. K. Niemi, V. Schulz-von der Gathen, and H. F. Dobele, "Absolute calibration of atomic density measurements by laser-induced fluorescence spectroscopy with two-photon excitation," J. Phys. D-Appl. Phys. **34**, 2330-2335 (2001).

135. A. Kramida, Y. Ralchenko, J. Reader, and NIST ASD Team, "NIST Atomic Spectra Database (ver. 5.3), [Online]. Available: http://physics.nist.gov/asd," National Institute of Standards and Technology, Gaithersburg, MD. (2015).

136. W. D. Kulatilaka, J. R. Gord, V. R. Katta, and S. Roy, "Photolytic-interference-free, femtosecond two-photon fluorescence imaging of atomic hydrogen," Opt. Lett. **37**, 3051-3053 (2012).

137. Y. Wang and W. D. Kulatilaka, "Detection of carbon monoxide (CO) in sooting hydrocarbon flames using femtosecond two-photon laser-induced fluorescence (fs-TPLIF)," Appl. Phys. B **124**, 8 (2017).

138. T. Ombrello, C. Carter, and V. Katta, "Burner platform for sub-atmospheric pressure flame studies," Combust. Flame **159**, 2363-2373 (2012).

139. R. S. Barlow, R. W. Dibble, J. Y. Chen, and R. P. Lucht, "Effect of Damköhler number on superequilibrium OH concentration in turbulent nonpremixed jet flames," Combust. Flame **82**, 235-251 (1990).

140. Q. N. Chan, P. R. Medwell, B. B. Dally, Z. T. Alwahabi, and G. J. Nathan, "New Seeding Methodology for Gas Concentration Measurements," Appl. Spectrosc. **66**, 803-809 (2012).

141. Meinhard, "Instruction manual for the direct injection high efficiency nebulizer."

142. K. P. Huber and G. Herzberg, "Molecular Spectra And Molecular Structure, IV. Constants Of Diatomic Molecules," New York: Van Nostrand Reinhold (1979).

143. O. Carrivain, M. Orain, N. Dorval, C. Morin, and G. Legros, "Spectroscopic studies of carbon monoxide: application for detection in flames," Proceedings of the European Combustion Meeting (2015).

144. O. Carrivain, M. Orain, N. Dorval, C. Morin, and G. Legros, "Experimental Spectroscopic Studies of Carbon Monoxide (CO) Fluorescence at High Temperatures and Pressures," Appl. Spectrosc. **71**, 2353-2366 (2017).

145. X. Song, Y. Gong, G. Yu, Q. Guo, and Z. Dai, "Chemiluminescence Studies of Coke Oven Gas/O_2 Coflow Normal/Inverse Diffusion Flames," J. Eng. Gas Turb. Power **137**, 1-10 (2015).

146. S. Karnani and D. Dunn-Rankin, "Visualizing CH* chemiluminescence in sooting flames," Combust. Flame **160**, 2275-2278 (2013).

147. B. K. McMillin, J. M. Seitzman, and R. K. Hanson, "Comparison of NO and OH planar fluorescence temperature measurements in scramjet model flowfield," AIAA J. **32**, 1945-1952 (1994).

148. S. Candel, G. Singla, P. Scouflaire, C. Rolon, and L. Vingert, "OH Planar Laser-Induced Fluorescence and Emission Imaging in High Pressure LOx/Methane Flames," J. Propul. Power **23**, 593-602 (2007).

149. T. R. Meyer, S. Roy, T. N. Anderson, J. D. Miller, V. R. Katta, R. P. Lucht, and J. R. Gord, "Measurements of OH mole fraction and temperature up to 20 kHz by using a diode-laser-based UV absorption sensor," Appl. Opt. **44**, 6729-6740 (2005).

150. Z. Yin, C. D. Carter, and W. R. Lempert, "Effects of signal corrections on measurements of temperature and OH concentrations using laser-induced fluorescence," Appl. Phys. B **117**, 707-721 (2014).

151. M. J. Fernée, P. F. Barker, A. E. W. Knight, and H. Rubinsztein-Dunlop, "Sensitive detection of nitric oxide using seeded parametric four-wave mixing," J. Chem. Phys. **108**, 6291-6302 (1998).

152. N. Georgiev and M. Aldén, "Two-photon degenerate four-wave mixing (DFWM) for the detection of ammonia: Applications to flames," Appl. Phys. B **56**, 281-286 (1993).

153. J. A. Gray and R. Trebino, "Two-photon-resonant four-wave-mixing spectroscopy of atomic hydrogen in flames," Chem. Phys. Lett. **216**, 519-524 (1993).

154. H. U. Stauffer, P. J. Wrzesinski, S. Roy, W. D. Kulatilaka, and J. R. Gord, "Collision-independent detection of molecular two-photon excitation by time-resolved parametric four-wave mixing," J. Raman Spectrosc. **47**, 1124-1129 (2016).